NASA TM-81827

NASA Technical Memorandum 81827

NASA-TM-81827 19800017878

ATM-CMG CONTROL SYSTEM STABILITY

W. W. Anderson, L. M. Avis, and K. L. Jacobs

MAY 1980

NATIONAL AERONAUTICS AND SPACE ADMINISTRATION

LANGLEY RESEARCH CENTER

ATM-CMG CONTROL SYSTEM STABILITY

By W. W. Anderson, L. M. Avis,
and K. L. Jacobs

INTRODUCTION

The Apollo Telescope Mount Cluster (ATM, fig. 1) represents the first proposed implementation of a large space station capable of supporting man and experiment packages in a near-earth orbit for extended periods of time (ref. 1). Primary attitude control to 0.1° and 1.0 min/sec will be provided by a control moment gyro (CMG) system with gravity gradient momentum desaturation capability.

This paper presents a discussion of theoretical and experimental research on the stability of this proposed CMG attitude control system. The system experimental data were generated with the Langley Real-Time Digital-Hardware Spacecraft Simulation (ref. 2). The simulation presently uses three prototype 1,000 ft-lb-sec CMG's (fig. 2) and associated control electronics, and a CDC 6600 digital computer programed in real time for vehicle dynamics, required ATM digital control logic, vehicle sensors, filters, and vehicle control logic. The vehicle modal data and design gains used were obtained from reference 3 and will be updated as new data become available.

The theoretical and experimental results of this work are divided into three areas. First, the unit CMG mechanical and electronic characteristics are discussed and CMG gimbal rate or precessional output torque phase and gain data are presented. Second, the momentum feedback or inner loop is discussed theoretically in terms of required CMG bandwidth and experimentally in terms of resulting moment-to-moment output phase and gain and step-function response. Finally, vehicle or outer loop stability data are presented as a function of CMG gimbal orientations and inner and outer loop gains. In all cases, modifications to the flight design are employed only when required to achieve stable low limit cycle response. The fine-pointing mode only has been evaluated at this writing. The effects on experimental data of simulation computer hardware have been minimized but are, of course, present to a certain degree.

SYMBOLS

$[A]$ — square matrix of rank three (3) relating control moment $\bar{G}$ to angular momentum error $\bar{H}_e$

A_{ij} — element of matrix $[A]$ on ith row and jth column

$\lvert A_{ij} \rvert$	absolute value of element A_{ij}
$\overline{G}$	CMG generated control moment
G	control moment component
$G(s)$	CMG gimbal angle rate transfer function
$\overline{H}$	total spin angular momentum of the three CMG's
H	constant spin angular momentum of single CMG
I	spacecraft moment of inertia
$I_m\{s\}$	imaginary part of s
K	inner loop compensation filter gain
K_A	ratio of simulated spacecraft attitude error gains to design attitude error gains
K_g	CMG gear train torsional stiffness
K_{SL}	steering law forward loop gain
$(K_{SL}H)_{max}$	maximum value of $K_{SL} \cdot H$ at which inner loop is stable
K_i	spacecraft attitude error gain for ith axis
K_{Ri}	spacecraft attitude rate error gain for ith axis
M_x, M_y, M_z	disturbance moment components
M_c	commanded control moment
M_F	filtered commanded control moment
n	any integer
$Re\{s\}$	real part of s
s	Laplace transform variable
t	time
W	angular frequency of bending filter
x, y, z	spacecraft reference axes
Z	operator, operates on filtered commanded control moment to yield commanded CMG angular momentum

2

α	outer gimbal angle
β	inner gimbal angle
Δ	CMG gear train deadband
θ_i	spacecraft attitude error angle of rotation about ith spacecraft axis
ρ	bending filter parameter
θ_{CMG}	phase angle of CMG gimbal rate relative to commanded gimbal rate
Ω	spacecraft angular velocity component

Subscripts

c	commanded value
e	error value
F	filtered value
i,j,k	cyclic permutation of 1,2,3; x,y,z
L	limited value
x,y,z	component for the x-, y-, or z-axis
1,2,3	CMG description number; for all gimbal angles zero, CMG No. 1 H-vector points along x-axis, CMG No. 2 H-vector points along y-axis, CMG No. 3 H-vector points along z-axis

Brackets [ ] enclosing a square array of quantities denote a square matrix. Braces { } enclosing a horizontal array of quantities (separated by commas) denote a row vector, and braces enclosing a vertical array denote a column vector. The juxtaposition of a row vector and a column vector, in that order, indicates that the inner product of the two vectors is to be taken. A bar ($^-$) over a symbol denotes a vector. A dot ($\cdot$) over a symbol designates the derivative with respect to time.

MSFC AND LRC COORDINATE SYSTEMS

Figure 3 illustrates the orientation of the CMG's and the definitions of the CMG gimbal angles for the MSFC and the LRC coordinates relative to the vehicle axes; x, the axis of minimum moment of inertia (workshop-CSM axis, fig. 1), z, the telescope viewing axis (LM/ATM axis, fig. 1), and y, the axis normal to x and z forming a right-handed system.

The outer gimbal angles and the inner gimbal angles of the CMG's are labeled "α" and "β," respectively, with a numerical subscript denoting the relevant CMG. The 3-CMG system generates control moments by means of exchange of angular momentum, H_x, H_y, H_z, with the remainder of the spacecraft.

The proposed flight system conforms to the MSFC orientation; however, much of the data presented in this paper pertain to the LRC-CMG orientation because the digital simulation program in LRC coordinates had been thoroughly checked out, while the program in MSFC coordinates had not. The data pertaining to MSFC coordinates presented herein were acquired after the MSFC coordinate digital simulation program was checked out. The control systems employing the MSFC and LRC coordinates are sufficiently similar that most conclusions for one system are valid for the other.

CMG UNIT CHARACTERISTICS

The control moment gyro (CMG) (fig. 2) is a double-gimbaled momentum storage device. A 24-inch-diameter rotor spinning at 11,450 rpm provides 1,000 ft-lb-sec of momentum. The rotor is located within the inner gimbal and is powered by a three-phase induction-type synchronous motor. Excitation for the motor is supplied by either a 400 Hz supply or a variable frequency inverter using 28 V dc.

The CMG unit weighs 209 pounds without the outer frame which serves as a mounting device. The CMG's maximum dimensions are 39.2 inches across the outer frame and 39 inches across the outer gimbal assembly, including its actuator and sensor packages.

Located on each gimbal are an actuator and sensor package. The actuator package contains a 7 ft-lb dc brush torque motor, a dc brush tachometer, and a two-stage planetary gear train with a ratio of 67.6 to 1. The sensor package consists of a second dc brush tachometer, a linear potentiometer, and sine-cosine resolvers. Both gimbals are fully slipringed and have complete rotation capability. The associated electronics provides the CMG with gimbal servo loops, rotor drive power, and system malfunction indicators such as excessive rotor bearing temperatures, rotor speed variations, and electronics failures.

Figure 4 illustrates an operational block diagram of the CMG gimbal rate servo loops. Command gimbal rate signals are sensed at points A_α and A_β, compared with torque motor tachometer signals and the difference or error signal

4

nulled by the torque motor transmission gimbal control loop. This results in a pseudo-control of the actual gimbal rates at points B_α and B_β. The most obvious feature of the servo loop is that the rate of the gimbal is not the controlled element but rather the rate of the torque motor. The contractor's design philosophy consisted of controlling the motor's rate and assuming that the gear train (C_α, C_β) between the motor and gimbal would serve as a rigid link with, of course, the linear reduction in rate due to the gear ratio. Gear train compliance, $1/K_G$, and deadband, Δ, do exist, however, and have a significant effect on performance, as will be illustrated later. Another CMG feature shown in figure 2 illustrates the momentum coupling (D_α, D_β) between the gimbals which causes the gimbal rate loops to interact and is, in fact, the main gyroscopic effect causing the predominant control torques felt by the spacecraft.

Performance of the servo loop in CMG hardware indicated a major difference in frequency response between the torque motor and the gimbal. Although a bandpass of 7 Hz was available at the motor with the contractor's servo loop and later updated at LRC to a bandpass of 15 Hz, figures 5 through 16 indicate gimbal bandwidths of only 3 to 4 Hz. This degradation in performance was found experimentally to result from the large deadband and a low stiffness of the gear train. Output deadbands as large as $0.1°$ and output torsional compliance values on the order of 1/47,000 rad/ft-lb were realized. The gear train deadband affects the CMG gimbal response by determining the actual magnitude of minimum sinusoidal displacement capable of being passed. When the torque motor is commanded to produce a constant magnitude sinusoidal rate with varying frequency, the corresponding magnitude of displacement also varies, proportional to $1/\omega$. Consequently, when the frequency of the commanded rate approaches 3.5 to 4.5 Hz, the output displacement of the torque motor becomes equal to the input deadband of the gear train and no movement is transmitted to the gimbal. The compliance of the gear train also affects the gimbal response by providing a lag between input and output due to a spring windup effect of the transmission. Due to the inability of the gear train to pass higher frequencies, a program is now in progress to improve or replace, with an optimal unit, the gear train and to attempt to compensate for the gear train electronically.

Figures 16 through 19 indicate the gimbal rate responses of the No. 3 CMG after the teeth of the gear trains had been plated, the output bearings preloaded, and with approximately 200 hours of operational time. A comparison of figures 17 through 20 with figures 13 through 16 illustrates the lack of improvement of the gimbal frequency responses. Although an initial improvement was realized with the reworked gear trains, apparently operational time has caused deterioration of the gear train's capability.

MOMENTUM FEEDBACK LOOP

Three 2,000 ft-lb-sec CMG's similar to the Langley prototypes are employed in the ATM design system. Their precessional torque output is controlled by an inner momentum feedback loop and combined vehicle loop integrators. The design goal of this inner loop is to provide a high capability for accurately positioning the three-CMG resultant momentum vector continuously as a function of

5

time. This loop is shown in figure 21 in block diagram form (ref. 4), including the vehicle loop integrators but excluding CMG characteristics. A complete dynamic analysis of this control scheme is virtually impossible because of its nonlinearity and complexity. However, quasi-linear analysis is straightforward where gimbal angle variations are assumed small. A simplified case is presented where all gimbal angles are assumed near zero to allow the generation of required CMG phase and gain for inner loop stability at this particular orientation. The analysis proceeds as follows:

Neglecting higher order small terms, the six command gimbal rates are

$$\dot{\beta}_{1_c} = K_{SL}He_y$$

$$\dot{\beta}_{2_c} = K_{SL}He_z$$

$$\dot{\beta}_{3_c} = K_{SL}He_x$$

$$\dot{\alpha}_{1_c} = -K_{SL}He_z \tag{1}$$

$$\dot{\alpha}_{2_c} = -K_{SL}He_x$$

$$\dot{\alpha}_{3_c} = -K_{SL}He_y$$

where K_{SL} is the steering law forward loop gain.

The three momentum error signals (where command momentum is equal to initial momentum) are

$$He_x = H - (H - H\alpha_2 + H\beta_3)$$

$$He_y = H - (H - H\alpha_3 + H\beta_1) \tag{2}$$

$$He_z = H - (H - H\alpha_1 + H\beta_2)$$

Substitution of equations (2) into equations (1) yields the following, six relations.

$$\dot{\beta}_{1_c} = K_{SL}H(\alpha_3 - \beta_1)$$

$$\dot{\alpha}_{3_c} = K_{SL}H(\beta_1 - \alpha_3)$$

$$\dot{\beta}_{2_c} = K_{SL}H(\alpha_1 - \beta_2)$$

$$\dot{\alpha}_{1_c} = K_{SL}H(\beta_2 - \alpha_1) \tag{3}$$

$$\dot{\beta}_{3_c} = K_{SL}H(\alpha_2 - \beta_3)$$

$$\dot{\alpha}_{2_c} = K_{SL}H(\beta_3 - \alpha_2)$$

These six equations are three sets of two equations with two variables. The first set is shown in block diagram form in figure 22(a), where the CMG is included as an output rate to input command rate transfer function, (G(s)). This diagram can be simplified to that of figure 22(b). The stability of the simplified loop is expressed by the inequality

6

$$-2K_{SL}H \left| \frac{G(s)}{s} \right|_{\phi_{CMG}=-(90°+n360°)} < 1 \qquad (4)$$

For the first crossover (n = 0) this inequality means that

$$(K_{SL}H)_{max} < \frac{\omega_{-90°}}{2\left|G(\omega_{-90°})\right|} \qquad (5)$$

where $\omega_{-90°}$ is the CMG 90° phase lag frequency (rad/sec) and $G(\omega_{-90°})$ is the CMG gain at this frequency. An average value of $(K_{SL}H)_{max}$ using equation (5) for the six initial CMG servo loops was, $K_{SL}H = 2.5$.

Initial simulation runs of the ATM attitude control system with three LRC CMG's have been completed. Typical initial stability data for the proposed flight system are plotted in figure 23 as stable (*) or unstable (▣) points for a set of inner loop (momentum feedback loop) gains, $K_{SL}H$, and outer loop (vehicle loop) attitude gain, K_A, expressed as a fraction of the ATM design gain. Constant vehicle damping was the criteria for selecting vehicle rate gain. Stable inner loop gain, $K_{SL}H$, was consistently an order of magnitude lower than the design value, $K_{SL}H = 10.5$. The effect on stability of increased CMG servo loop gain and increased noise filter bandwidth is also shown in figure 23.

The primary cause of the low inner loop gains is gear train deadband and compliance. Gear plating and gear bearing preloading were accomplished and figure 23, a plot of average CMG gimbal rate limit cycling (fine-pointing mode - no disturbances acting) for increasing inner loop gain, illustrates the improvement in performance.

The resulting simulation was not considered acceptable for further planned maneuver, acquisition, and crew motion investigations, however, since limit cycle magnitudes were still too large for acceptable system life and acceptable vehicle pointing accuracy. A compensation-filtering scheme was incorporated into the simulation where the actual CMG gimbal positions used in calculation of system momentum are altered on a high frequency basis, but where the dc signal of the compensation filter remains the actual gimbal position. This is accomplished by adding the CMG command rate to the gimbal position and filtering the sum. The signal

$$\frac{\alpha_{gimbal} + K\dot{\alpha}_{command}}{1 + KS} \qquad (6)$$

is substituted for α_{gimbal} alone. This eliminates high frequency limit cycling caused by phase lag associated with actual gimbal position, α_{gimbal}, since for high frequency

7

$$\frac{\alpha_{gimbal} + K\dot{\alpha}_{command}}{1 + KS} \sim \alpha_{command} \qquad (7)$$

and also allows for continuous update of gimbal position, since for low frequency

$$\frac{\alpha_{gimbal} + K\dot{\alpha}_{command}}{1 + KS} \sim \alpha_{gimbal} \qquad (8)$$

Figures 25 and 26 show CMG operation with and without the above compensation filter as the CMG's maneuver the ATM 0.05° on all three axes. No noticeable inner loop limit cycles are present after the maneuver is complete. Further data (all analog simulated inner loop) have shown that a compensation gain as low as $K = 2.0$ with $K_{SL}H = 20.0$ is possible with adequate gain margin.

Figures 27(a) through (m) illustrate CMG inner loop response to a step command moment of 100 ft-lb. The figures show the improved inner loop response as the compensation-filter gain, K, is increased. Figures 28(a) and (b) present CMG inner loop response to a sinusoidal command moment of 100 ft-lb at 1.0 cps. The figures illustrate the decreased resonance and increased phase associated with the compensation filter. All data are for the integrated three CMG system hardware with the initial digital inner loop.

The simulation uses CMG gimbal potentiometers rather than gimbal resolvers as in the ATM flight system, however, and is not in itself directly applicable to actual ATM CMG system hardware. The following describes a proposed method for using the same logic as that used in the LRC simulation but specifically adaptable to the ATM hardware.

Proposed Compensation Filter

The above logic for the H-vector system change is based on substitution of the function

$$"\alpha" = \frac{\alpha_{gimbal} + K\dot{\alpha}_{command}}{1 + KS}$$

into the system momentum calculations rather than the gimbal potentiometer reading, α_p, directly. Sin "α" and cos "α" are thus smooth stable variables and inner loop limit cycling is eliminated.

For the ATM hardware, gimbal sine and cosine resolvers are used and thus α_{gimbal} is not available. However, the substitution of the functions

$$"\sin \alpha" = \frac{(\sin \alpha)_r + (\cos \alpha)_r K\dot{\alpha}_{command}}{1 + KS}$$

and

$$\text{"cos }\alpha\text{"} = \frac{(\cos\alpha)_r - (\sin\alpha)_r K\dot{\alpha}_{\text{command}}}{1 + KS}$$

where $(\sin\alpha)_r$ = gimbal sine resolver signal and $(\cos\alpha)_r$ = gimbal cosine resolver signal, is equivalent to the correction used in the LRC simulation, using only signals available in the ATM flight system. The LRC simulation is presently being modified to include gimbal resolver signals rather than gimbal potentiometer signals to validate the above corrections experimentally.

The equivalence of both corrections can be shown by expanding the trigonometric gimbal angle relations as follows:

$$\text{"sin }\alpha\text{"} = \sin\left(\frac{\alpha_{\text{gimbal}} + K\dot{\alpha}_c}{1 + KS}\right)$$

$$= \sin\left(\frac{\alpha_{\text{gimbal}}}{1 + KS}\right)\cos\left(\frac{K\dot{\alpha}_c}{1 + KS}\right)$$

$$+ \cos\left(\frac{\alpha_{\text{gimbal}}}{1 + KS}\right)\sin\left(\frac{K\dot{\alpha}_c}{1 + KS}\right)$$

Assuming that

$$\frac{K\dot{\alpha}_c}{1 + KS} \sim \text{small}$$

then

$$\text{"sin }\alpha\text{"} = \sin\left(\frac{\alpha_{\text{gimbal}}}{1 + KS}\right)(1) + \cos\left(\frac{\alpha_{\text{gimbal}}}{1 + KS}\right)\left(\frac{K\dot{\alpha}_c}{1 + KS}\right)$$

Also assuming that

$$\sin\left(\frac{\alpha_{\text{gimbal}}}{1 + KS}\right) \sim \frac{\sin\alpha_{\text{gimbal}}}{1 + KS}$$

$$\cos\left(\frac{\alpha_{\text{gimbal}}}{1 + KS}\right) \sim \frac{\cos\alpha_{\text{gimbal}}}{1 + KS}$$

then

$$\text{"sin } \alpha \text{"} = \frac{\sin \alpha_{gimbal}}{1 + KS} + \frac{\cos \alpha_{gimbal}}{1 + KS} \frac{K\dot{\alpha}_c}{1 + KS}$$

Finally, the variation between

$$\frac{\cos \alpha_{gimbal}}{1 + KS}$$

and $\cos \alpha_p$ is assumed not to be significant in the second or correction term (a fact to be experimentally verified). Therefore,

$$\text{"sin } \alpha \text{"} = \frac{\sin \alpha_{gimbal} + (\cos \alpha_{gimbal})(K\dot{\alpha}_c)}{1 + KS}$$

$$= \frac{(\sin \alpha)_r + (\cos \alpha)_r K\dot{\alpha}_{command}}{1 + KS}$$

The analysis for "cos α" is similar and will not be included.

CMG SYSTEM OR OUTER LOOP STABILITY

Digital simulations of the ATM-CMG control system have demonstrated space-craft attitude (outer loop) instabilities at certain CMG orientations. A summary of digital simulations of acquisition maneuvers at unfavorable initial CMG (noncollinear) orientations and some typical data traces are presented. By means of a linearized analytical treatment of the control system, minor proposed modifications of the system are developed to stabilize the vehicle. A summary of digital simulations of acquisition maneuvers at unfavorable initial CMG orientations incorporating one proposed modification of the control system are included herein.

The linear analysis of the CMG control system is developed below, incorporating both the MSFC and the LRC CMG coordinate systems (fig. 3).

Linear Analysis of the H-Vector Feedback Control System

Figure 29 schematizes the CMG control system in LRC coordinates, with simplifying approximations made for small vehicle attitude and attitude rate errors. The simplifying approximations and the differences between the MSFC orientation and the LRC orientation control systems are noted in the discussion

10

immediately following. Vehicle flexibility is neglected for the linear analysis but included in all simulation data.

The Euler angles of spacecraft attitude error, θ_x, θ_y, θ_z are transformed into commanded moment components, M_{cx}, M_{cy}, M_{cz}, by means of attitude gains, K_x, K_y, K_z, and attitude rate gains, K_{Rx}, K_{Ry}, K_{Rz}. The commanded moment is filtered by a fourth-order filter designed to isolate the CMG's from frequencies associated with vehicle flexibility. Each component of the filtered command moment is limited to ± 200 ft-lb and the negative time integral of the resulting moment vector is taken, with the constant of negative integration equal to the initial value of the total spin angular momentum vector of the CMG's, yielding the commanded momentum vector, H_{cx}, H_{cy}, H_{cz}. The momentum error vector, formed by subtracting the total spin momentum vector of the CMG's from the commanded vector, generates, via the steering law, the commanded inner and outer gimbal precession rates. The steering law in MSFC coordinates is:

$$\dot{\alpha}_{ic} = K_{SL}(-H_{ei} \sin \alpha_i - H_{ej} \cos \alpha_i)$$

(9)

$$\dot{\beta}_{ic} = K_{SL}(-H_{ei} \cos \alpha_i \sin \beta_i + H_{ej} \sin \alpha_i \sin \beta_i - H_{ek} \cos \beta_i)$$

Before the commanded gimbal rates are fed to the CMG drive system, the gimbal rates are limited to the range $\pm 3.5°$ per sec. The outer and inner gimbal angles are limited to the ranges $\pm 175°$ and $\pm 70°$ or $\pm 80°$, respectively. In the MSFC coordinates, the limits on the outer and inner gimbal angles are $45° \pm 175°$, and $\pm 80°$, respectively. The computer simulations in MSFC or LRC coordinates have the appropriate limits on the gimbal angles and rates and have the gyro transfer functions, $G_{i\alpha}(s)$ and $G_{i\beta}(s)$ equal to unity. The control moments resulting from CMG precession are given by:

$$G_i = H\Big[(\Omega_k + \dot{\alpha}_j)\cos \beta_j \cos \alpha_j + (\Omega_j + \dot{\alpha}_i)\sin \alpha_i \cos \beta_i$$

$$- (\Omega_j + \dot{\beta}_j \sin \alpha_j)\sin \beta_j + (\Omega_k + \dot{\beta}_i \cos \alpha_i)\sin \beta_i$$

$$- (\Omega_k \sin \alpha_k + \Omega_j \cos \alpha_k + \dot{\beta}_k)\cos \beta_k\Big]$$

(10)

in LRC coordinates, and

$$G_i = H\Big[- (\Omega_k - \dot{\alpha}_i)\cos\beta_i \sin\alpha_i - (\Omega_j - \dot{\alpha}_k)\cos\alpha_k \cos\beta_k$$
$$+ (\Omega_j + \dot{\beta}_i \cos\alpha_i)\sin\beta_i - (\Omega_k + \dot{\beta}_k \sin\alpha_k)\sin\beta_k$$
$$+ (\Omega_k \cos\alpha_j + \Omega_j \sin\alpha_j + \dot{\beta}_j)\cos\beta_j\Big] \tag{11}$$

in MSFC coordinates. These result from

$$\overline{g} = -\overline{\omega} \times \overline{H}$$

where $\overline{g}$ is the moment produced by one CMG, $\overline{\omega}$ is the precessional angular velocity of the CMG in inertial space, and $\overline{H}$ is the angular momentum associated with CMG spin.

To simplify the analysis, the vehicle attitude rates, Ω_x, Ω_y, Ω_z are ignored in equations (10) and (11) with little error, as is shown by the following order-of-magnitude calculation. It is assumed that all vehicle attitude rates are initially zero.

$$G \sim H(\Omega + \dot{\alpha})$$

where G is the order of magnitude of the control moment, H = scalar angular momentum of a CMG, $\Omega \sim$ vehicle attitude rate, $\dot{\alpha} \sim$ gimbal precession rate. Note that

$$\dot{\Omega} \sim \frac{G}{I}$$

where $I \sim$ vehicle moment of inertia $\sim 10^6$ slug-ft^2. Hence

$$\Omega \sim \frac{G}{IS}$$

where $s \sim$ characteristic frequency of control system $\gtrsim 0.3$ sec^{-1}. It follows that

$$G \sim H\Big(\frac{G}{IS} + \dot{\alpha}\Big) \sim H\Big(\frac{G}{10^6 s} + \dot{\alpha}\Big)$$

or

12

$$G \sim \frac{HG}{10^6 s} + H\dot{\alpha} = \frac{2 \times 10^{-3}}{s} G + 2000\dot{\alpha}$$

where 2000 ft-lb-sec is substituted for H.

The contribution to the control moment, G, from the vehicle rate, Ω, is of the order or less than $\frac{2 \times 10^{-3}}{0.3} G$, which is much less than the total control moment, and thus much less than the contribution from the gimbal rates.

In the proposed flight system, the values of the sine and cosine of the gimbal angles, as measured by resolvers in the CMG gimbal assemblies, are used in the steering law and in determining the total CMG spin angular momentum components, H_x, H_y, H_z. In the idealized computer simulations for this work, the gimbal angles are obtained by integration of the simulated gimbal precessional rates (relative to vehicle coordinate axes) and the sines and cosines are then calculated by the computer. Neglecting vehicle attitude rates in equations (10) or (11) is equivalent to considering the vehicle coordinate system to be an inertial frame, in which case the total spin angular momentum of the CMG's is the negative integral of the control moment, a fact which is useful in analysis.

The computer simulations utilize the Euler equation,

$$G_i + M_i = I_i \dot{\Omega}_i + (I_k - I_j)\Omega_k \Omega_j \tag{12}$$

(where M_i is the ith component of the disturbance torque) to obtain the vehicle angular acceleration. For analysis of acquisition maneuvers from initial attitude errors much less than $1°$ and with no disturbance torques and no initial vehicle attitude rates, equation (12) can be simplified to:

$$G_i = I_i \ddot{\theta}_i \tag{13}$$

The fractional error introduced by simplifying equation (12) is small and $\sim \frac{\Omega^2}{\dot{\Omega}} \sim \frac{s^2 \theta^2}{s^2 \theta} = \theta$, where coupling of vehicle attitude rates into off-axis Euler angle rates is neglected (a first order in θ effect), Ω is the order of magnitude ($\sim$) of the vehicle attitude rates, $s \sim$ characteristic frequency of system, and $\theta \sim$ vehicle attitude errors. Then,

$$\theta_i = \theta_i(0) - \frac{1}{I_i} \cdot \int_0^t H_i \, dt$$

$$(14)$$

$$= \theta_i(0) + \frac{1}{I_i} \int_0^t \int_0^t G_i \, dt \, dt$$

To linearize the control system, the vehicle attitude errors are restricted to a small fraction of a degree, initial vehicle angular rates are assumed to be zero, and the gimbal angles, gimbal rates, and commanded moments are assumed to be less than their respective limits.

The steering law in LRC coordinates is:

$$\dot{\alpha}_{ic} = K_{SL}(-H_{ei} \sin \alpha_i - H_{ek} \cos \alpha_i)$$

$$(15)$$

$$\dot{\beta}_{ic} = K_{SL}(-H_{ei} \cos \alpha_i \sin \beta_i + H_{ej} \cos \beta_i + H_{ek} \sin \alpha_i \sin \beta_i)$$

The CMG control moment components are approximately:

$$G_i = H(\dot{\alpha}_j \cos \beta_j \cos \alpha_j + \dot{\alpha}_i \sin \alpha_i \cos \beta_i - \dot{\beta}_j \sin \alpha_j \sin \beta_j$$

$$+ \dot{\beta}_i \cos \alpha_i \sin \beta_i - \dot{\beta}_k \cos \beta_k)$$

in LRC coordinates. The vehicle behavior as simulated by computer has been observed to be insensitive to substitution of ideal CMG's (for which $G_\alpha(s) = G_\beta(s) = 1$) for actual CMG hardware when the inner loop (with hardware) is stable (see earlier section). The assumption follows that

$$\dot{\alpha}_i = \dot{\alpha}_{ic}$$

$$\dot{\beta}_i = \dot{\beta}_{ic}$$

The CMG control moment components become, in LRC coordinates:

$$G_i = -K_{SL} H \left\{ H_{ei}, \ H_{ej}, \ H_{ek} \right\} \begin{cases} \cos^2\alpha_j \cos \beta_j + \sin^2\alpha_i \cos \beta_i + \sin^2\beta_j \sin^2\alpha_j \\ \sin \alpha_j \cos \alpha_j \cos \beta_j \\ \sin \beta_j \cos \beta_j \sin \alpha_j - \sin^2\beta_i \sin \alpha_i \cos \alpha_i \end{cases}$$

$$+ \cos^2\alpha_i \sin^2\beta_i + \cos^2\beta_k$$

$$- \sin \alpha_j \cos \alpha_j \sin^2\beta_j - \sin \beta_i \cos \beta_i \cos \alpha_i + \sin \beta_k \cos \beta_k \sin \alpha_k$$

$$- \sin \beta_k \cos \beta_k \cos \alpha_k + \sin \alpha_i \cos \alpha_i \cos \beta_i \Bigg\}$$

$$(16)$$

14

Similarly, in MSFC coordinates,

$$G_i = -K_{SL}H \left\{ H_{ei}, H_{ej}, H_{ek} \right\} \begin{cases} \sin^2\alpha_i \cos\beta_i + \cos^2\alpha_k \cos\beta_k \\ \sin\alpha_i \cos\alpha_i \cos\beta_i - \sin\alpha_i \cos\alpha_i \sin^2\beta_i \\ \sin\alpha_k \cos\alpha_k \cos\beta_k + \sin\beta_i \cos\beta_i \cos\alpha_i \end{cases}$$

$$\left. \begin{aligned} &+ \cos^2\alpha_i \sin^2\beta_i + \sin^2\alpha_k \sin^2\beta_k + \cos^2\beta_j \\ &- \sin\beta_k \cos\beta_k \sin\alpha_k + \cos\alpha_j \sin\beta_j \cos\beta_j \\ &- \sin\alpha_k \cos\alpha_k \sin\beta_k - \sin\alpha_j \sin\beta_j \cos\beta_j \end{aligned} \right\} \tag{17}$$

Expanding equations (16) and (17), define the matrix $[A]$ by:

$$\left\{ G_x, G_y, G_z \right\} = \left\{ H_{ex}, H_{ey}, H_{ez} \right\} \begin{bmatrix} A_{11} & A_{12} & A_{13} \\ A_{21} & A_{22} & A_{23} \\ A_{31} & A_{32} & A_{33} \end{bmatrix} \tag{18}$$

$$= \left\{ H_{ex}, H_{ey}, H_{ez} \right\} [A]$$

for both MSFC and LRC coordinates. A 21st order characteristic equation of the control system can be derived with no additional simplifying assumptions. Neglect of the components of the matrix $[A]$ off the principal diagonal results in the seventh order characteristic equation derived in the following, using figure 29. The predictions of vehicle behavior based on this simplified theory are then verified by observed computer simulated vehicle behavior. Here,

$$G_i = H_{ei}A_{ii} \tag{19}$$

and

$$H_{ei} = H_{ci} - H_i \tag{20}$$

by definition. Note that

$$H_{ci} = -\frac{M_{Fi}}{s} \tag{21}$$

15

and

$$-H_1 = \frac{G_1}{s} \tag{22}$$

hence

$$G_1 = A_{11}\left(\frac{G_1}{s} - \frac{M_{F1}}{s}\right)$$

or

$$G_1 = \frac{A_{11}M_{F1}}{s - A_{11}} \tag{23}$$

For $K_{SL}H > 0$ and $|\beta_i|$, $|\beta_j|$, $|\beta_k| < \frac{\pi}{2}$,

$$A_{11} < 0$$

and

$$G_1 = \frac{|A_{11}|}{s + |A_{11}|} M_{F1} \tag{24}$$

The output of the bending filter is

$$M_{F1} = M_{c1}\left\{\frac{1}{\left[\dfrac{s^4}{W_1^4} + \dfrac{4\rho_1}{W_1^3}s^3 + \dfrac{(4\rho_1^2 + 2)}{W_1^2}s^2 + \dfrac{4\rho_1}{W_1}s + 1\right]}\right\} \tag{25}$$

where

$$M_{c1} = -K_1\theta_1 - K_{R1}s\theta_1 \tag{26}$$

Therefore

$$G_1 = \frac{|A_{11}|}{s + |A_{11}|}\left\{-K_1\theta_1 - K_{R1}s\theta_1\right\}\frac{1}{\left[\dfrac{s^4}{W_1^4} + \dfrac{4\rho_1}{W_1^3}s + \dfrac{(4\rho_1^2 + 2)}{W_1^2}s + \dfrac{4\rho_1}{W_1}s + 1\right]}$$

$$\tag{27}$$

16

Substituting the expression

$$G_i = I_1\theta_1 s^2 \tag{28}$$

into (27) and arranging in standard form yields

$$\frac{I_1}{W_1^4}s^7 + \left[\frac{|A_{11}|I_1}{W_1^4} + \frac{4\rho_1 I_1}{W_1^3}\right]s^6 + \left[\frac{(4\rho_1^2 + 2)I_1}{W_1^2} + \frac{4\rho_1 I_1}{W_1^3}\right]s^5$$

$$+ \left[\frac{4\rho_1 I_1}{W_1} + \frac{|A_{11}|(4\rho_1^2 + 2)I_1}{W_1^2}\right]s^4 + (I_1)s^3 + (|A_{11}|I_1)s^2$$

$$+ (K_{R1}|A_{11}|)s + K_1|A_{11}| = 0 \tag{29}$$

The above is valid for either MSFC or LRC coordinates.

Equation (29) was solved numerically, varying the parameter $|A_{11}|$, for present design values of the functions I_1, W_1, ρ_1, K_1, and K_{R1}, which are:

$$I_x = 0.4555 \times 10^6 \text{ slug-ft}^2$$

$$I_y = 3.475 \times 10^6 \text{ slug-ft}^2$$

$$I_z = 3.235 \times 10^6 \text{ slug-ft}^2$$

$$W_1 = 4.26 \text{ rad/sec}$$

$$W_2 = 1.5 \text{ rad/sec}$$

$$W_3 = 2.6 \text{ rad/sec}$$

$$\rho_1 = 0.5$$

$$\rho_2 = 0.5$$

$$\rho_3 = 0.5$$

$$K_x = 1.475 \times 10^5 \text{ ft-lb}$$

$$K_y = 2.95 \times 10^5 \text{ ft-lb}$$

$$K_z = 7.375 \times 10^5 \text{ ft-lb}$$

$$K_{Rx} = 2.95 \times 10^5 \text{ ft-lb-sec}$$

$$K_{Ry} = 1.1 \times 10^6 \text{ ft-lb-sec}$$

$$K_{Rz} = 2.46 \times 10^6 \text{ ft-lb-sec}$$

The parameter $|A_{11}|$ was varied from the maximum possible value when the steering law constant K_{SL} is the design value, 0.00525 $\text{slug}^{-1}\text{-ft}^{-2}$, to values which resulted in vehicle instabilities (positive real parts of any solution for s). In LRC coordinates, the element A_{11} is, from equation (16),

$$A_{11} = -K_{SL}H(\cos^2\alpha_j \cos\beta_j + \sin^2\alpha_i \cos\beta_i + \sin^2\beta_j \sin^2\alpha_j$$
$$+ \cos^2\alpha_i \sin^2\beta_i + \cos^2\beta_k) \tag{30}$$

The limits on the inner gimbal angles, β_L, are plus and minus an acute angle, and so, $\cos\beta_i > 0$, $\cos\beta_j > 0$, and $\cos\beta_k > 0$. Thus all the terms in parentheses in equation (30) are positive, and the minimum value of $|A_{11}|$ results when $\alpha_i = 0$ or π, $\alpha_j = \pm\frac{\pi}{2}$, $\beta_i = 0$, $\beta_j = 0$, $\pm\beta_k = \beta_L$, yielding $|A_{11}|$ equal to $K_{SL}H \cos^2\beta_L \text{ sec}^{-1}$. In MSFC coordinates, the element A_{11} is, from equation (17)

$$A_{11} = -K_{SL}H(\sin^2\alpha_i \cos\beta_i + \cos^2\alpha_k \cos\beta_k + \cos^2\alpha_i \sin^2\beta_i$$
$$+ \sin^2\alpha_k \sin^2\beta_k + \cos^2\beta_j) \tag{31}$$

The minimum value of $|A_{11}|$ results when $\alpha_k = \pm\frac{\pi}{2}$, $\alpha_i = 0$ or π, $\beta_i = 0$, $\beta_k = 0$, $\beta_j = \pm\beta_L$, yielding $|A_{11}|$ equal to $K_{SL}H \cos^2\beta_L \text{ sec}^{-1}$. For $\beta_L = \pm 80$, $|A_{11}|$ has a minimum value of 0.317 sec in either MSFC or LRC coordinates. For $\beta_L = \pm 70^\circ$, $|A_{11}|$ has a minimum value of 1.23 sec^{-1}.

Figures 30, 31, and 32 display the real parts of the solutions of equation (29) for s for θ_x, θ_y, and θ_z, respectively. The least damped root, for all axes, rapidly approaches zero damping as $|A_{11}|$ drops from about 5 sec^{-1}, indicating deteriorating vehicle control capability. Figure 33 is a plot of the least damped root for all axes in the neighborhood of neutral stability (zero damping). The linear model predicts neutral stability at $|A_{11}| = 0.963 \text{ sec}^{-1}$ or $|A_{22}| = 0.825 \text{ sec}^{-1}$ or $|A_{33}| = 1.10 \text{ sec}^{-1}$. Digital simulations of acquisition maneuvers from initial spacecraft attitude errors

18

of 10^{-4} rad ($\sim 0.006°$) on all axes (which is in the linear range) with ideal gyros ($g_\alpha(s) = g_\beta(s) = 1$) demonstrated neutral stability at the following initial gimbal angles, in LRC coordinates:

θ_x neutral stability; $\alpha_2 = 90°$, $\beta_3 = 68.8°$, other gimbal angles zero

θ_y neutral stability; $\alpha_3 = 90°$, $\beta_1 = 71.0°$, other gimbal angles zero

θ_z neutral stability; $\alpha_1 = 90°$, $\beta_2 = 60.2°$, other gimbal angles zero

where $\beta_L = \pm 80°$. The linear model predicts neutral stability at the following gimbal angles:

θ_x neutral stability; $\alpha_2 = 90°$, $\beta_3 = 72.4°$, other gimbal angles zero

θ_y neutral stability; $\alpha_3 = 90°$, $\beta_1 = 73.7°$, other gimbal angles zero

θ_z neutral stability; $\alpha_1 = 90°$, $\beta_2 = 71.2°$, other gimbal angles zero

by virtue of the fact that $|A_{11}| = K_{SL}H \cos^2(72.4°) = 0.963$ sec^{-1}, $|A_{22}| = K_{SL}H \cos^2(73.7°) = 0.825$ sec^{-1}, $|A_{33}| = K_{SL}H \cos^2(71.2°) = 1.10$ sec^{-1}, respectively, where $K_{SL}H$ is $0.00525 \times 2000 = 10.5$ sec^{-1}, the design value. Figures 34(a), 34(b), and 34(c) show computer simulated vehicle attitude for three acquisition maneuvers in the neighborhood of neutral stability for θ_x.

There are CMG gimbal orientations in which the off-diagonal components of the matrix $[A]$ vanish. Some examples are, in both LRC and MSFC coordinates:

(a) all gimbal angles = 0

(b) $\alpha_1 = \pm 90°$, other gimbal angles zero

(c) $\alpha_2 = \pm 90°$, other gimbal angles zero

(d) $\alpha_3 = \pm 90°$, other gimbal angles zero

as can be seen from equations (16) and (17). As a check of the linear model of the control system under conditions where the complicating effects of the off-diagonal elements of the matrix $[A]$ are not present, computer simulations of acquisition maneuvers were run at gimbal orientations that diagonalize $[A]$. The value of $K_{SL}H$ was varied in order to induce neutral stability and instability. The following summarizes the results.

NEUTRAL STABILITY, (LRC COORDINATES)

Initial gimbal angles	Initial nonzero attitude angles	$K_{SL}H$ simulated	$K_{SL}H$ predicted by linear model
$\alpha_2 = 90°$, others zero	$\theta_x = 10^{-4}$ rad	0.9625	0.9625
$\alpha_2 = 90°$, others zero	$\theta_x = \theta_y = \theta_z = 10^{-4}$ rad	0.8	0.825
$\alpha_1 = 90°$, others zero	$\theta_z = 10^{-4}$ rad	1.1	1.1

Figures 35(a), 35(b), and 35(c) are recordings of the simulated vehicle attitude for these acquisition maneuvers. The predicted value of $K_{SL}H$ for neutral stability is found by means of equation (30) and figure 33 as follows:

For $\alpha_i = 90°$ and others zero, $A_{ii} = -3K_{SL}H$

For $\alpha_j = 90°$ and others zero, $A_{ii} = -K_{SL}H$

For $\alpha_k = 90°$ and others zero, $A_{ii} = -2K_{SL}H$

For neutral stability in θ_x, $A_{11} = -0.9625$

For neutral stability in θ_y, $A_{22} = -0.825$

For neutral stability in θ_z, $A_{33} = -1.1$

Therefore, predicted neutral stability occurs for

θ_x at $\alpha_2 = 90°$ and others zero when $K_{SL}H = 0.9625$

θ_y at $\alpha_3 = 90°$ and others zero when $K_{SL}H = 0.825$

θ_z at $\alpha_1 = 90°$ and others zero when $K_{SL}H = 1.1$

Figures 36, 37, and 38 display the imaginary parts (frequencies) of the complex solutions of equation (29). The negative imaginaries of the complex conjugates to the roots with positive imaginaries are not plotted. The frequencies of the least damped solutions are observable in computer simulations of the CMG control system near the condition of neutral stability with respect to the axis to which the solution pertains; the wave forms of the spacecraft attitude then persist long enough for the wavelengths on the recording chart to be measured. Figure 39 is a plot of the solution frequencies in the neighborhood of neutral stability and of frequencies observed in computer simulations of the control system in LRC coordinates with ideal CMG's. The "coupled x" data points correspond to the condition $\alpha_2 = 90^\circ$, $\beta_3 = 70^\circ$, other gimbal angles zero, and $K_{SL}H$ has the value required to make $|A_{11}|$ equal to the value on the abscissa. Similarly, "coupled y" means $\alpha_3 = 90^\circ$, $\beta_1 = 70^\circ$, and "coupled z" means $\alpha_2 = 90^\circ$, $\beta_3 = 70^\circ$. "Uncoupled x, y, z" correspond to the condition $\alpha_2 = 90^\circ$, $\alpha_3 = 90^\circ$, and $\alpha_1 = 90^\circ$, respectively, with $K_{SL}H$ variable. The initial vehicle attitude errors are $\theta_x = \theta_y = \theta_z = 10^{-4}$ rad except for the "uncoupled x" and "uncoupled z" cases, where the nonzero initial attitude errors are $\theta_x = 10^{-4}$ rad and $\theta_z = 10^{-4}$ rad, respectively. The term, "coupled," indicates that the off-diagonal elements of the matrix $[A]$ are not all zero.

Table II is a summary of simulated acquisition maneuvers in MSFC coordinates, incorporating the isogonal correction logic. The isogonal scheme tends to minimize the inner gimbal angles and to space the individual CMG spin angular momentum vectors symmetrically with respect to the total CMG spin angular momentum vector. The simulations of table II are outside of the linear range of the control system; the filtered commanded moment limit and the gimbal rate limit are both invoked.

Equation (24) and the linear model indicate increasing lag of the control moment, G_1, with respect to the filtered commanded moment, M_{F1}, as the magnitude of the matrix element A_{11} decreases. One way to try to avoid the instability associated with low $|A_{11}|$ is to raise the lower limit on $|A_{11}|$ by increasing $K_{SL}H$ and/or narrowing the limits on the inner gimbal angles. The upper limit on $K_{SL}H$ is set by the requirement of inner loop stability. The inner loop is sketched in figure 29 and discussed in the previous section. The penalty paid for narrowing the inner gimbal travel is that the inner gimbals will hit their stops more often than before, thus reducing CMG redundancy and torque linearity and/or more power will be consumed in moving the inner gimbal away from the stops. These possible remedies will be investigated in the future. Another stabilizing modification of the control system is to replace the negative integration of the limited commanded moment, $\bar{M}_F$, by an operator Z, such that $H_{e1} = \dfrac{M_{F1}}{A_{11}}$. The following is a derivation of the operator, Z, utilizing figure 29, for both MSFC and LRC coordinates. With

$$H_{e1} = \frac{M_{F1}}{A_{11}}. \qquad (32)$$

21.

and replacing the relation, $H_{ei} = \dfrac{M_{Fi}}{s}$, by $H_{ei} = ZM_{Fi}$ in figure 29,

$$H_{ei} = H_{ci} - H_i = M_{Fi} \cdot Z - H_i$$

$$= M_{Fi} \cdot Z + \frac{G_i}{s}$$

By equations (32) and (18),

$$\frac{M_{Fi}}{A_{ii}} = M_{Fi} \cdot Z + \frac{1}{s}(A_{ii}H_{ei} + A_{ij}H_{ej} + A_{ik}H_{ek})$$

so that

$$Z = \frac{1}{A_{ii}} - \frac{1}{s}\left(1 + \frac{A_{ij}}{A_{jj}}\frac{M_{Fj}}{M_{Fi}} + \frac{A_{ik}}{A_{kk}}\frac{M_{Fk}}{M_{Fi}}\right) \qquad (33)$$

the constant of integration being the initial value of H_i. The control moment becomes equal to the control moment of the unmodified control system at infinite $|A_{ii}|$, that is, there is no lag from M_{Fi} to G_i. Note that division by the A_{ii}'s is allowed because they are never zero. The control moment G_i is, by equations (18) and (32):

$$G_i = A_{ii}H_{ei} + A_{ij}H_{ej} + A_{ik}H_{ek}$$

$$= M_{Fi} + \frac{A_{ij}}{A_{jj}}M_{Fj} + \frac{A_{ik}}{A_{kk}}M_{Fk} \qquad (34)$$

Figure 40 schematizes the assumed linear circuit equivalent to the circuit of the control system employing the operator Z. The equivalent circuit has no inner loop, however, the idealized computer simulation represented by figure 40 and used to test the utility of the Z operator is equivalent to the idealized computer simulation of the CMG control system incorporating the inner loop and the operator Z, when all simulated CMG's are fully functional.

The real parts of the least damped roots of the sixth order characteristic equation for the linearized control system represented by figure 40, neglecting the nondiagonal elements of the matrix A, are:

For θ_x, -0.352 sec^{-1}, independent of A_{11}

For θ_y, -0.167 sec^{-1}, independent of A_{22}

For θ_z, -0.390 sec^{-1}, independent of A_{33}

Comparison of these root parts with the real parts of the roots of the characteristic equation for the linearized control system of figure 29 indicates that the Z operator increases vehicle stability at low values of $|A_{11}|$. Idealized computer simulations demonstrate that the Z operator improves the CMG system control capability overall. Table III is a summary and comparison of idealized digital simulations of vehicle acquisition maneuvers performed by the CMG control system with and without the Z operator. The simulations, in LRC coordinates, are outside of the linear range of the control system because gimbal rates and filtered commanded moments are confined by the limiters.

CONCLUSIONS AND RECOMMENDATIONS

The conclusions and recommendations for this paper are divided into the three ATM-CMG system areas: (1) the CMG servo loops, (2) the ATM H-vector inner loops, and (3) the controlled ATM vehicle attitude loops.

1. The main CMG problem areas consist of developing and implementing a responsive and accurate gimbal rate servo loop consisting of optimized mechanical and electronic components. Mechanically, optimization consists of the utilization of the most efficient and linear components possible such as brushless dc torquers, low-compliance—low-deadband gear trains, etc. Electronically, optimization consists of designing servo loop compensation which will allow wide bandwidth control of the gimbal rate itself with the ability to cancel nonlinear mechanical effects introduced by elements such as gear trains. As demonstrated by the performance of the CMG's in spacecraft simulations, the ability of CMG's to accurately control the attitude of a spacecraft is directly dependent on the responsiveness and accuracy of the gimbal rate loops. Consequently, it is highly desirable to develop servo loops approaching the ideal time optimal response characteristics. A CMG unit optimization program is underway at Langley Research Center which will provide time (and energy) optimal second and third generation CMG hardware for attitude control systems of this type.

2. The concept of H-vector or CMG momentum feedback has been found to be an extremely difficult concept to implement with state-of-the-art CMG hardware. The LRC digital simulation has shown that for the required ATM design gains the proposed system will not function satisfactorily. The inner loop compensation-filter scheme discussed in this report will eliminate the inner loop instabilities for the LRC simulation and should have a similar effect for the flight system, but is in no way a substitute for compatible control logic-CMG hardware.

3. Analysis of a linear model of the ATM CMG control system reveals some, but not all, of the mechanisms for vehicle (outer loop) instabilities. One of the causes of vehicle instabilities is excessive phase lag of the control moment with respect to the commanded moment. The excessive phase lag results from low magnitudes of the diagonal elements of the momentum-error-to-control-moment transfer matrix at certain CMG orientations. The incorporation of a filter, termed the Z operator, into the control system compensates for the phase lag and eliminates instabilities in both the linear and nonlinear regions. The modified H-vector control system (Z operator modification) shows sufficient promise to warrant further study although the additional computational requirement coupled with the present computational requirement of this system may exceed a rational limit. The possibility of stabilizing the spacecraft by increasing $K_{SL}H$ and/or narrowing the limits on the inner gimbal angles, as an alternative to the z operator, will be investigated in the future. Also, the response of the system with a CMG failed has been shown to cause outer loop instabilities. This is being investigated and data will be published in the future.

REFERENCES

1. Kurzhals, P. R.: Attitude Control for Manned Space Station. Paper presented at AIAA Fifth Annual Meeting - Philadelphia, Penna., 1968.

2. Will, R. W., Keckler, C. R., Kyle, R. G., and Wooley, C. T.: A Description of a Real Time Digital Computer - Hardware Spacecraft Simulation. NASA TN, 1968.

3. MSFC Memorandum - R-P & VE-SLS-67-42. Preliminary Vibration of the AAP Orbital Workshop. September 11, 1967.

4. Control Law Comparison Study for the ATM/CMG Control System. Bendix Corp. MT-15025, vol. 1, June 13, 1967.

5. CMG Research Project for ATM. Progress Reports for Periods of January 15, 1967 to June 15, 1967.

TABLE I CMG Constants

$$K = 184$$

$$K_L = 6.8$$

$$L = 22 \text{ volts}$$

$$K_T = 0.16 \text{ ft-lb/volt}$$

$$I_T = 0.005 \text{ SLUG ft}^2$$

$$G = 67.6$$

$$K_G = 47,000 \text{ ft-lb/rad}$$

$$K_H = 0.427$$

$$I_\alpha = 4.9 \text{ SLUG ft}^2$$

$$I_\beta = 4.0 \text{ SLUG ft}^2$$

$$T_f = 0.15 \text{ ft-lb}$$

$$\Delta = 1/573 \text{ rad}$$

$$H = 1000 \text{ ft-lb/sec}$$

$$K_B = 1.53 \text{ volts/rad/sec}$$

$$\tau_1 = 0.1 \text{ sec}$$

$$\tau_2 = 1.0 \text{ sec}$$

$$\tau_3 = 0.5 \text{ sec}$$

$$\tau_4 = 0.003 \text{ sec}$$

$$\tau_5 = 0.02 \text{ sec}$$

$$\tau_6 = 0.0033 \text{ sec}$$

TABLE II

SUMMARY OF ACQUISITION MANEUVERS, H-VECTOR WITH ISOGONAL CORRECTION, MSFC COORDINATES

$\beta_L = \pm 80°$ Initial non-zero Gimbal angles, deg.	Initial Spacecraft Attitude errors, rad. $\theta_x = \theta_y = \theta_z$	Stability	Acquisition Time, sec.
$\alpha_3 = 90°, \beta_2 = 80°$	$.8725 \times 10^{-3}$	temporarily unstable x	90
$\alpha_3 = 90°, \beta_2 = 75°$	$.8725 \times 10^{-3}$	temporarily unstable x	75
$\alpha_1 = 90°, \beta_3 = 75°$	$.8725 \times 10^{-3}$	temporarily unstable y	85
$\alpha_2 = 90°, \beta_1 = 70°$	$.8725 \times 10^{-3}$	stable	60
$\alpha_2 = 90°, \beta_1 = 75°$	$.8725 \times 10^{-3}$	temporarily unstable z	65
$\beta_2 = \beta_3 = 70°$	$.8725 \times 10^{-3}$	unstable x	--
$\beta_2 = 70°, \beta_3 = -70°$	$.8725 \times 10^{-3}$	stable	45
$\beta_1 = \beta_3 = 70°$	$.8725 \times 10^{-3}$	unstable y	--
$\beta_1 = \beta_2 = 70°$	$.8725 \times 10^{-3}$	temporarily unstable z	220
$\alpha_1 = 90°$	$.8725 \times 10^{-3}$	stable	55
$\alpha_1 = 90°$	$.8725 \times 10^{-2}$	temporarily unstable y	280
$\alpha_1 = -90°$	$.8725 \times 10^{-2}$	unstable y	--
$\alpha_2 = 90°$	$.8725 \times 10^{-3}$	stable	45
$\alpha_2 = 90°$	$.8725 \times 10^{-2}$	stable	200
$\alpha_3 = 90°$	$.8725 \times 10^{-2}$	stable	160
$\alpha_3 = -90°$	$.8725 \times 10^{-2}$	unstable x	--
$\alpha_2 = -90°$	$.8725 \times 10^{-2}$	unstable y & z	--

TABLE III

SUMMARY OF ACQUISITION MANEUVERS, LRC COORDINATES

Control Law	$\beta_L = \pm 70^\circ$ Initial Non-zero Gimbal Angles, deg.	Initial Spacecraft Attitude Errors, rad. $\vartheta_x = \vartheta_y = \vartheta_z$	Stability	Acquisition Time, sec.
New (as per Fig. 41)	$\alpha_1 = \alpha_2 = \alpha_3 = 45^\circ$	$.8725 \times 10^{-3}$	stable	30
Old (as per Fig. 29)	$\alpha_1 = \alpha_2 = \alpha_3 = 45^\circ$	$.8725 \times 10^{-3}$	stable	40
New	$\alpha_2 = 90^\circ, \beta_3 = 70^\circ$	$.8725 \times 10^{-3}$	stable	40
Old	$\alpha_2 = 90^\circ, \beta_3 = 70^\circ$	$.8725 \times 10^{-3}$	stable	25
New	$\alpha_3 = 90^\circ, \beta_1 = 70^\circ$	$.8725 \times 10^{-3}$	stable, initial x overshoot	60
Old	$\alpha_3 = 90^\circ, \beta_1 = 70^\circ$	$.8725 \times 10^{-3}$	unstable x and y	--
New	$\alpha_1 = 90^\circ, \beta_2 = 70^\circ$	$.8725 \times 10^{-3}$	stable, initial x overshoot	70
Old	$\alpha_1 = 90^\circ, \beta_2 = 70^\circ$	$.8725 \times 10^{-3}$	temporarily unstable x and y	85
New	$\beta_2 = \beta_3 = 70^\circ$	$.8725 \times 10^{-3}$	stable	40
Old	$\beta_2 = \beta_3 = 70^\circ$	$.8725 \times 10^{-3}$	unstable x	--
New	$\beta_2 = \beta_3 = 70^\circ$	$-.8725 \times 10^{-3}$	stable	35
Old	$\beta_2 = \beta_3 = 70^\circ$	$-.8725 \times 10^{-3}$	unstable x	--
New	$\beta_1 = \beta_3 = 70^\circ$	$.8725 \times 10^{-3}$	stable	50
Old	$\beta_1 = \beta_3 = 70^\circ$	$.8725 \times 10^{-3}$	unstable y	--
New	$\beta_1 = \beta_2 = 70^\circ$	$.8725 \times 10^{-3}$	stable	45
Old	$\beta_1 = \beta_2 = 70^\circ$	$.8725 \times 10^{-3}$	temporarily unstable z	68

TABLE III,-CONCLUDED

Control Law	$\beta_L = \pm\,70^\circ$ Initial Non-zero Gimbal Angles, deg.	Initial Spacecraft Attitude Errors, rad. $\theta_x = \theta_y = \theta_z$	Stability	Acquisition Time, sec.
New	$\beta_1 = \beta_2 = 70^\circ$	$-.8725 \times 10^{-3}$	stable	35
Old	$\beta_1 = \beta_2 = 70^\circ$	$-.8725 \times 10^{-3}$	temporarily unstable z	70
New	$\alpha_1 = 90^\circ, \beta_2 = 70^\circ$	10^{-4}	stable	70
Old	$\alpha_1 = 90^\circ, \beta_2 = 70^\circ$	10^{-4}	stable, initial x, y, z overshoot	45
Old	$\alpha_1 = 90^\circ, \beta_2 = 70^\circ$	10^{-5}	stable	110
Old	$\alpha_1 = 90^\circ, \beta_2 = 70^\circ$	1.5×10^{-5}	temporarily unstable	160
New	$\alpha_1 = 90^\circ$	$.8725 \times 10^{-2}$	stable	110
Old	$\alpha_1 = 90^\circ$	$.8725 \times 10^{-3}$	unstable y	--

TABLE IV.- Conversion Table

U. S. Customary Units	S. I. Units
inch	.0254 meter
foot-pound	1.356 Newton-meter
pound	4.448 Newton
slug-foot^2	1.356 kilogram-meter^2
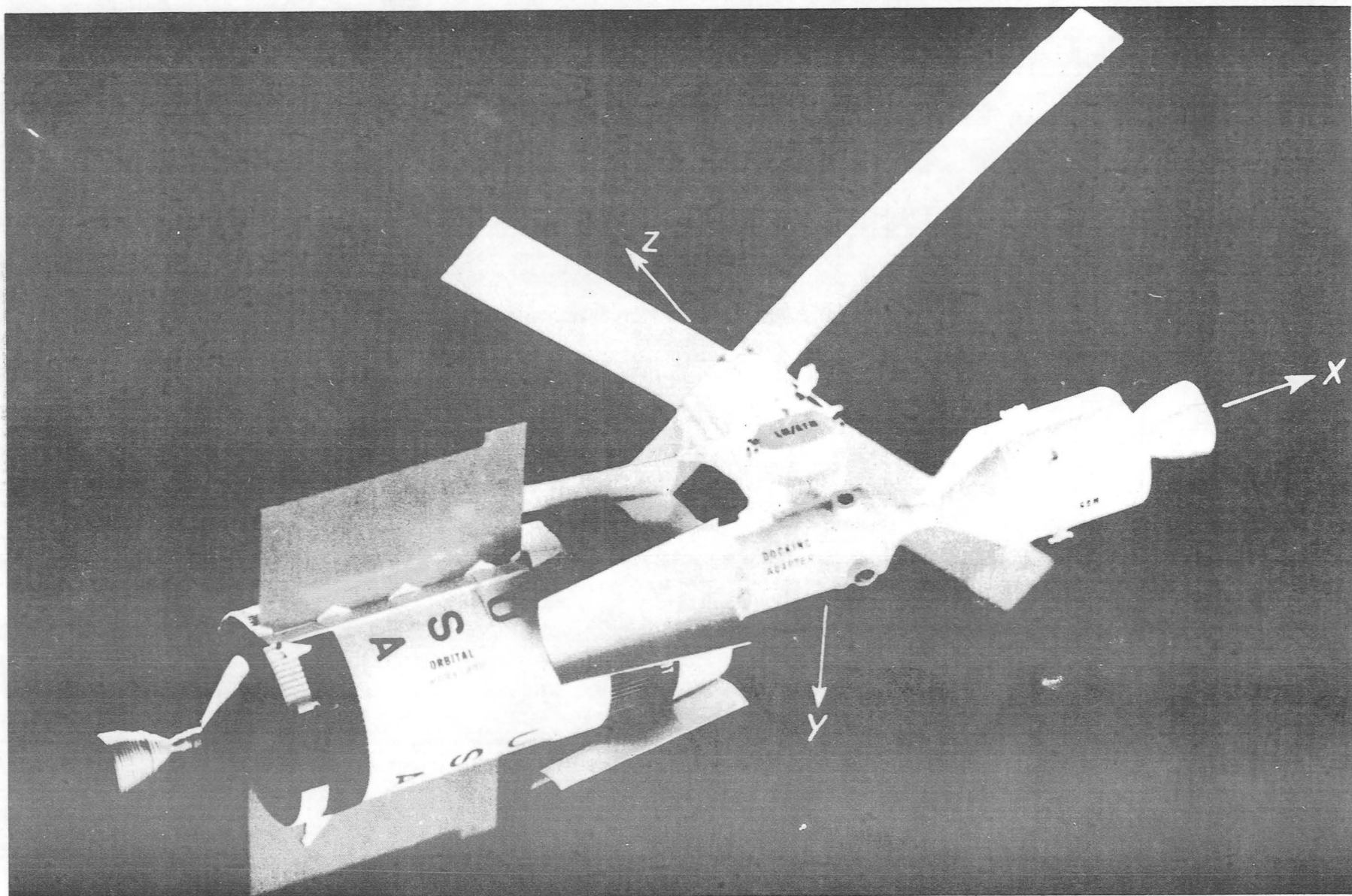
Figure 1.-   APOLLO TELESCOPE MOUNT CLUSTER

CMG UNITS

TEST STAND

Figure 2.- CMG SYSTEM TEST SETUP

LRC Coordinates

H(2)

H(3)

z

y

x

H(1)

α_3 β_3 β_2 α_2 α_1 β_1

H(1) = H(2) = H(3) = 2000 ft-lb-sec
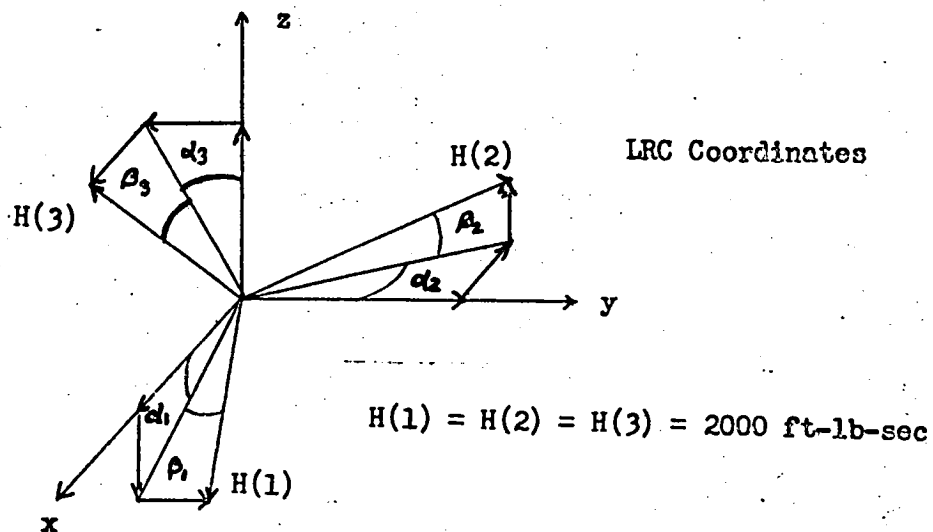
$$H_x = H(\cos\alpha_1 \cos\beta_1 - \sin\alpha_2 \cos\beta_2 + \sin\beta_3)$$

$$H_y = H(\cos\alpha_2 \cos\beta_2 - \sin\alpha_3 \cos\beta_3 + \sin\beta_1)$$

$$H_z = H(\cos\alpha_3 \cos\beta_3 - \sin\alpha_1 \cos\beta_1 + \sin\beta_2)$$

MSFC Coordinates

z

H(3)

y

H(2)

H(1)

x

β_3 α_3 α_2 β_2 α_1 β_1

H(1) = H(2) = H(3) = 2000 ft-lb-sec

$$H_x = H(\cos\alpha_1 \cos\beta_1 - \sin\alpha_3 \cos\beta_3 - \sin\beta_2)$$
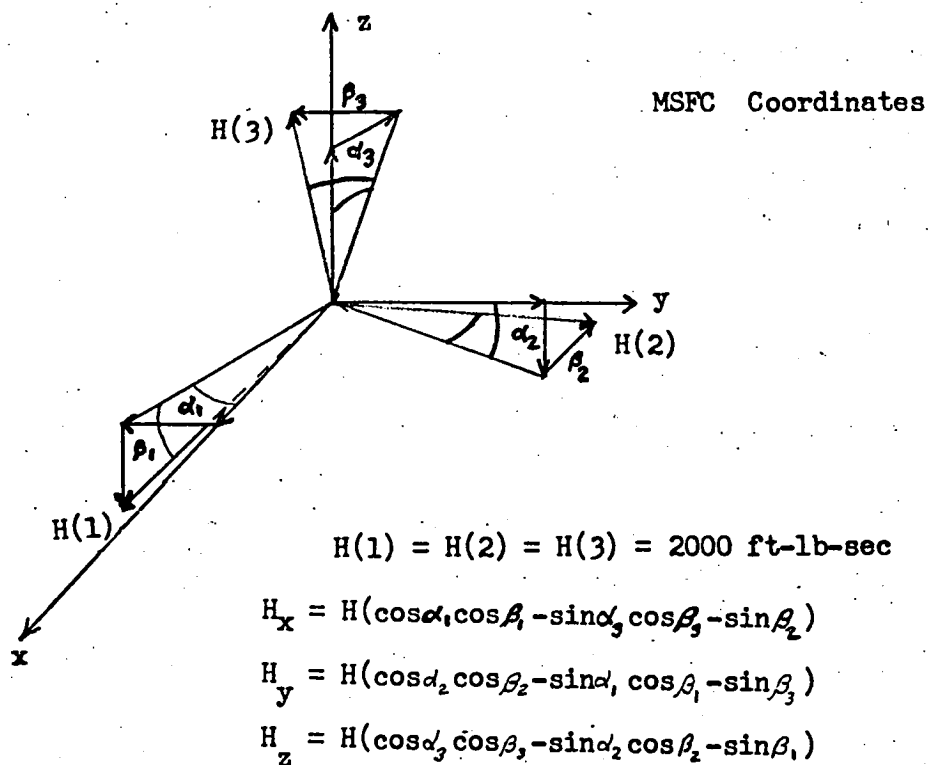
$$H_y = H(\cos\alpha_2 \cos\beta_2 - \sin\alpha_1 \cos\beta_1 - \sin\beta_3)$$

$$H_z = H(\cos\alpha_3 \cos\beta_3 - \sin\alpha_2 \cos\beta_2 - \sin\beta_1)$$

Figure 3.-   Control moment gyro orientation.
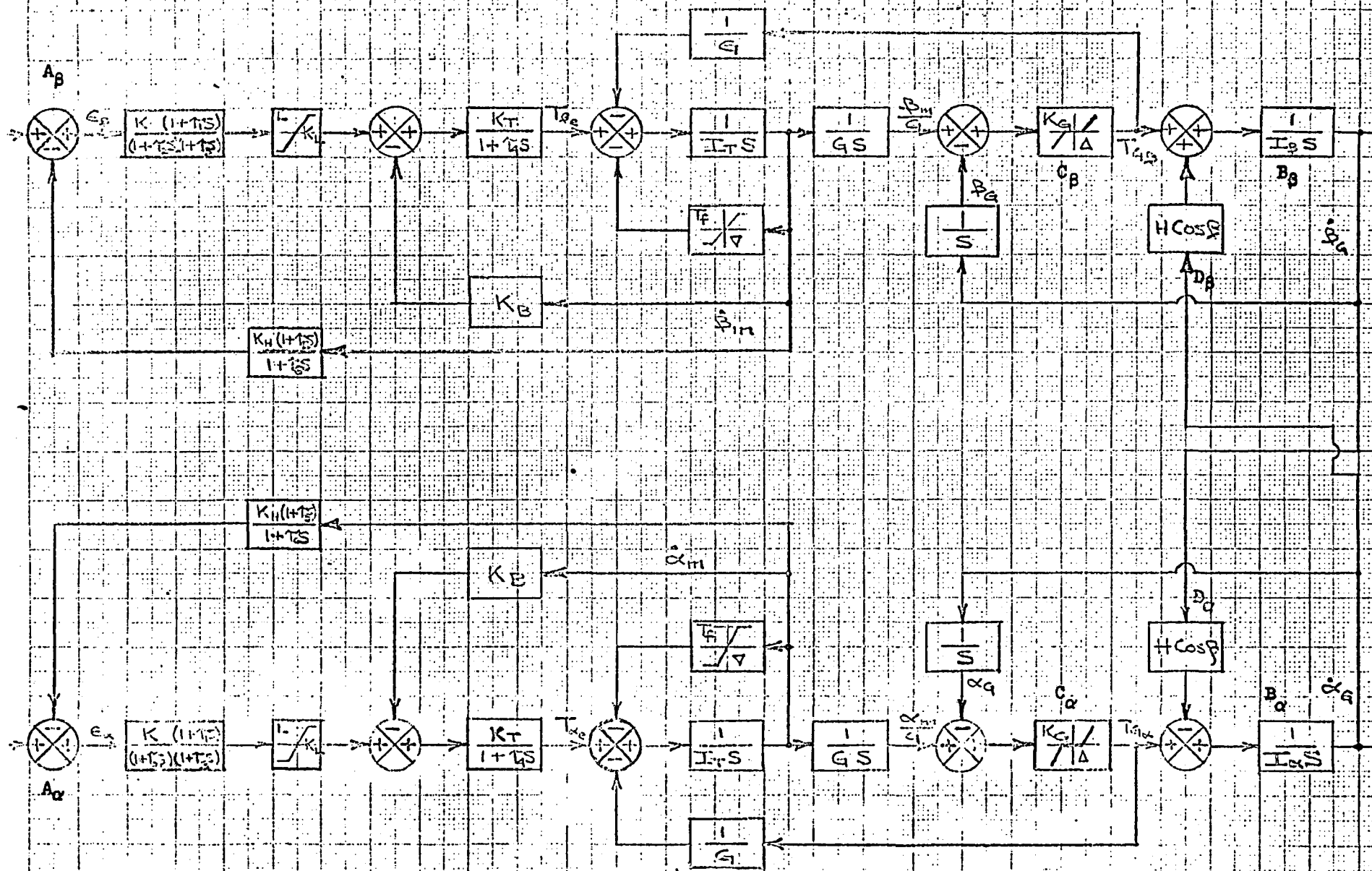
Figure 4.-CG System.
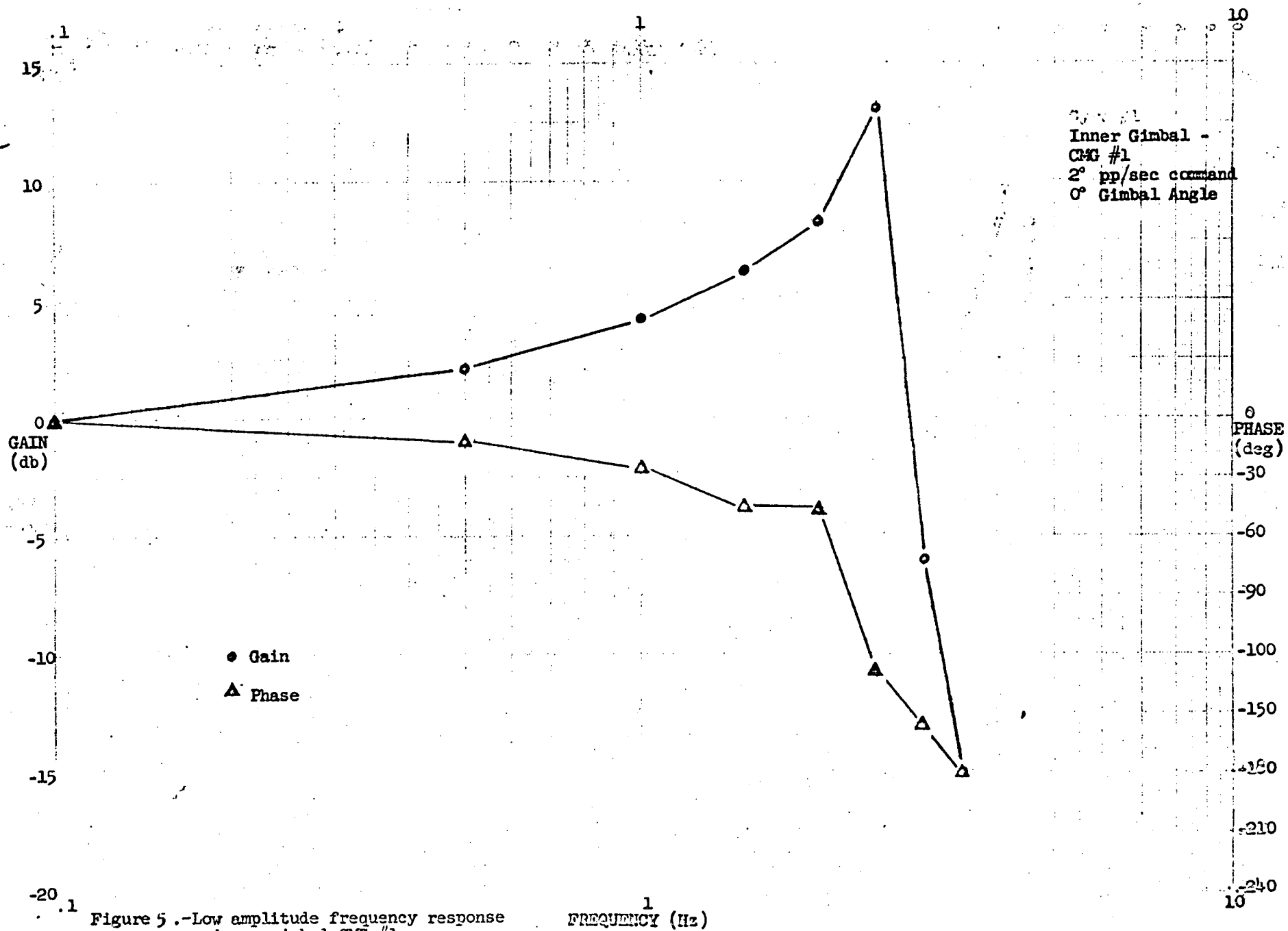
Figure 5.-Low amplitude frequency response - inner gimbal CMG #1.
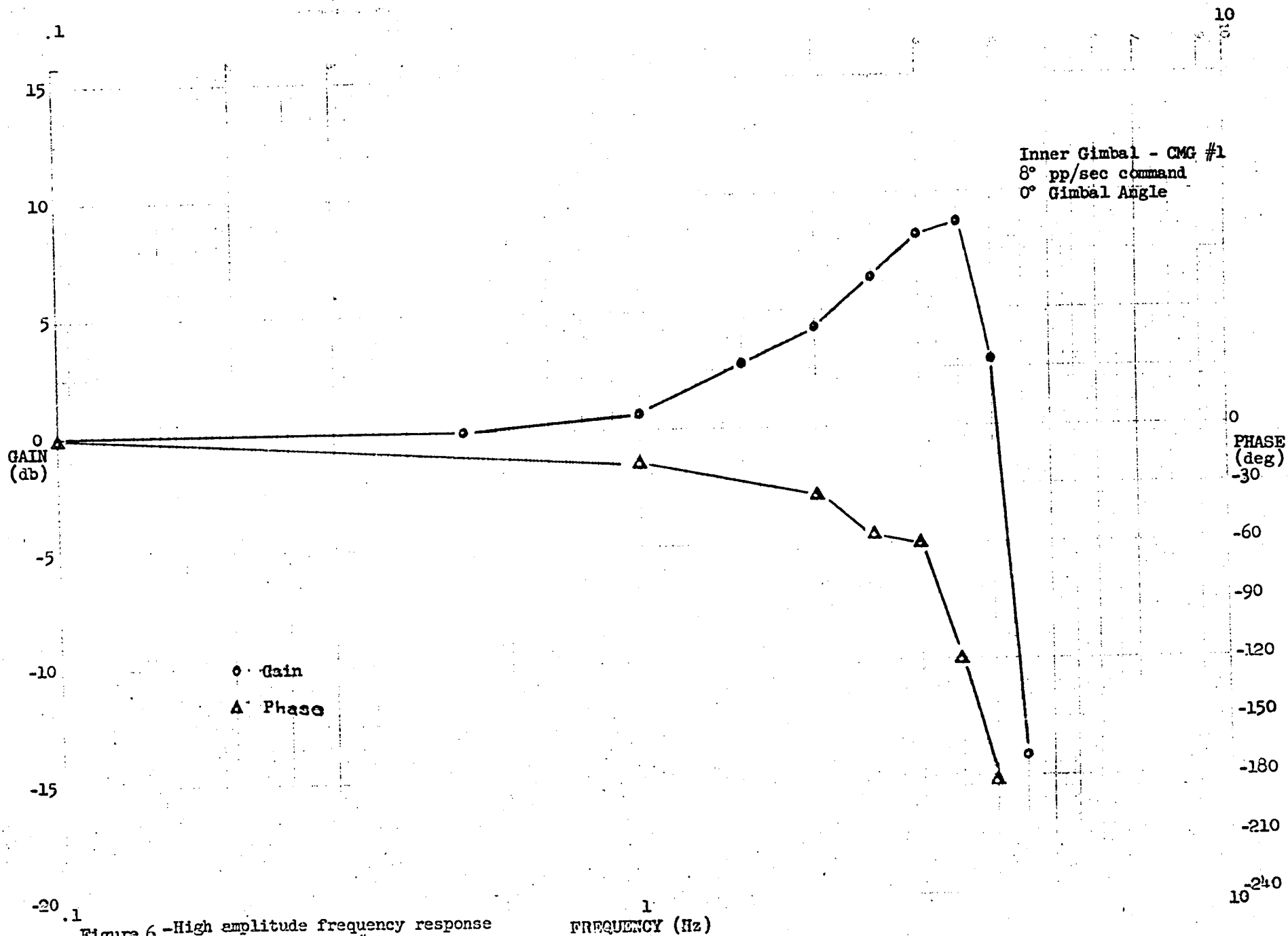
Figure 6.-High amplitude frequency response
- inner gimbal CMG #1.
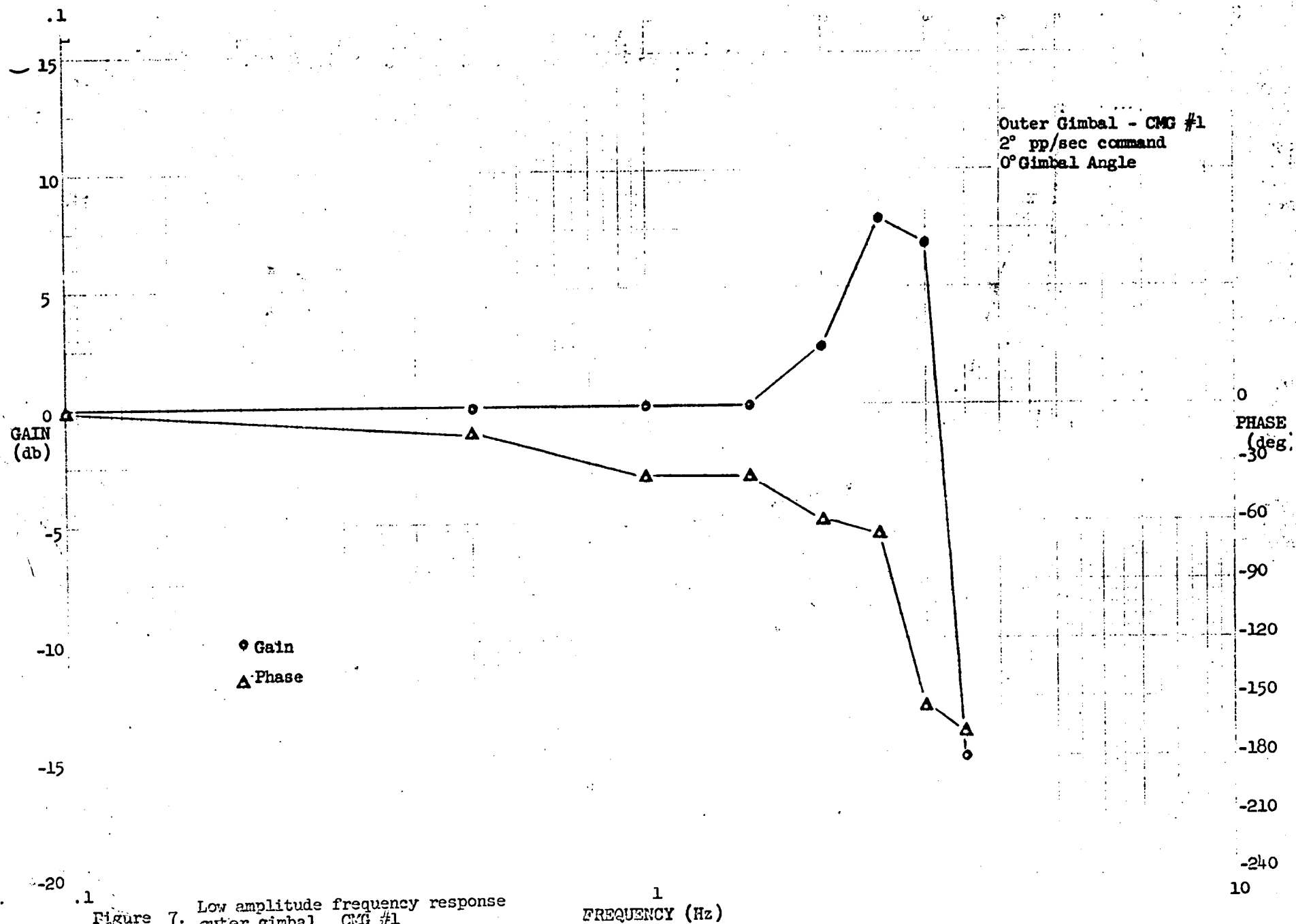
Figure 7. Low amplitude frequency response outer gimbal CMG #1
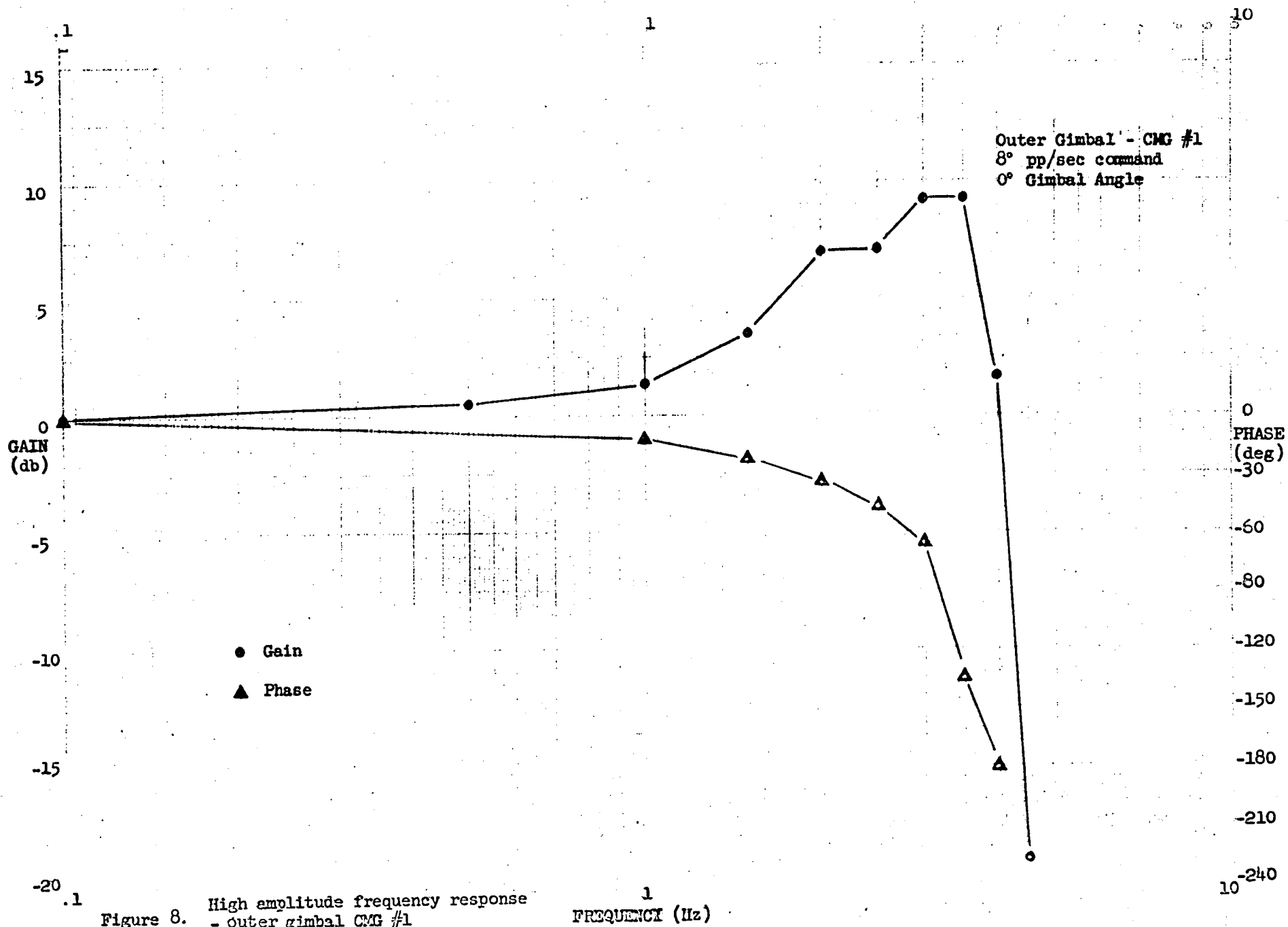
Figure 8.   High amplitude frequency response – outer gimbal CMG #1

Figure 9. Low amplitude frequency response - inner gimbal CMG #2

Figure 10. High amplitude frequency response
- inner gimbal CMG #2
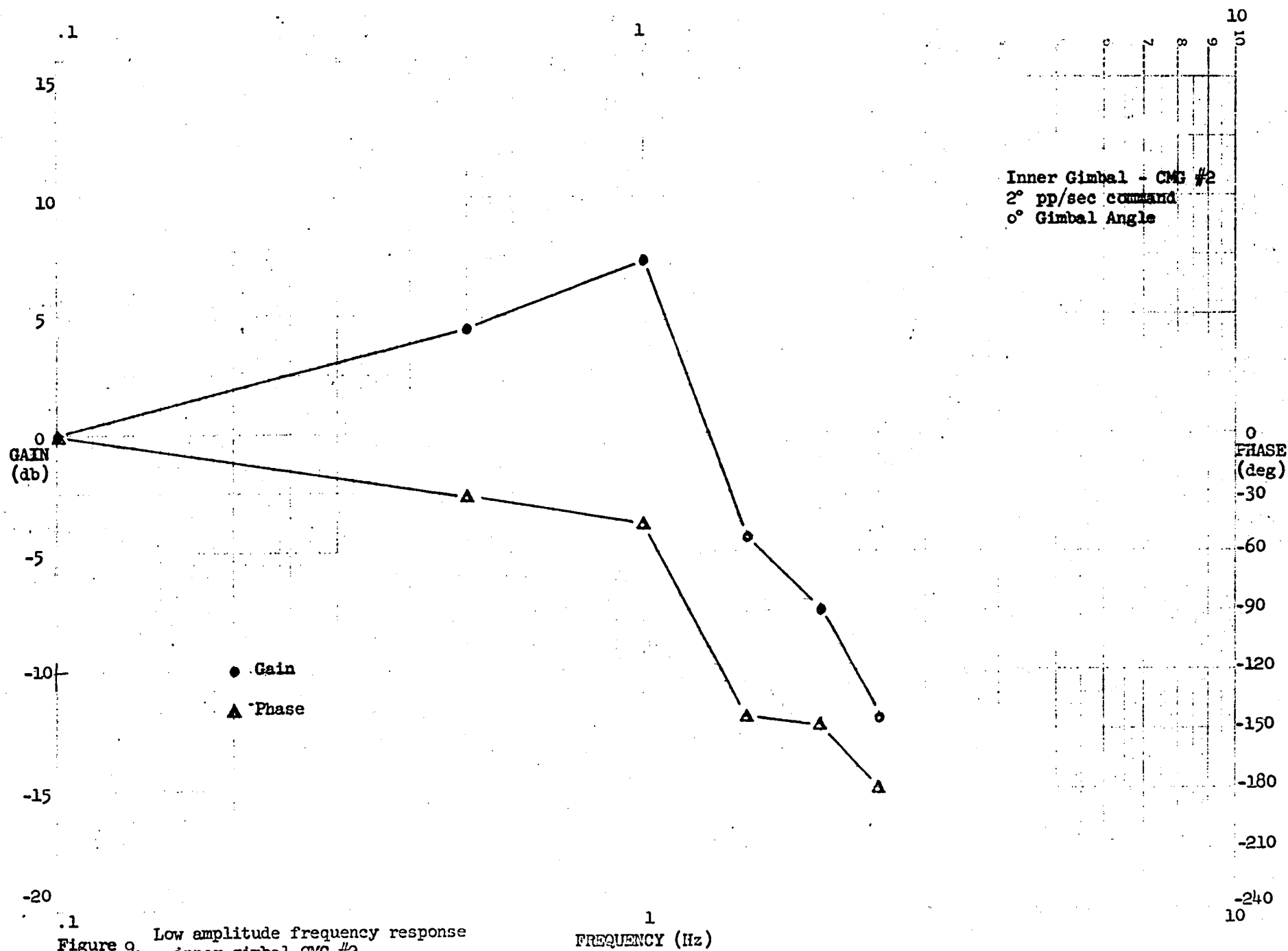
Figure 11. Low amplitude frequency response — inner gimbal #2
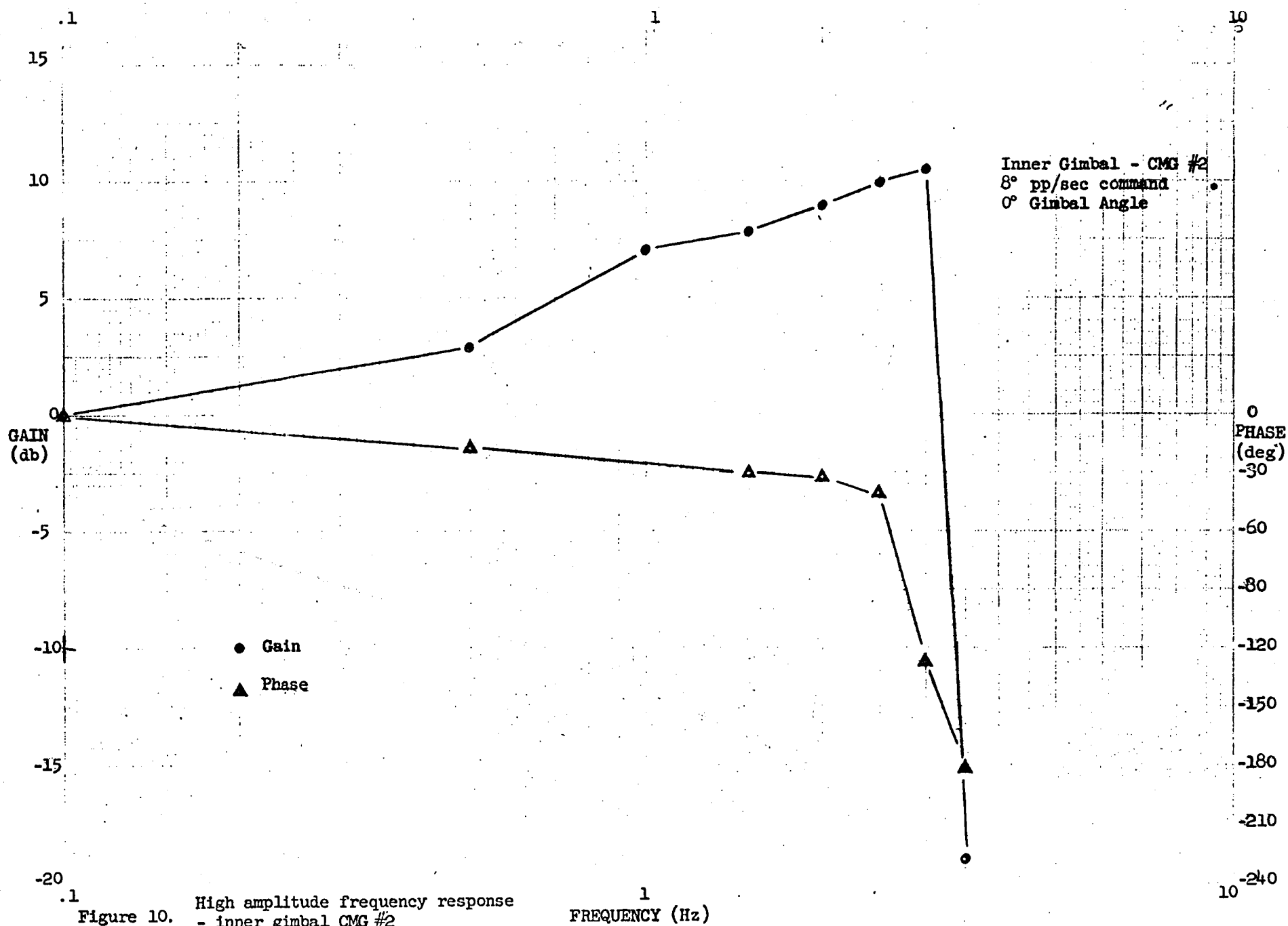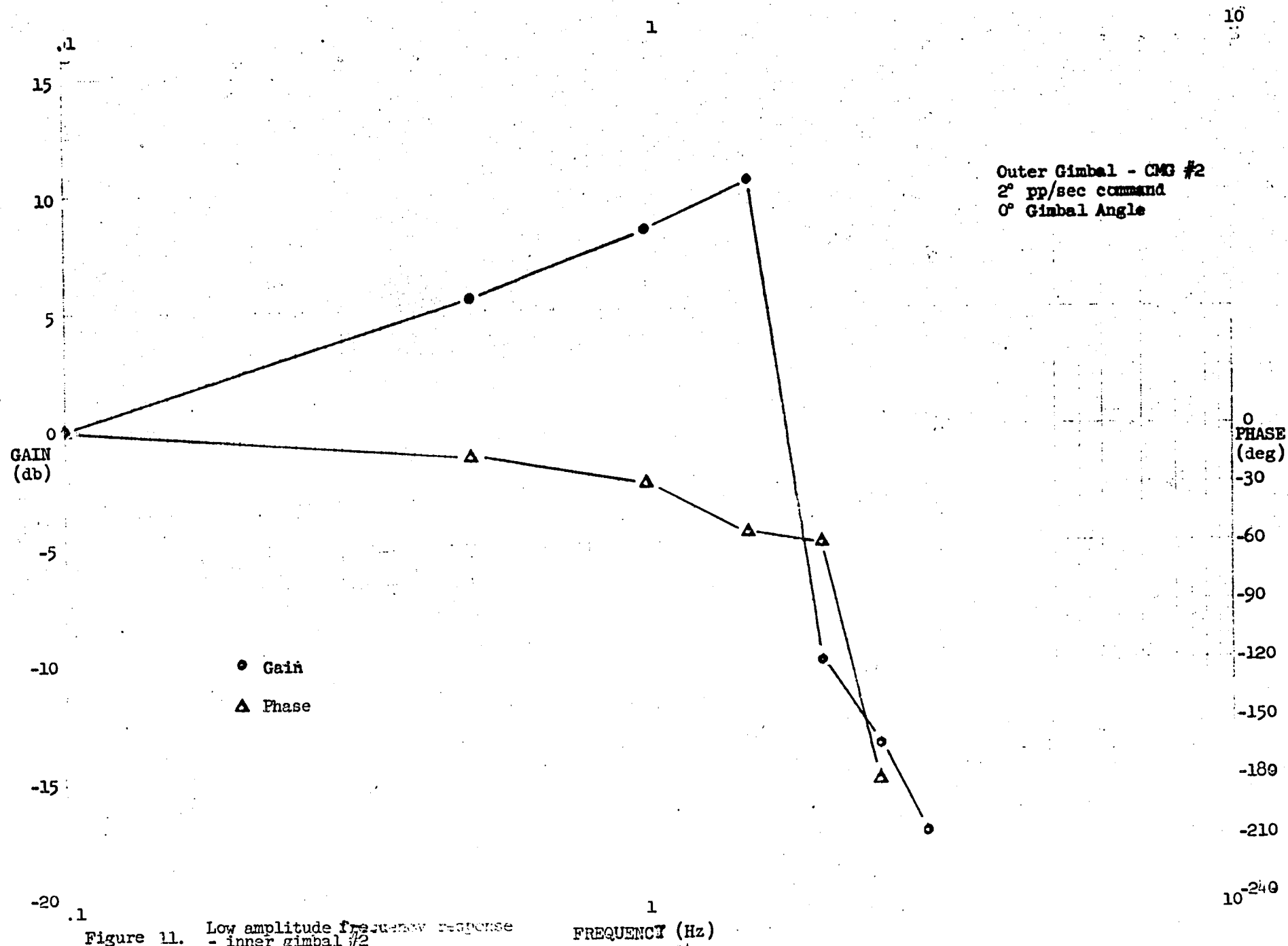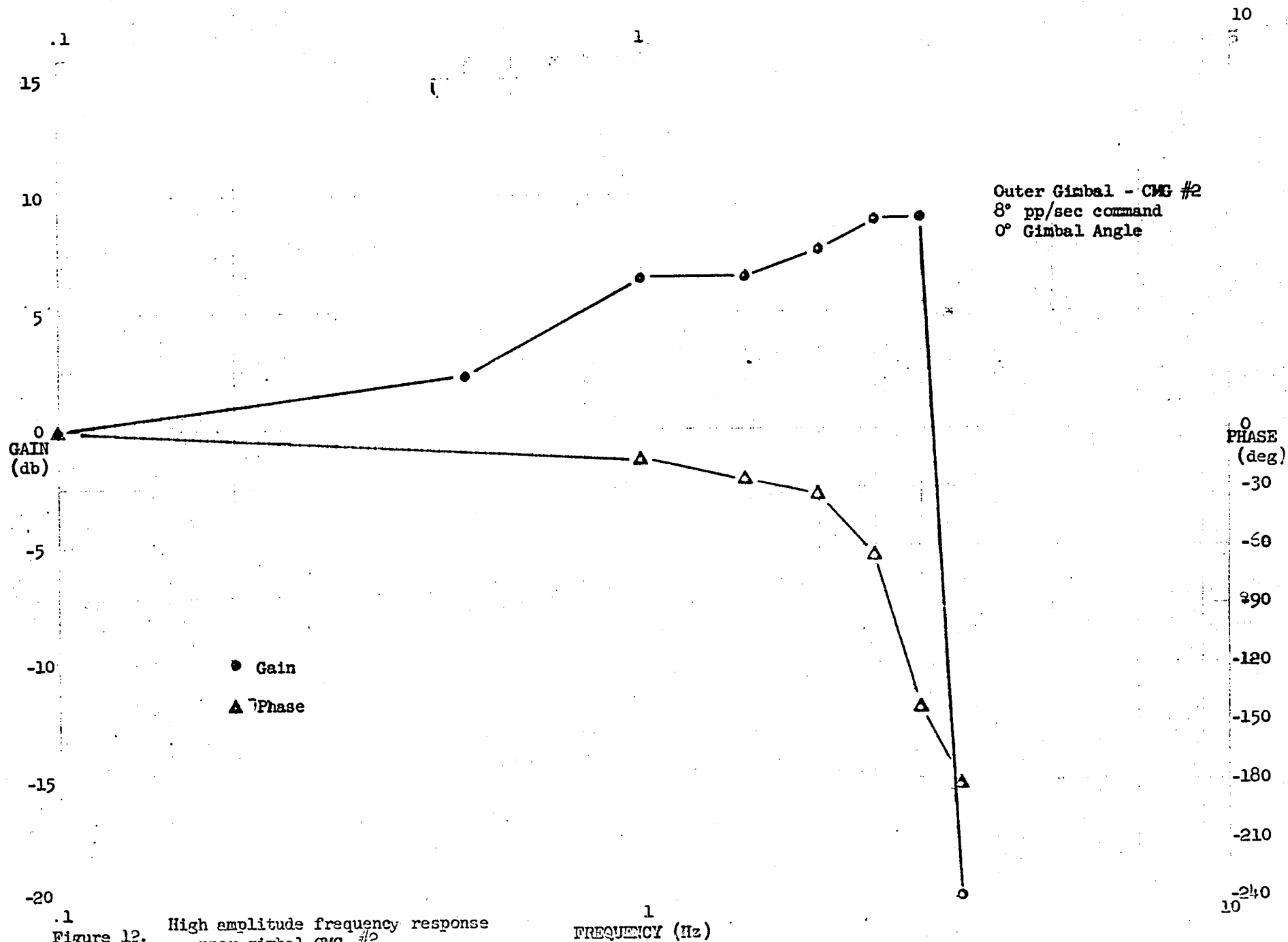
Figure 12. High amplitude frequency response – inner gimbal CMG #2

Figure 13. Low amplitude frequency response — inner gimbal CMG #3

Figure 14. High amplitude frequency response - inner gimbal CMG #3
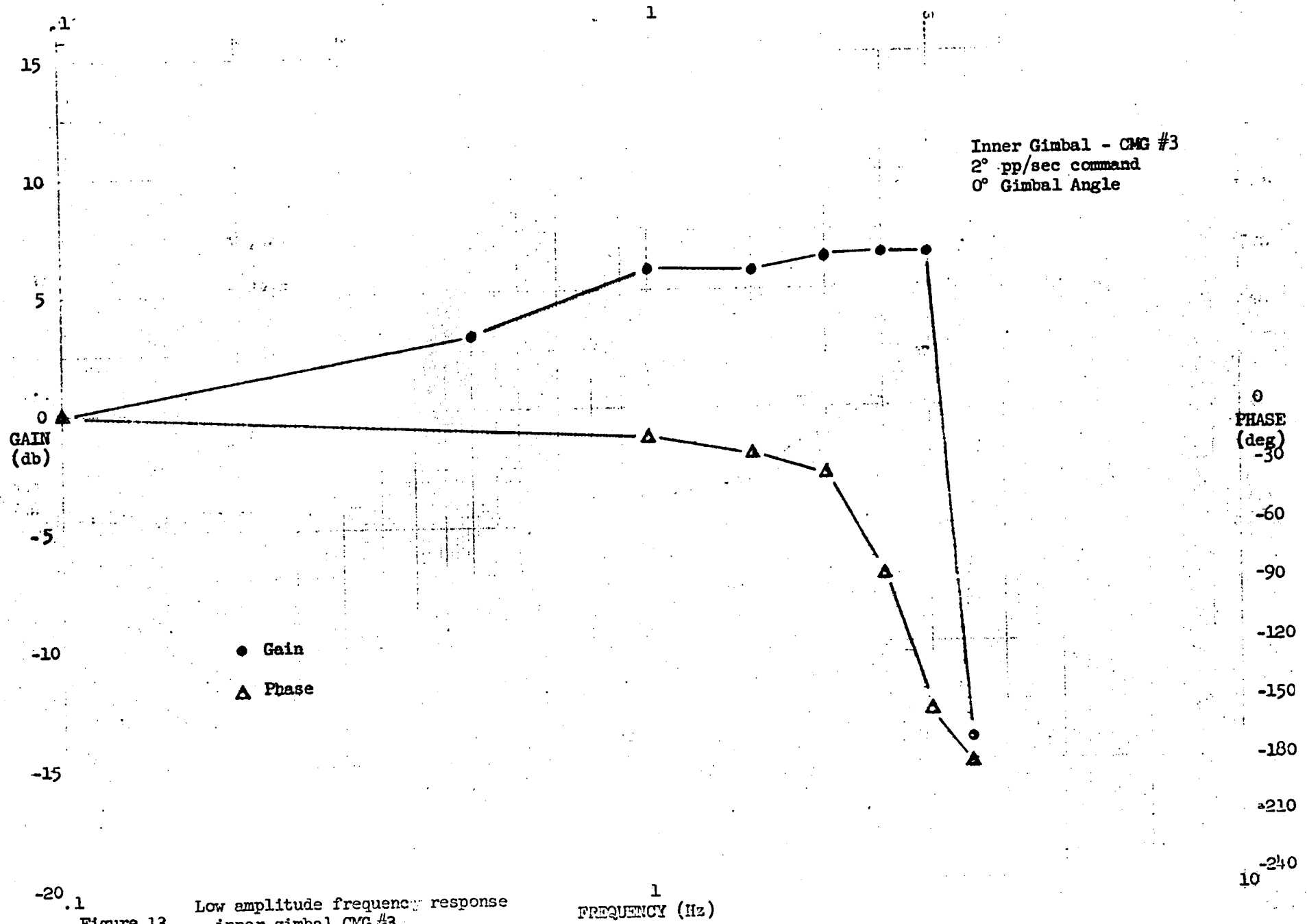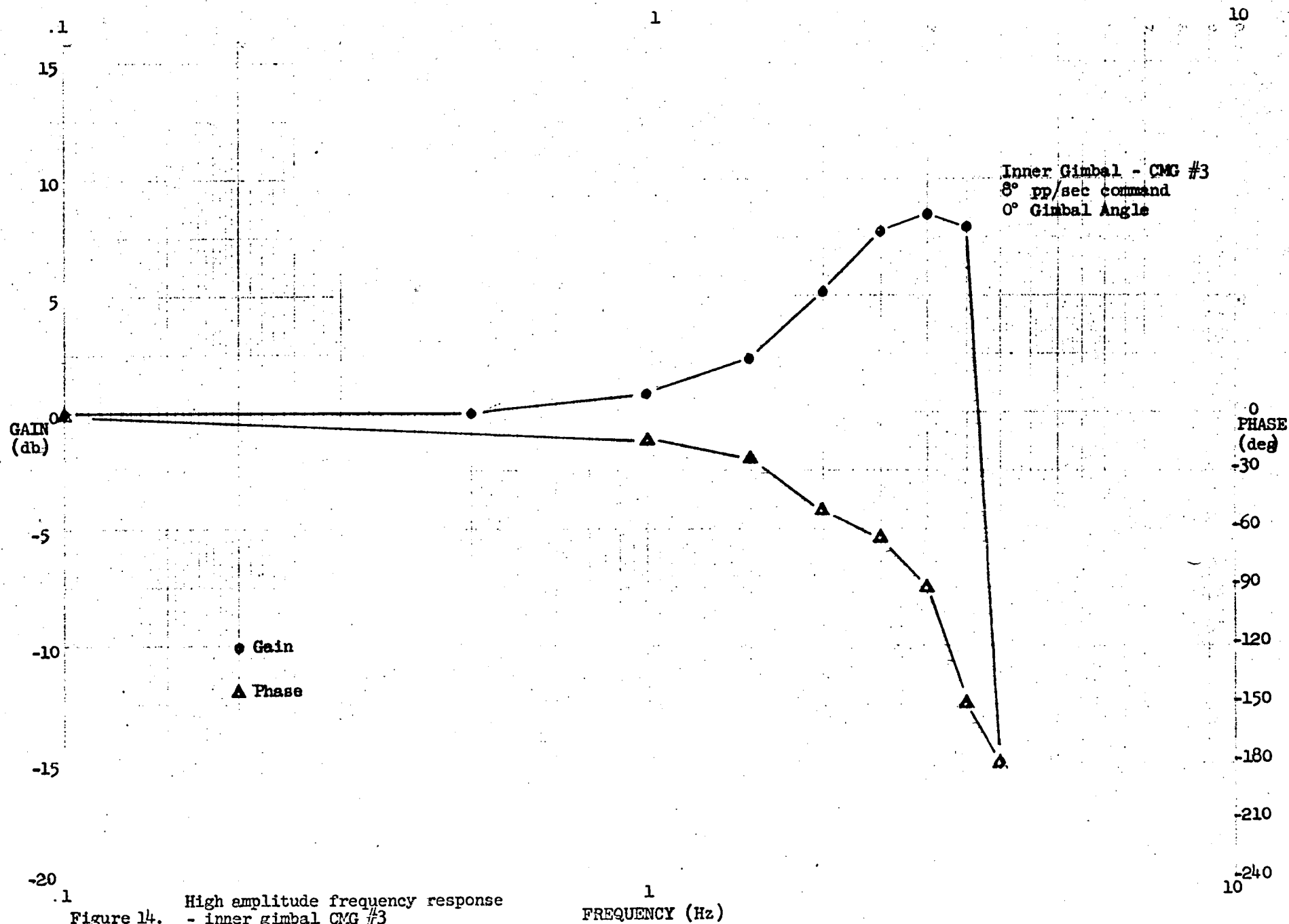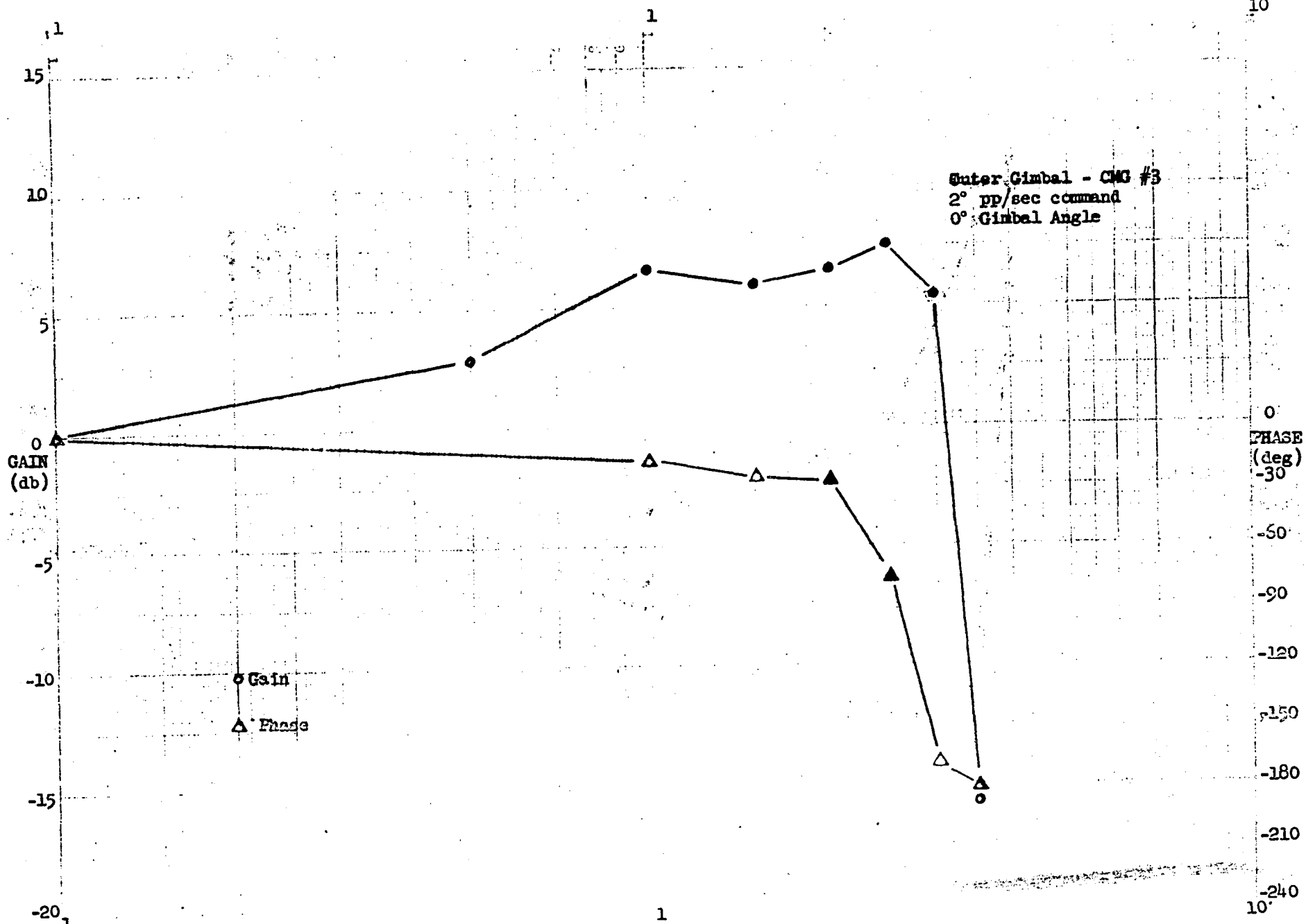
Figure 15. Low amplitude frequency response - inner gimbal CMG #3

Figure 16.   High amplitude frequency response - inner gimbal CMG #3

Figure 17. Low amplitude frequency response – inner gimbal CMG #3

Figure 18. High amplitude frequence response – inner gimbal CMG #3

Figure 19. Low amplitude frequency response - inner gimbal - CMG #3
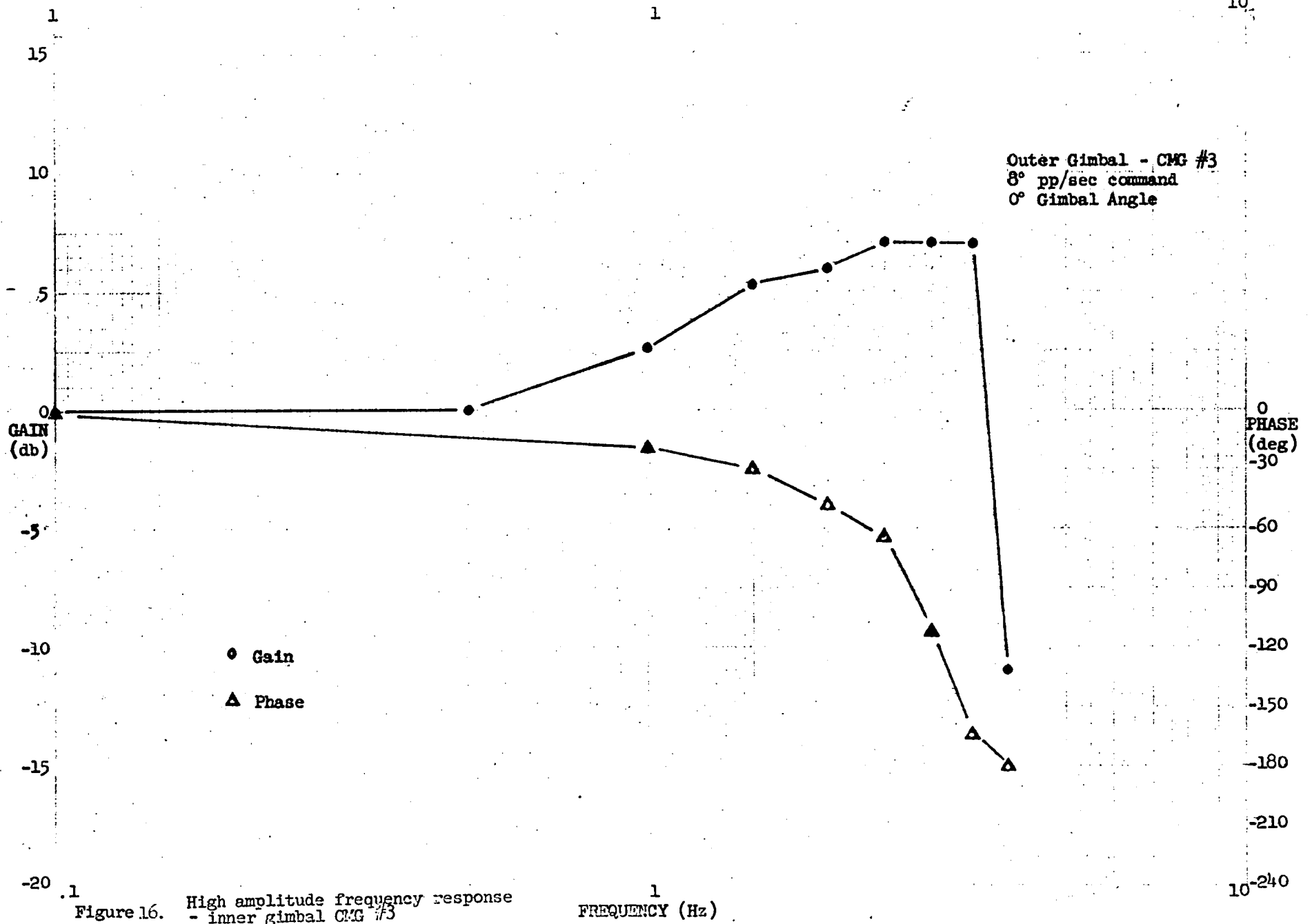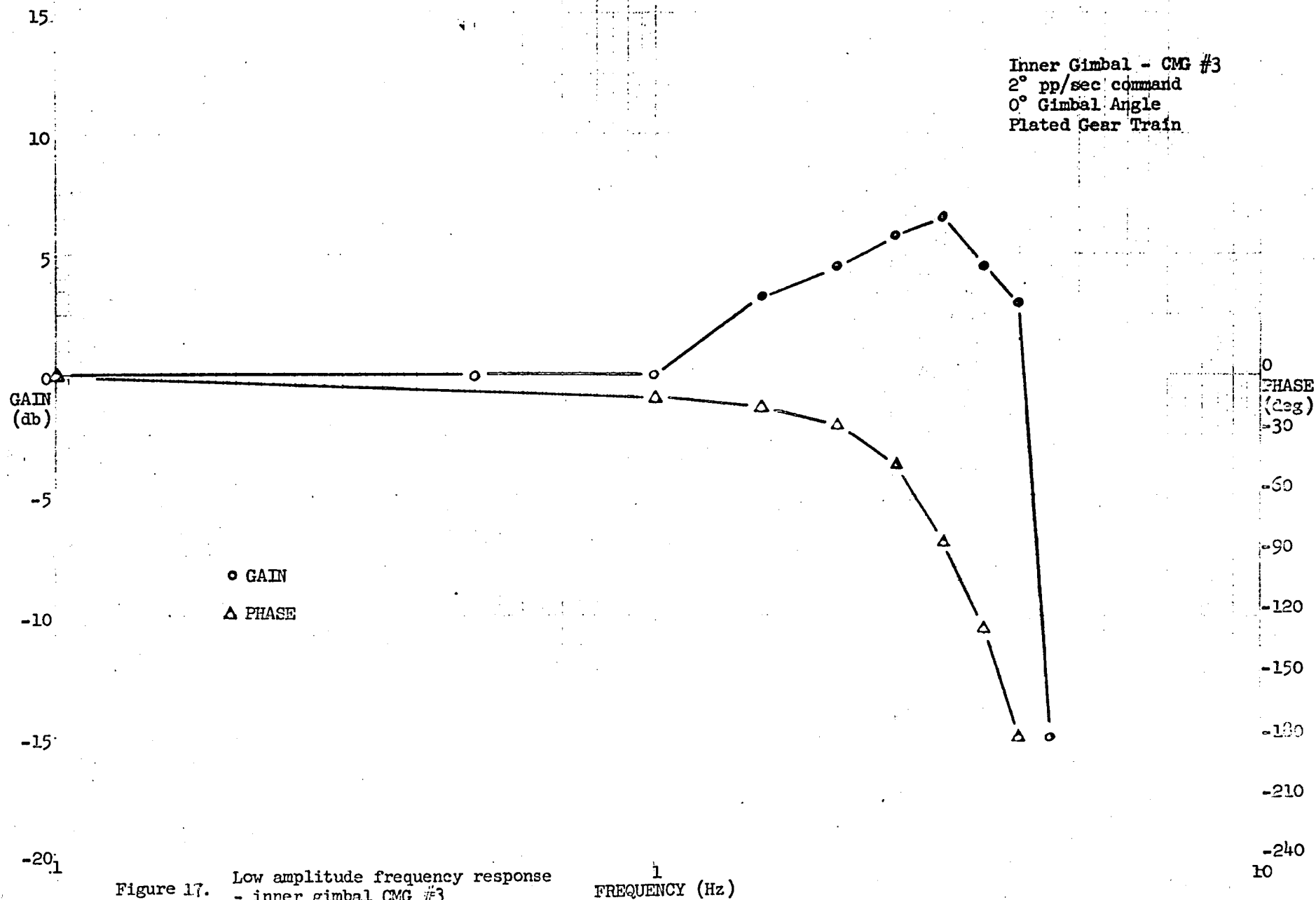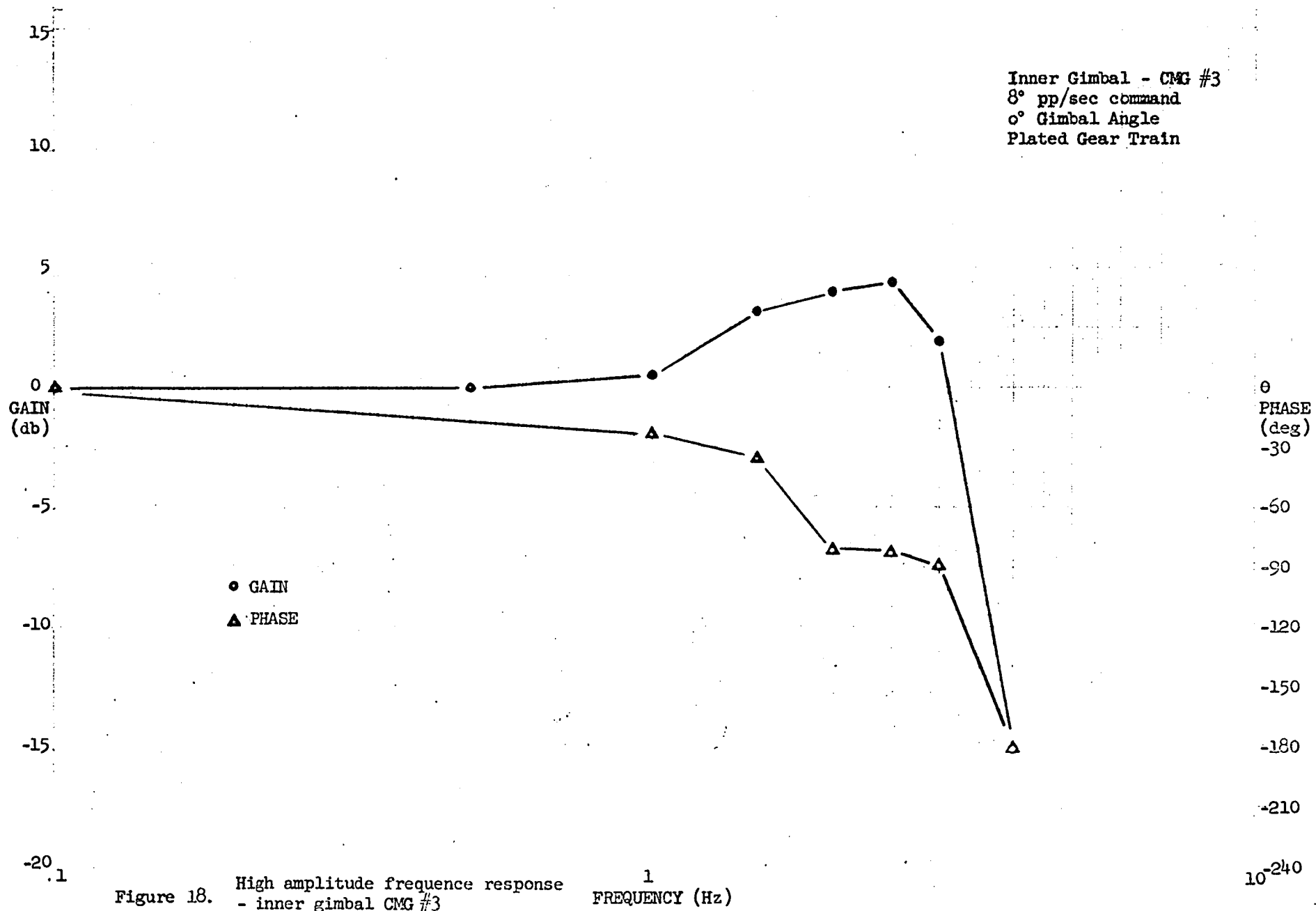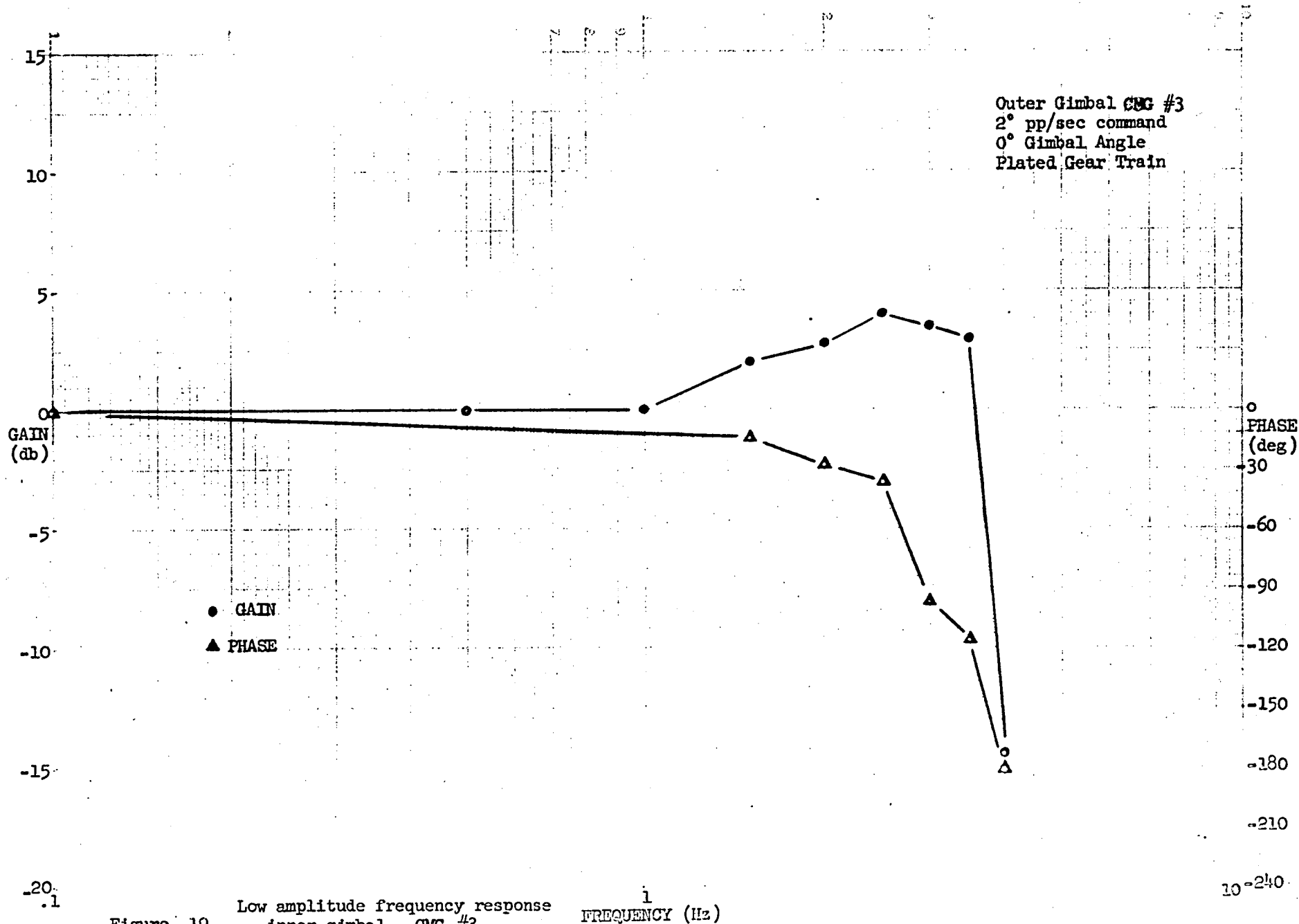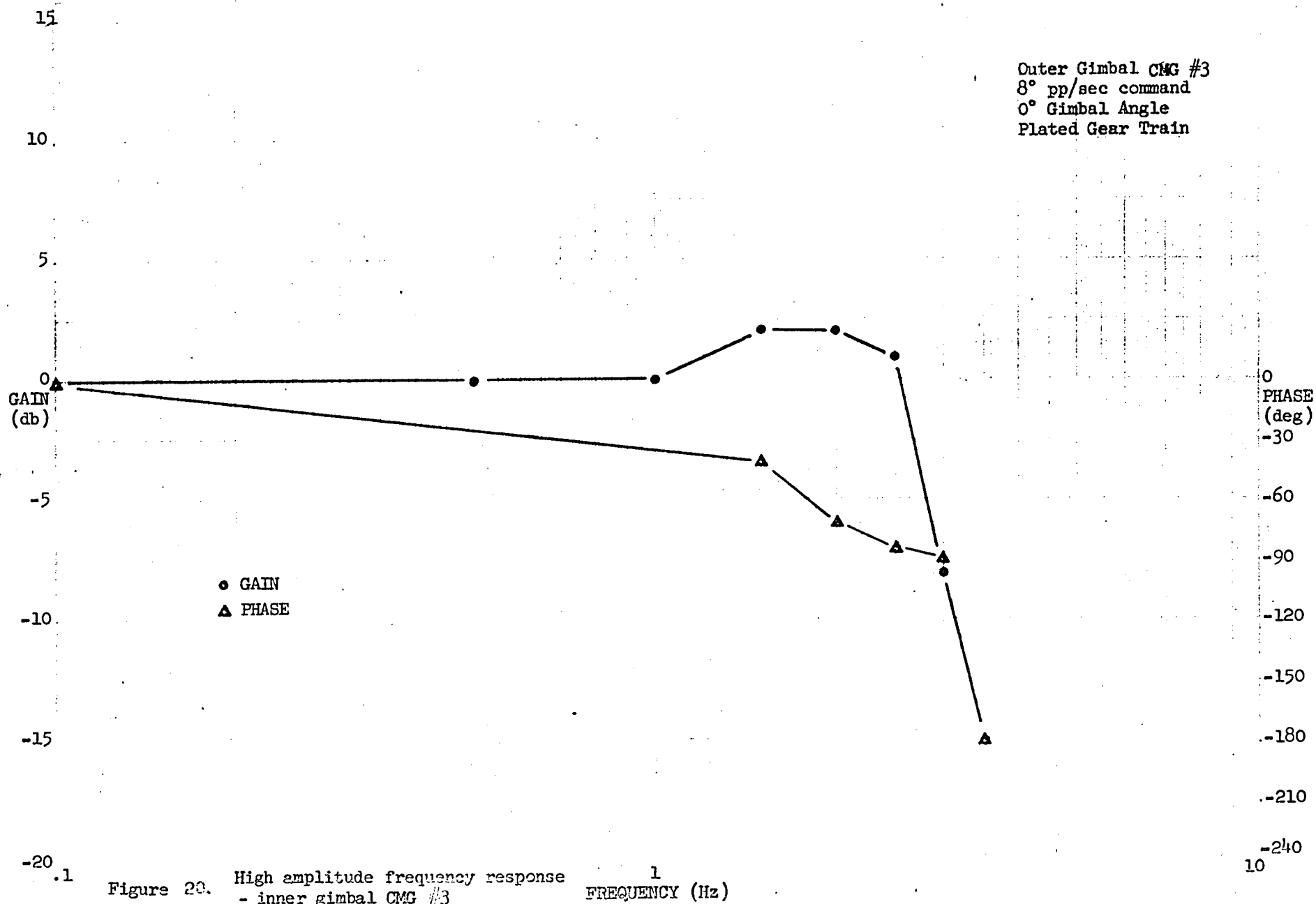
Figure 20. High amplitude frequency response – inner gimbal CMG #3
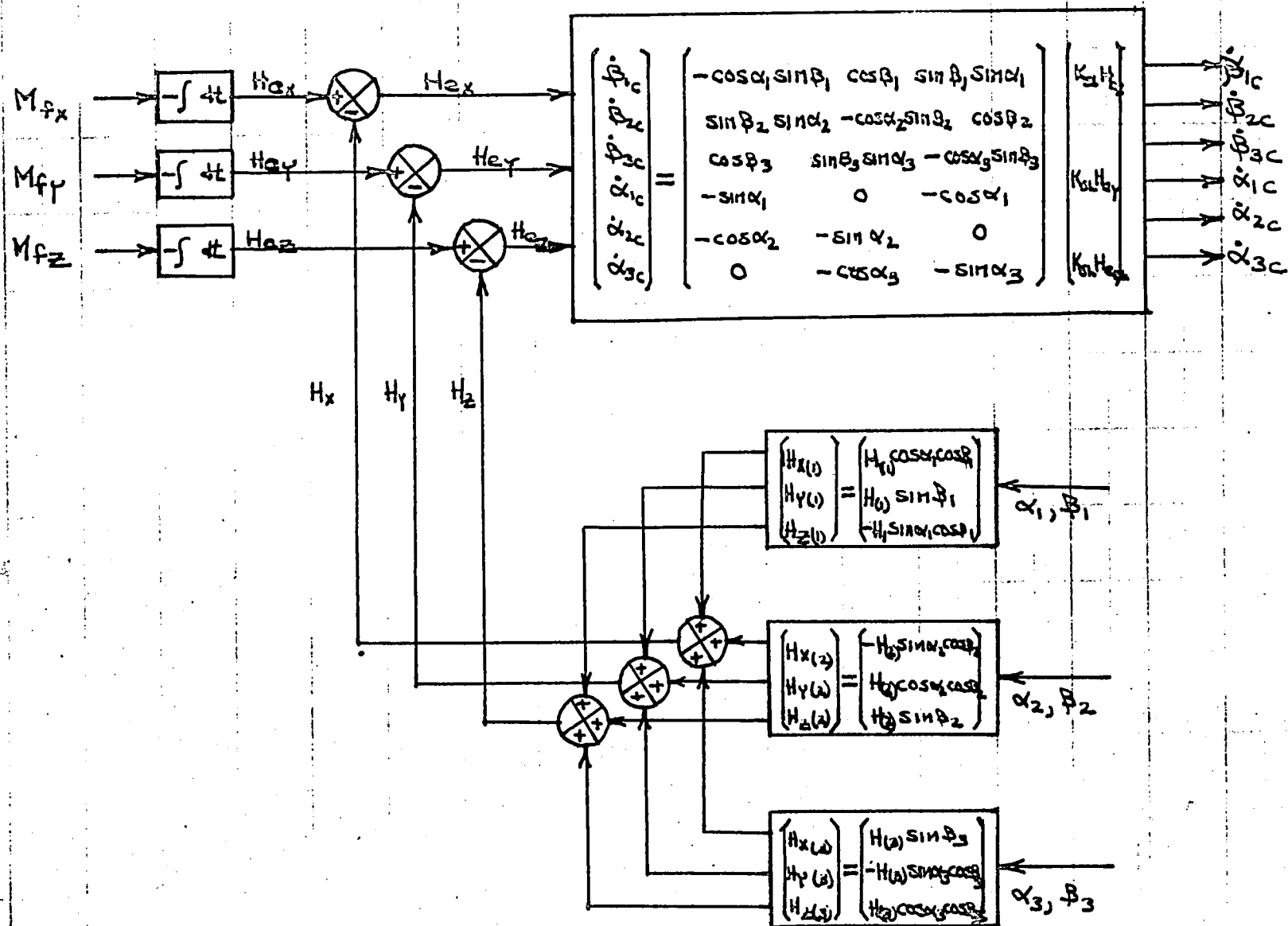
Figure 21.— H-Vector inner loop.
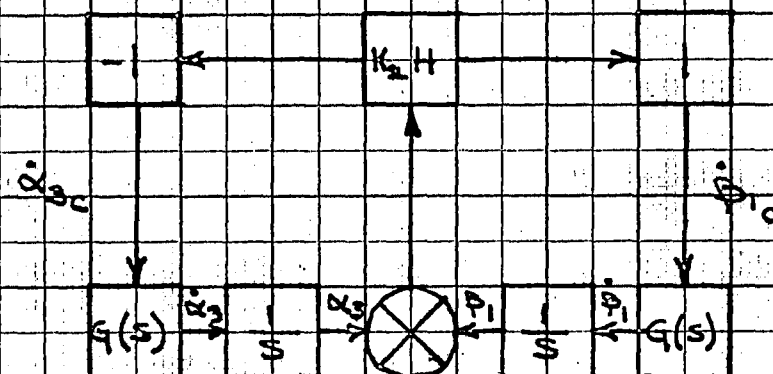
(a) Equations (3) with CMG
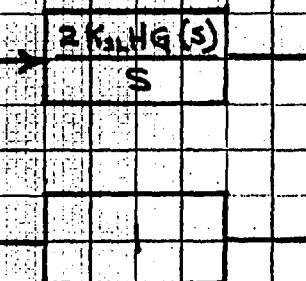
(b) Simplified Loop

Figure 22.— Quasi-Linear Momentum Feedback Loop.
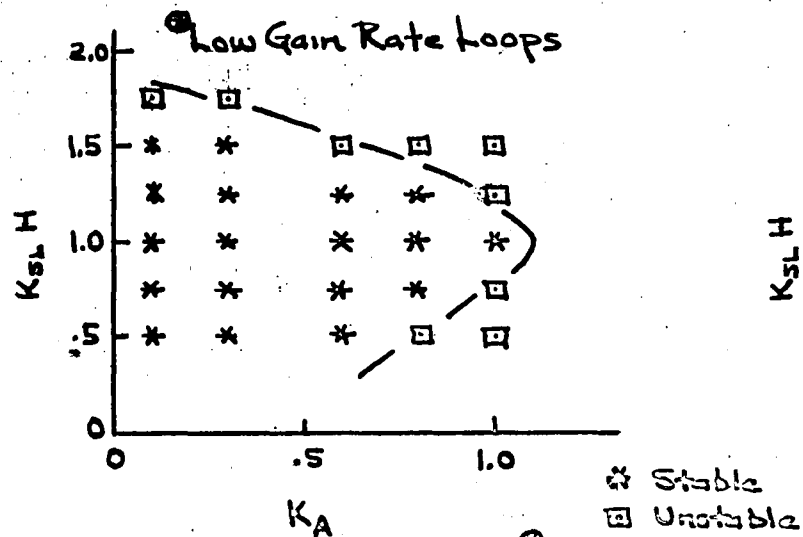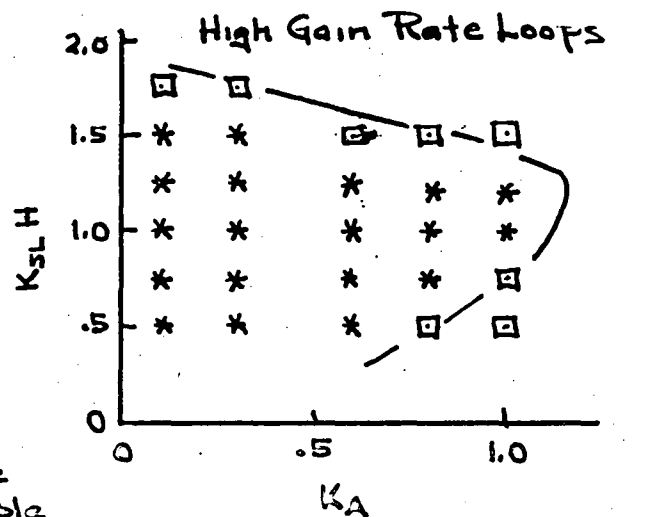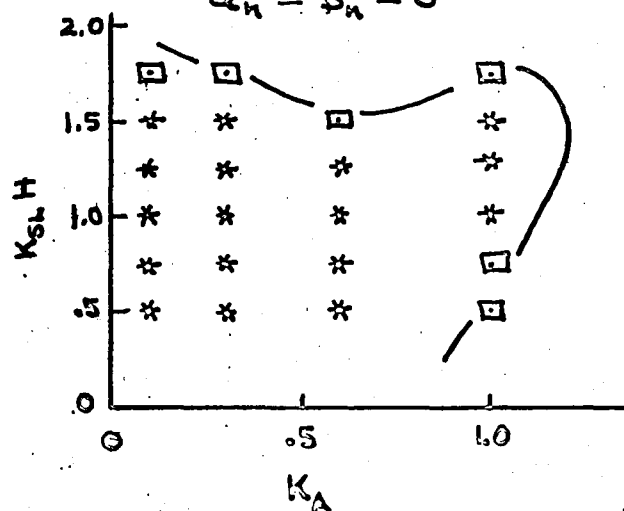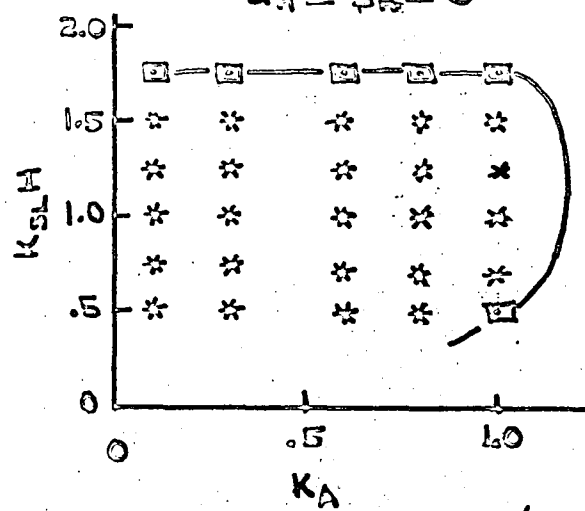
Figure 23.—H-Vector Stability Bounds.
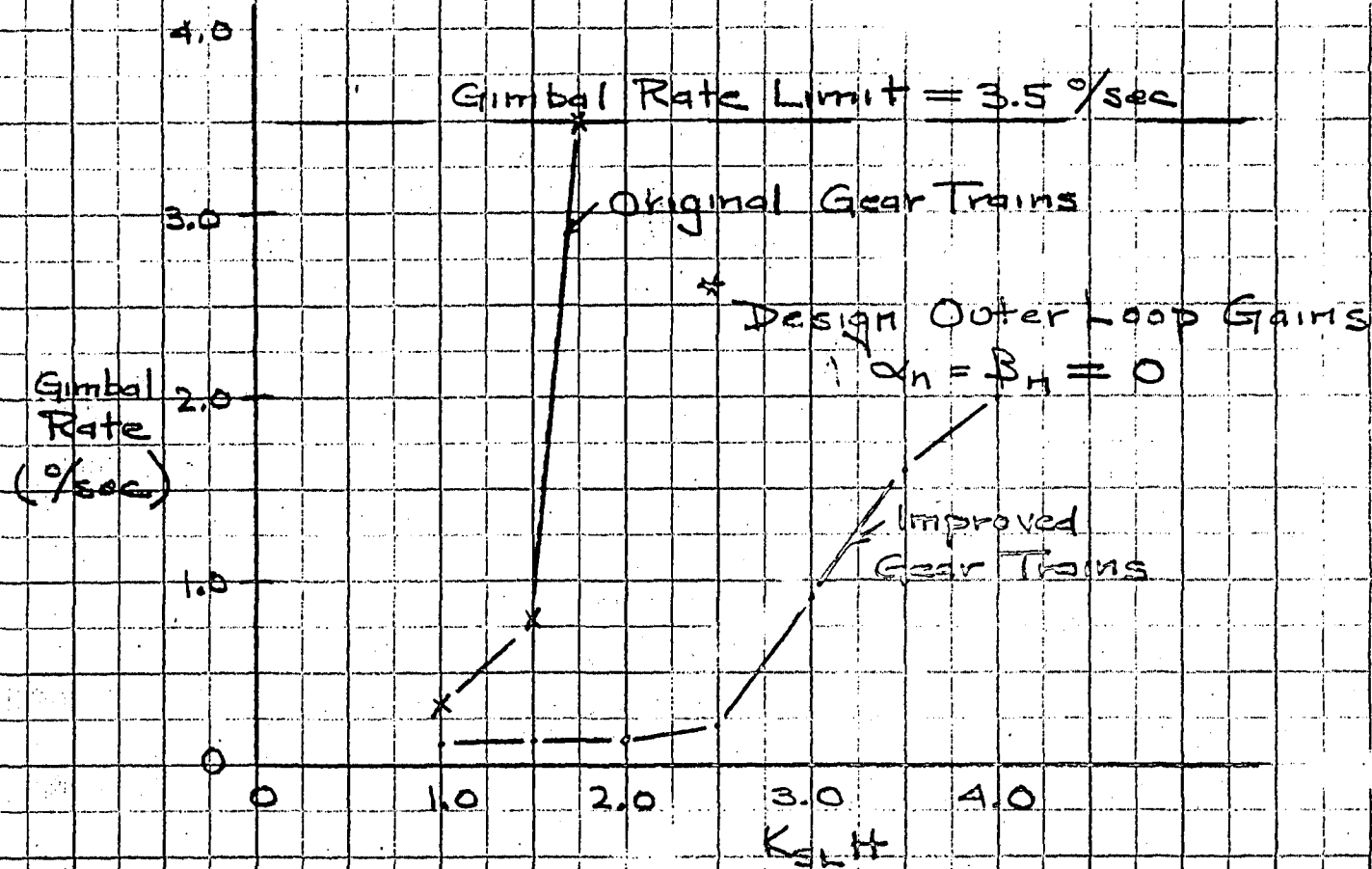
Figure 24. — CMG limit cycles, $K_A = 1.0$.

Figure 25. — COMPENSATED CONTROL SYSTEM RESPONSE

MEASURED GIMBAL RATES FOR THREE-AXIS .05° SPACECRAFT MANEUVER

$\dot{\alpha}$ = OUTER GIMBAL RATE
$\dot{\beta}$ = INNER GIMBAL RATE

FULL ATM
DESIGN GAINS
IMPROVED GEAR
TRAINS

K_α = 16 sec
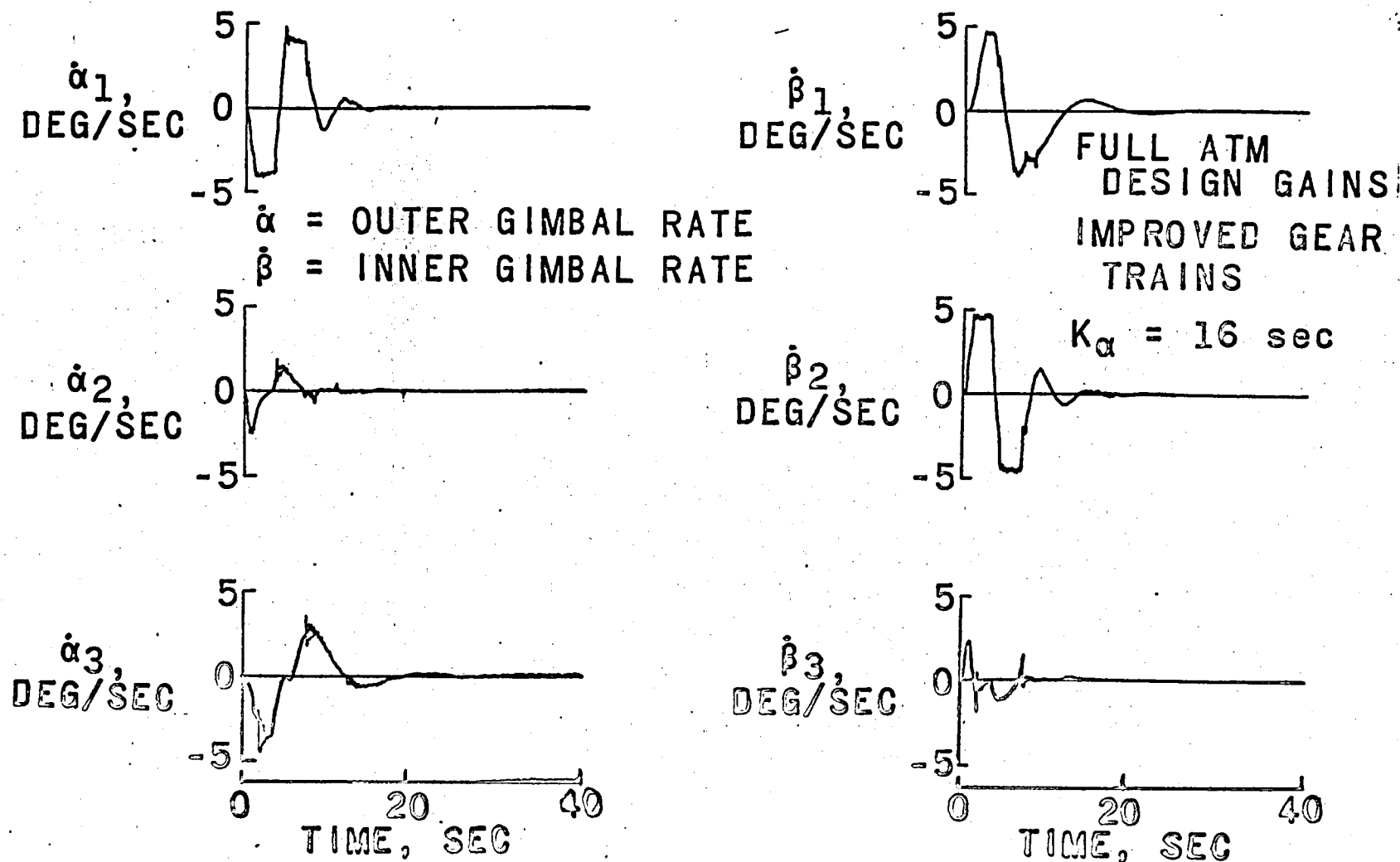
Figure 26.—UNCOMPENSATED CONTROL SYSTEM RESPONSE
MEASURED GIMBAL RATES FOR THREE-AXIS .05° SPACECRAFT MANEUVER
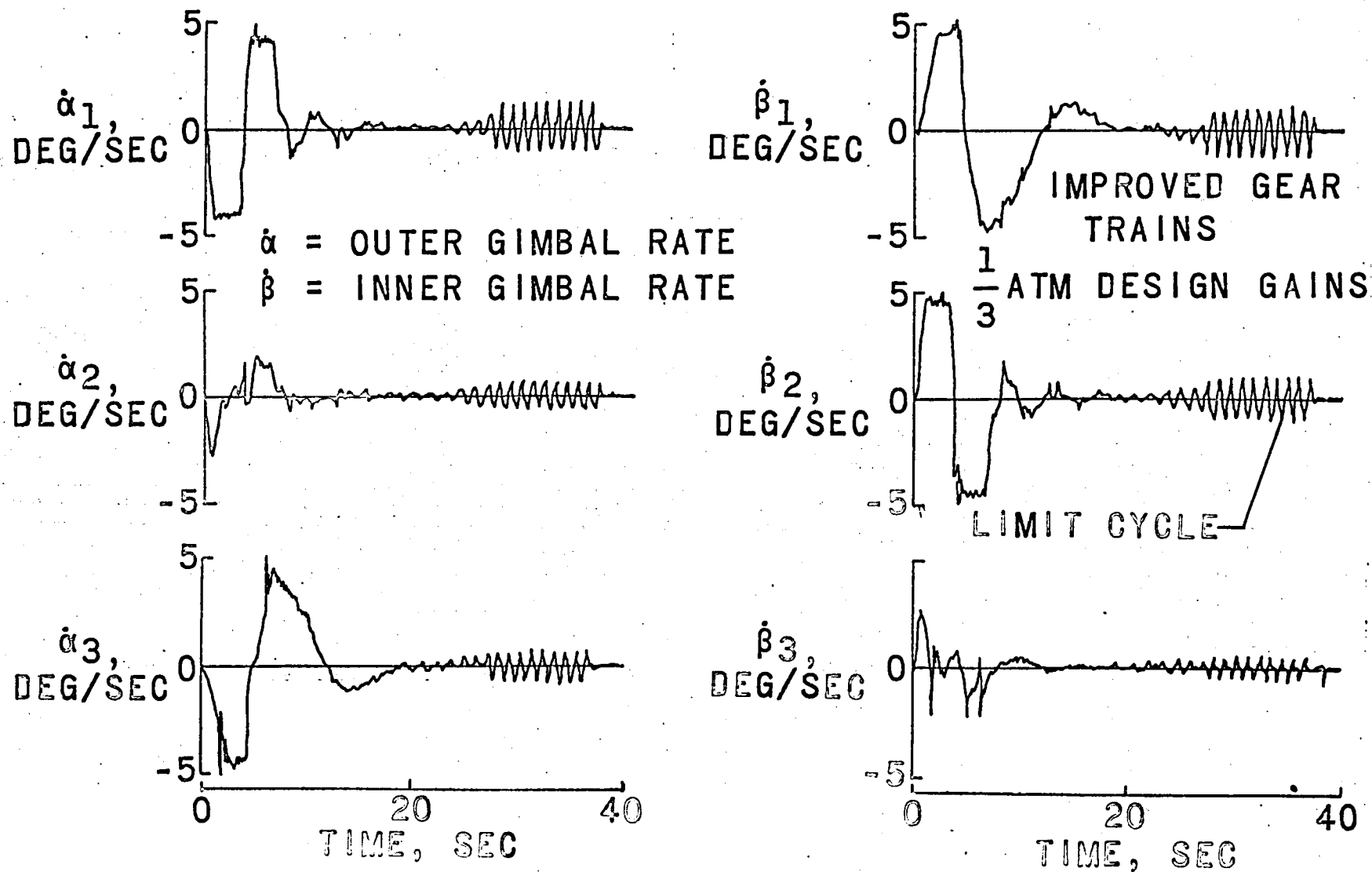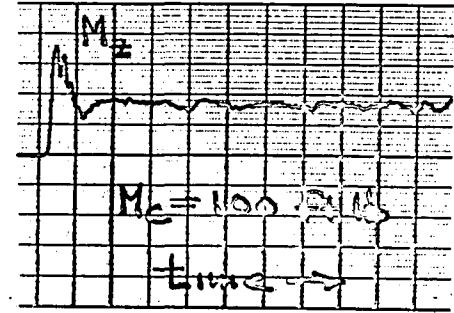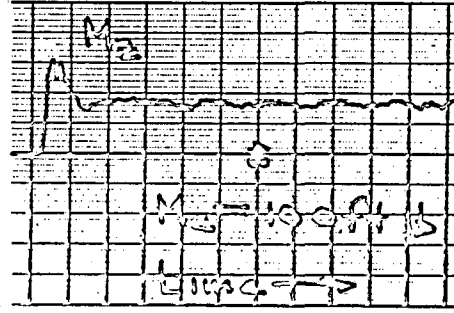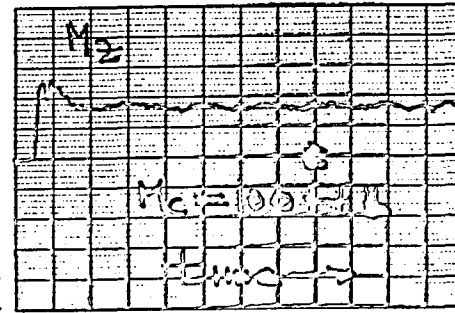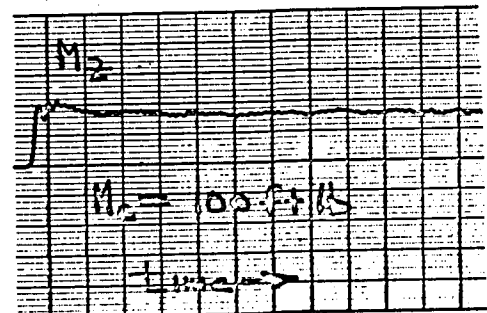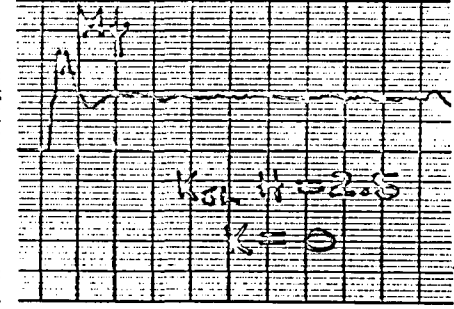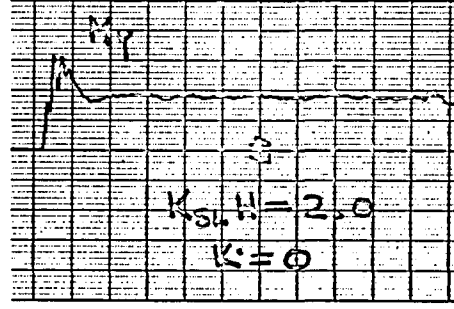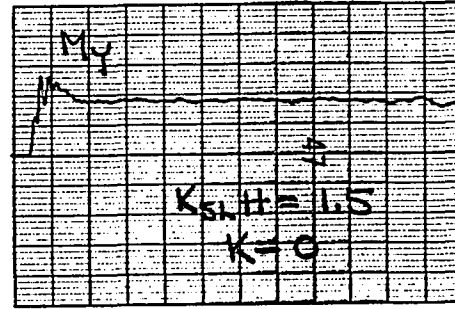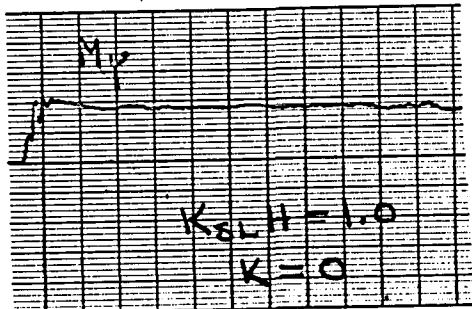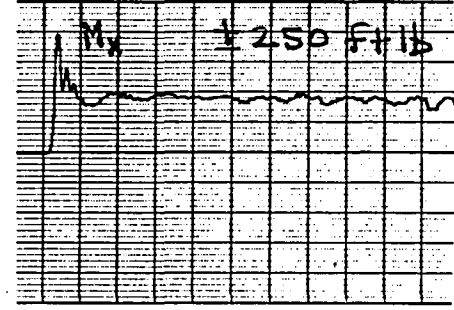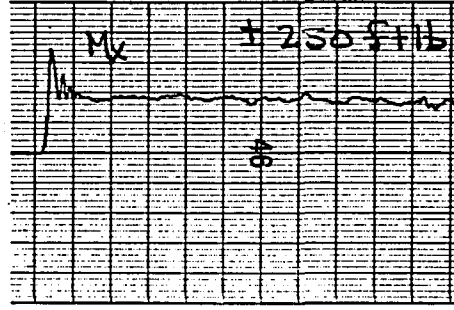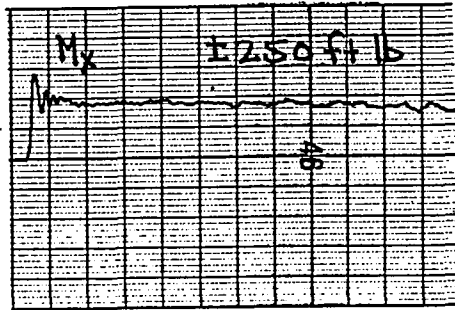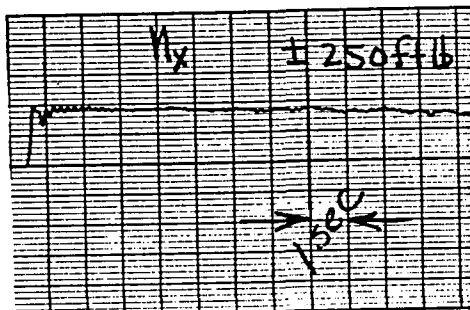
Figure 27 (a)   Figure 27 (b)   Figure 27 (c)   Figure 27 (d)

Figure 27(e)

Figure 27(f)

Figure 27(g)

Figure 27 (h)
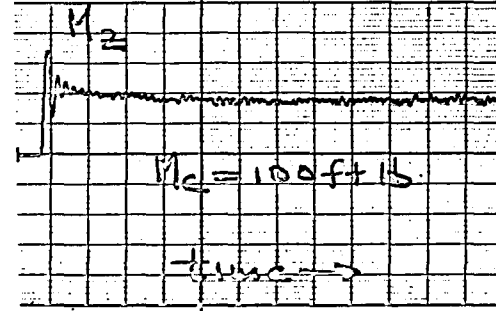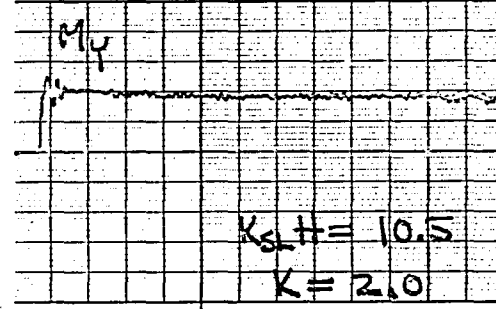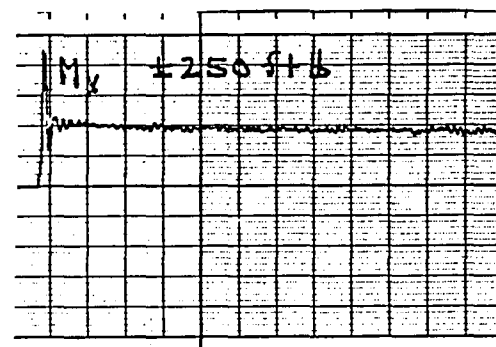
Figure 27 (i)
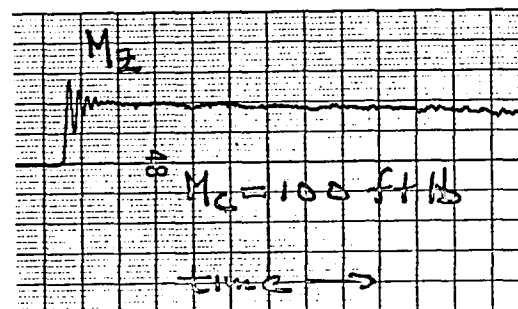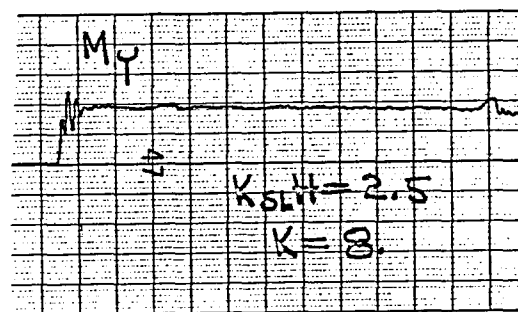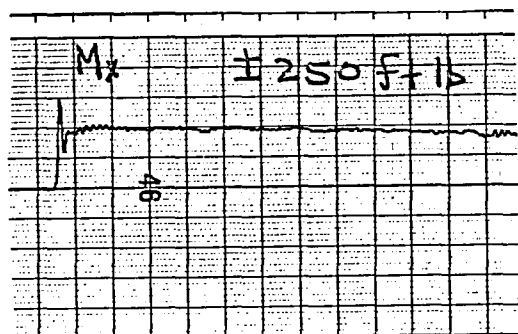
Figure 27 (j)
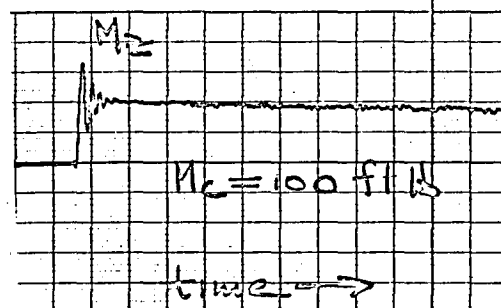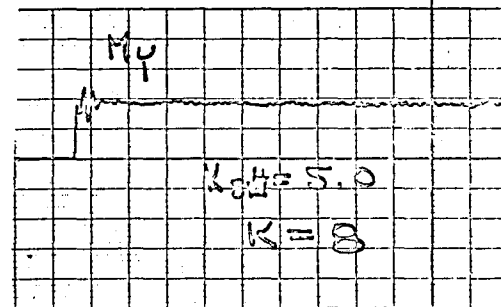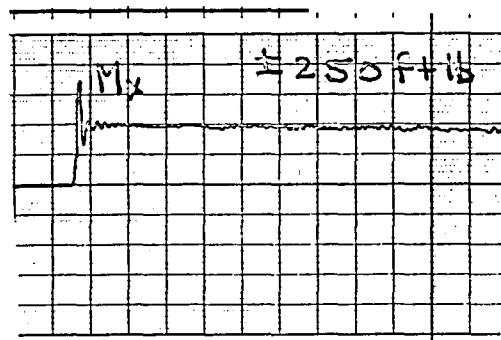
Figure 27 (k)

Figure 27 (l)
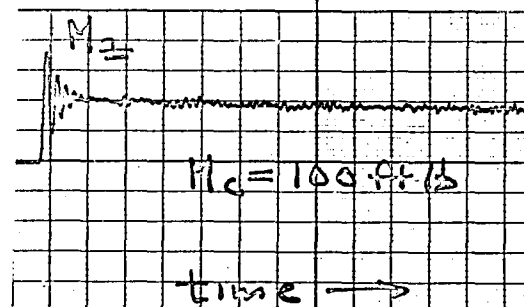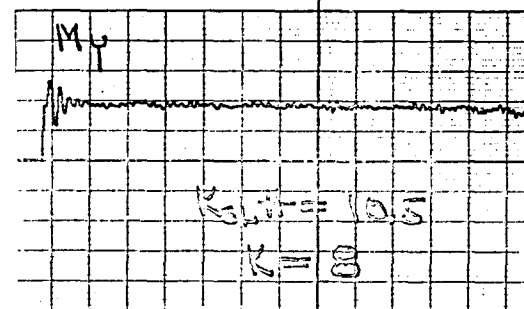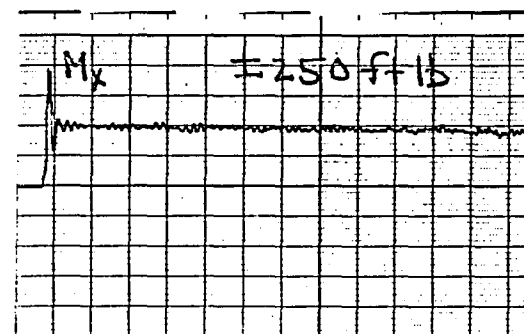
Figure 27 (m)
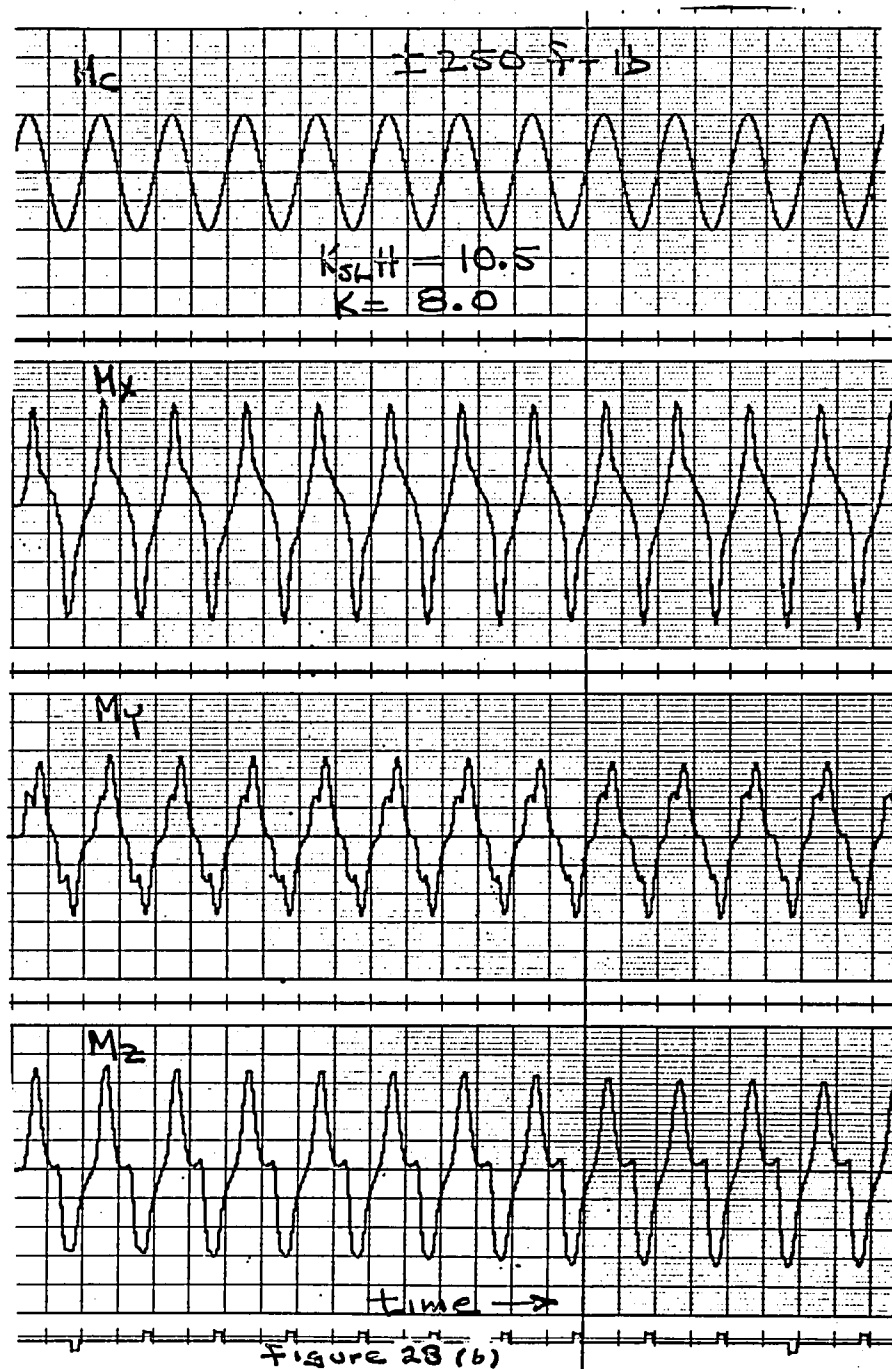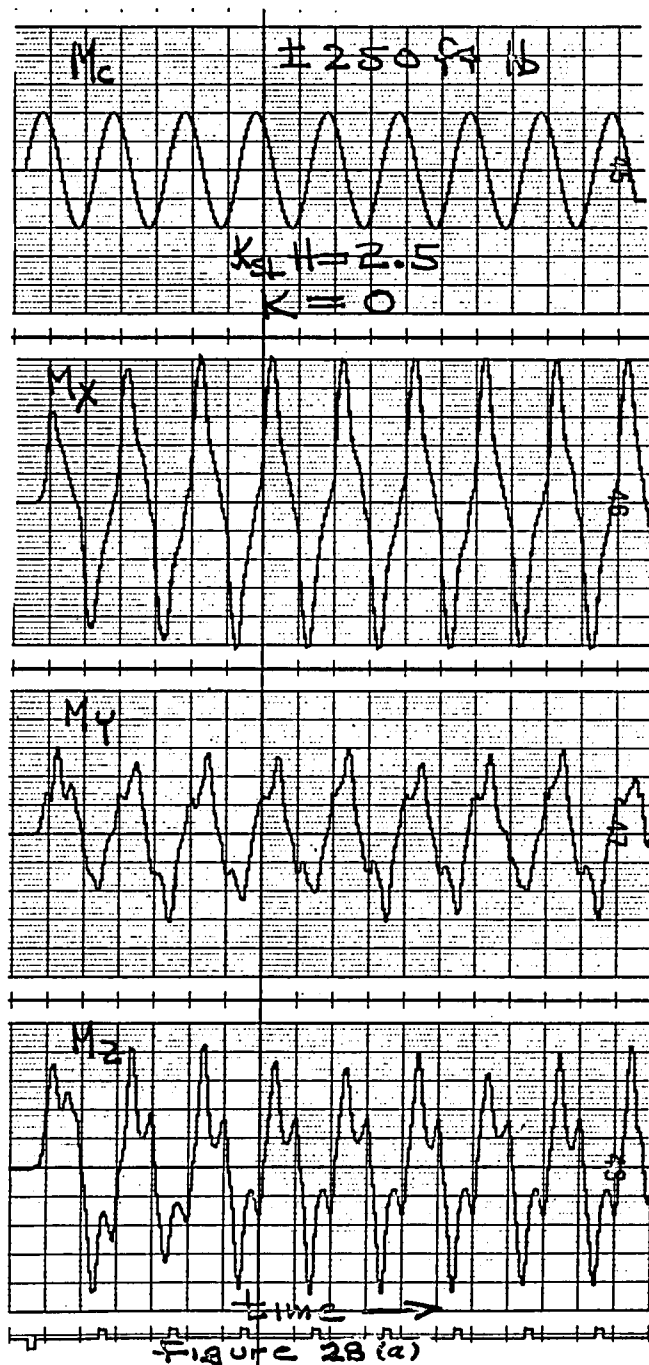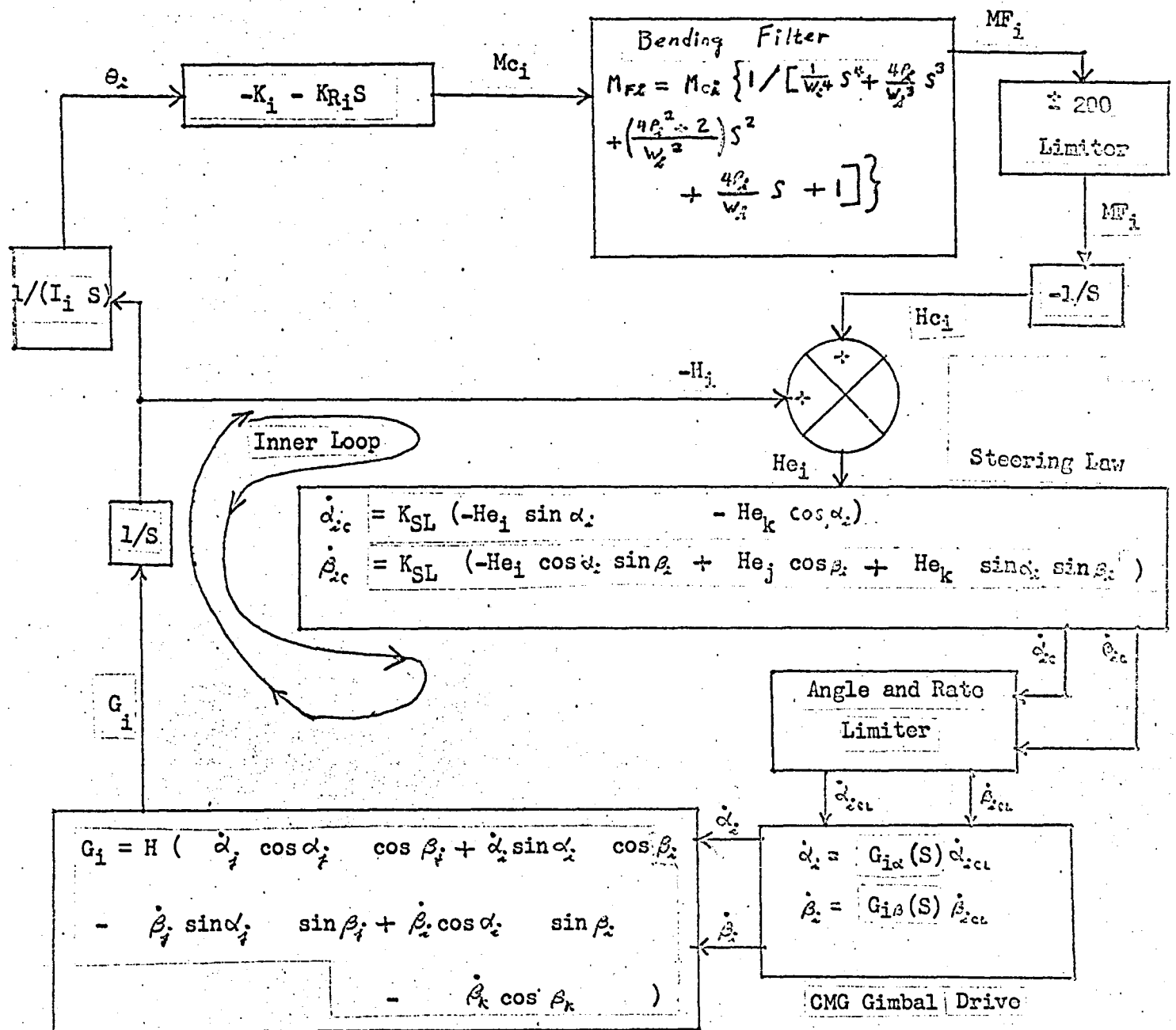
Figure 28 (a)

Figure 28 (b)

Figure 29.- H-vector feedback control system.
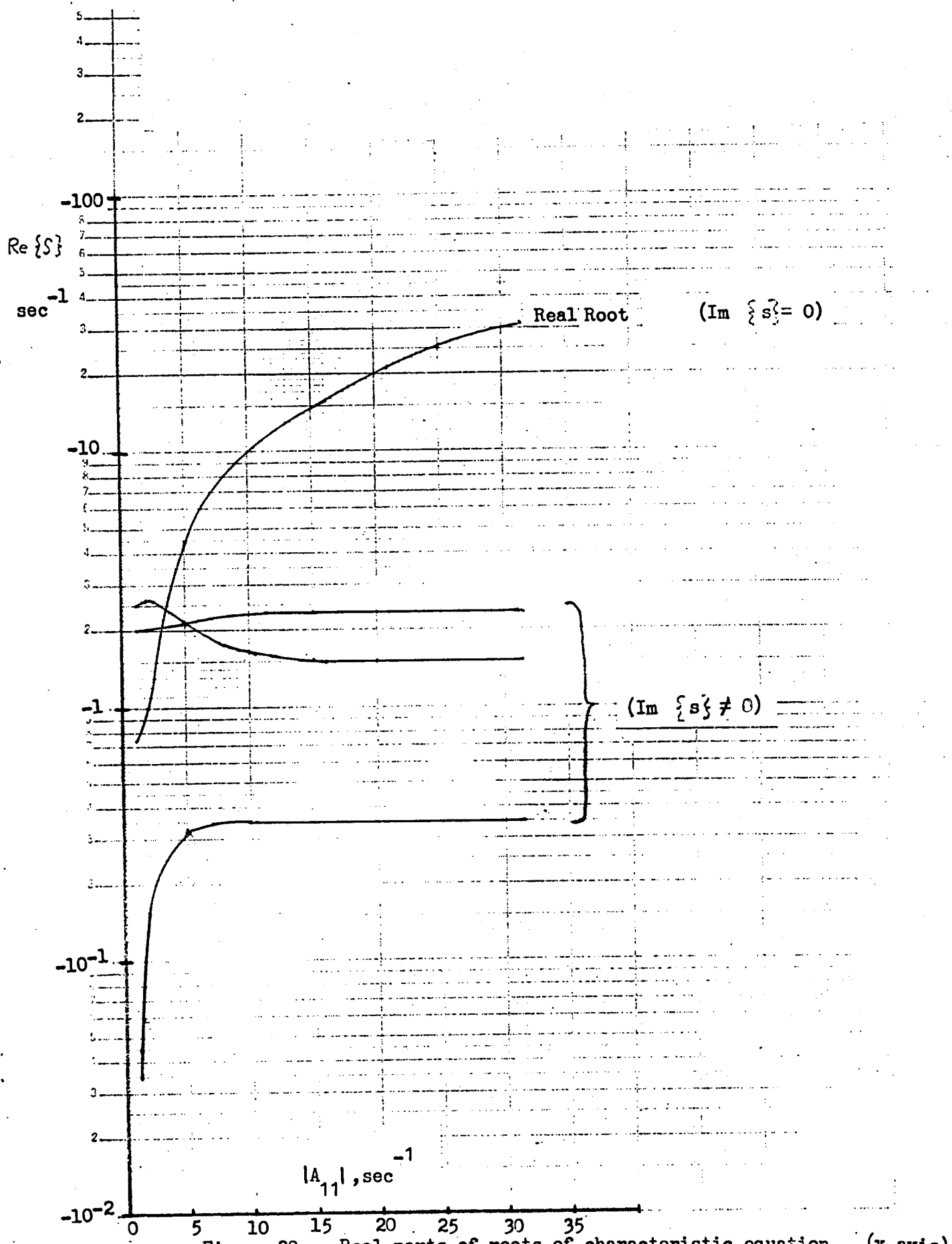
Figure 30.- Real parts of roots of characteristic equation. (x axis)
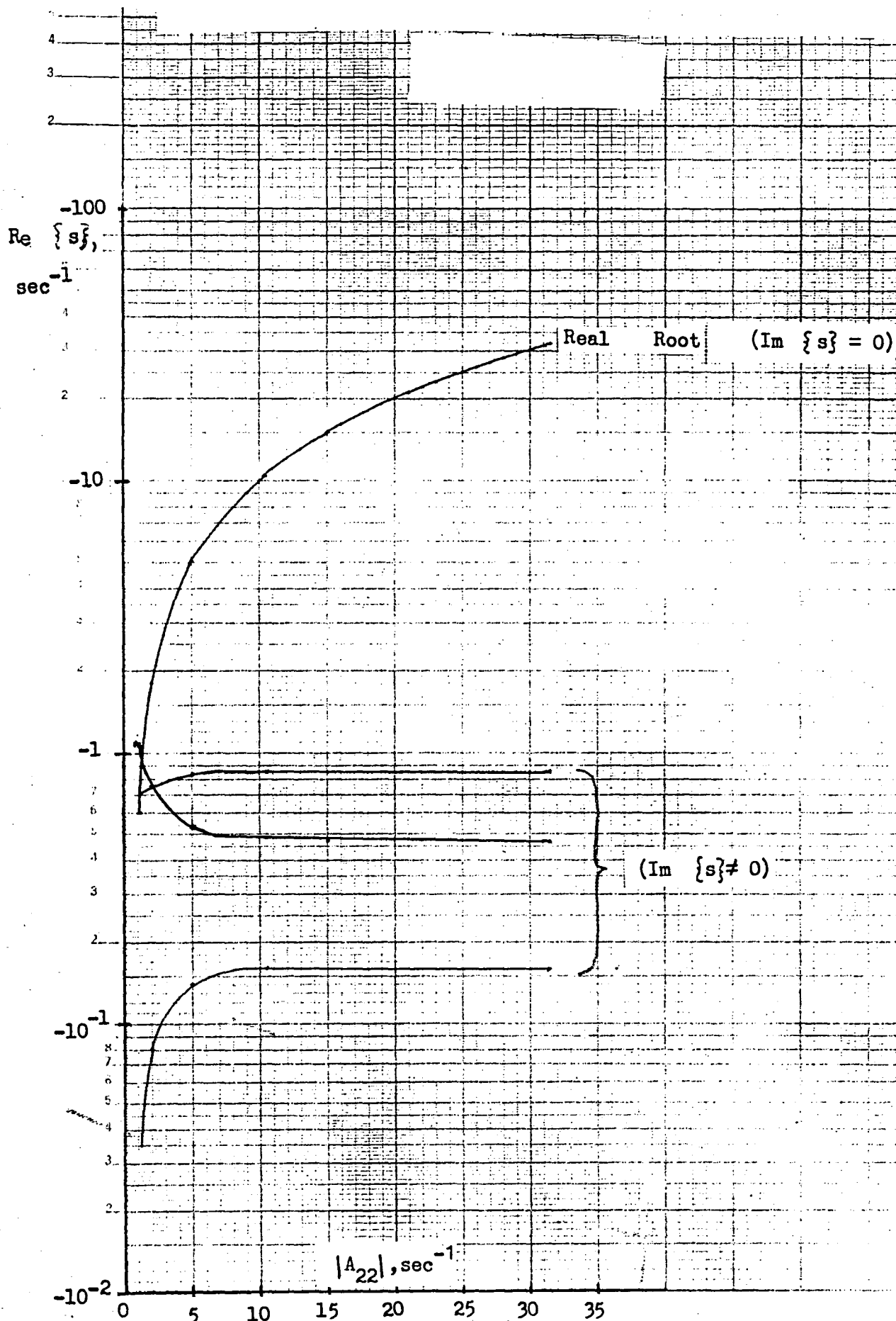
Figure 31.- Real parts of roots of characteristic equation. (y axis)
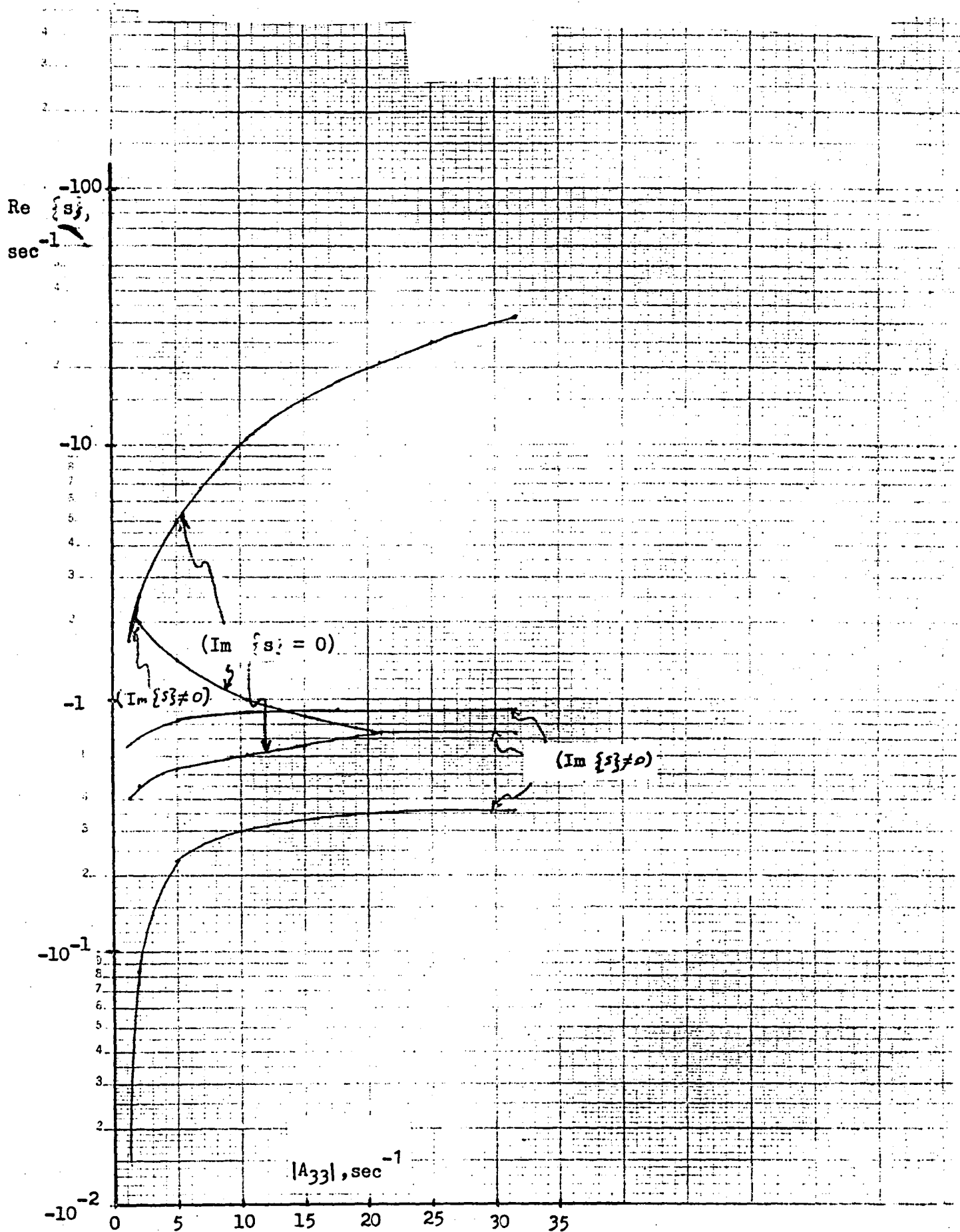
Figure 32.– Real parts of roots of characteristic equation. (z axis)
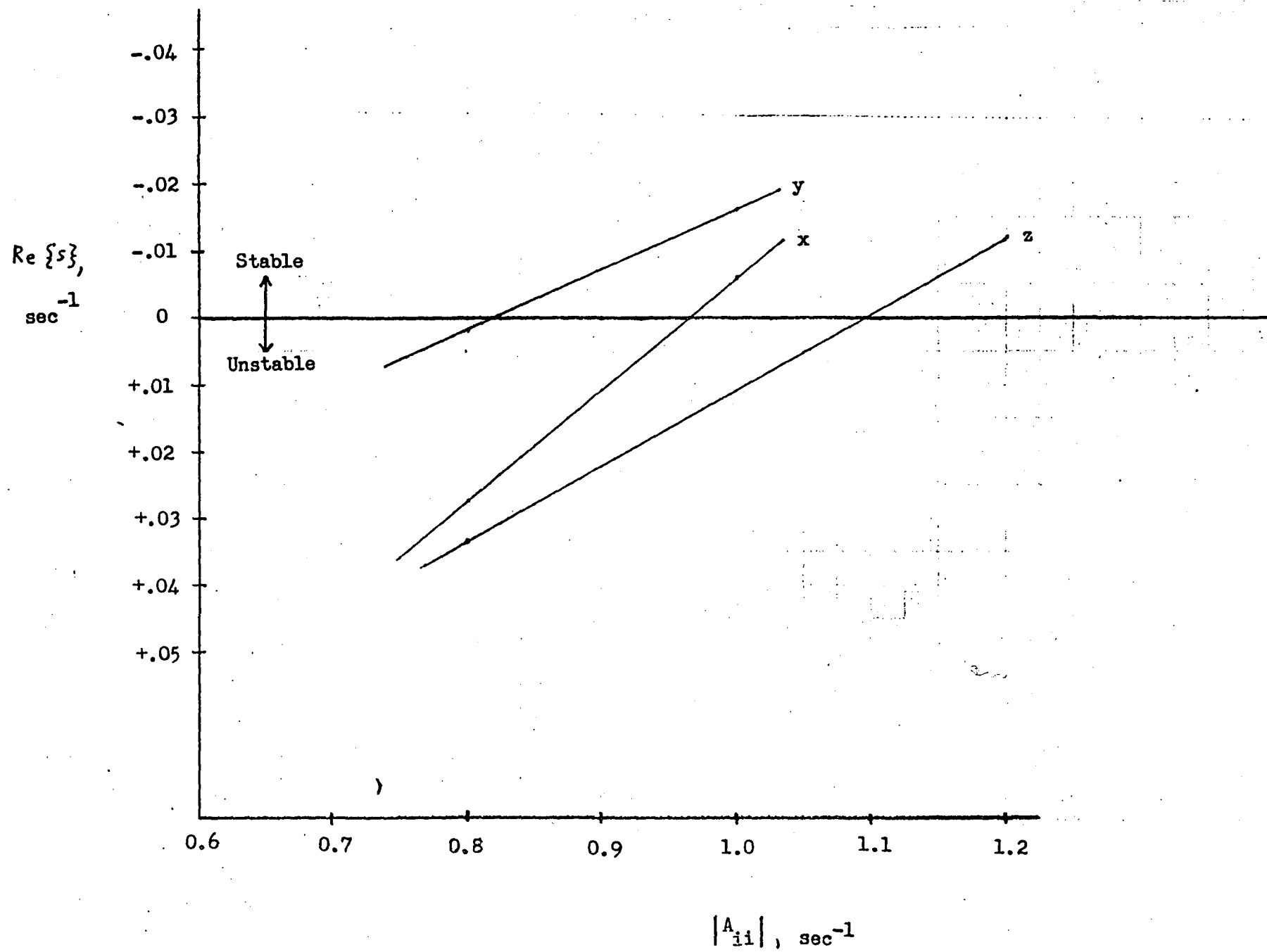
Figure 33.- Real parts of least damped roots of characteristic equation.
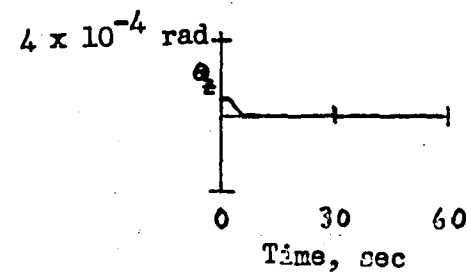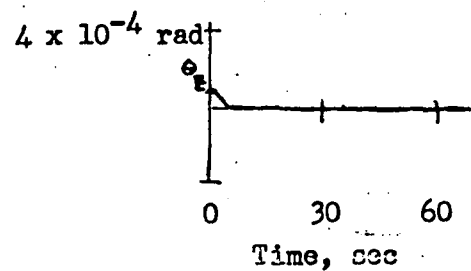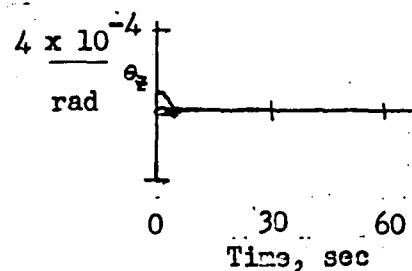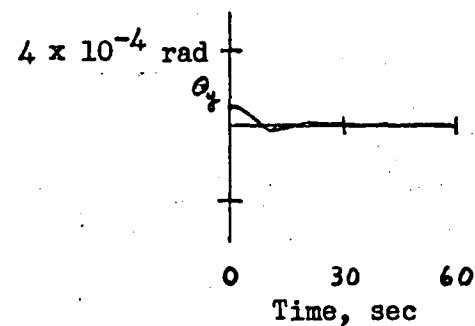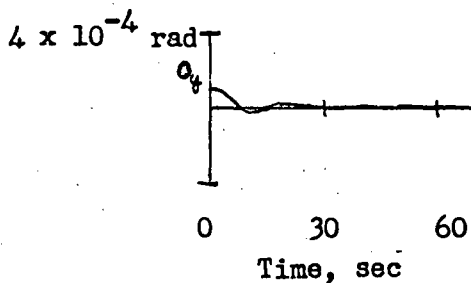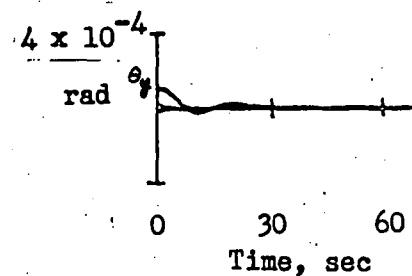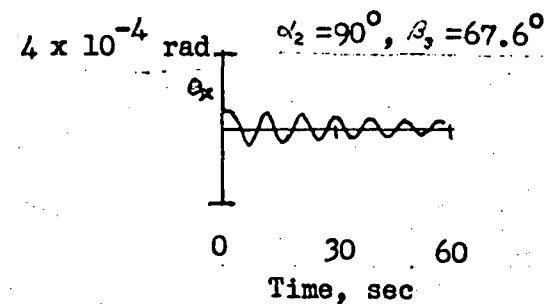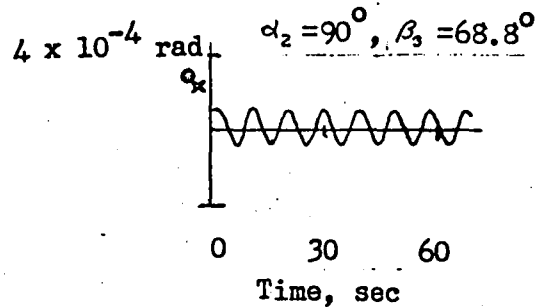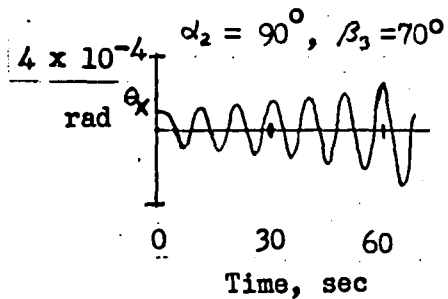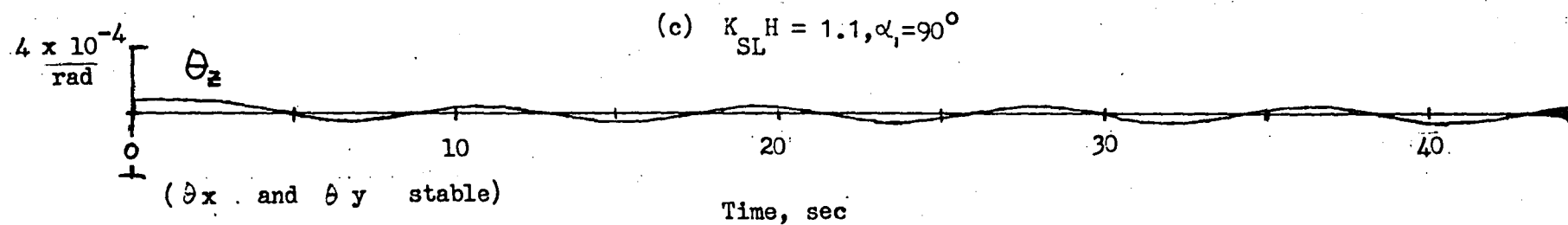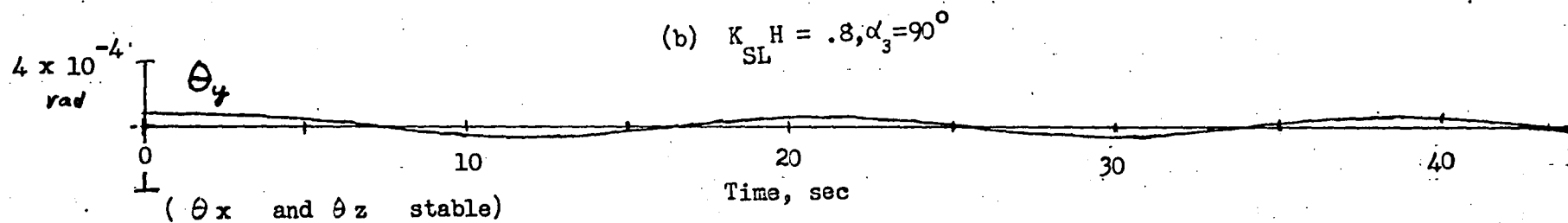
Figure 34.- Simulated acquisition maneuvers.

4×10^{-4} / rad θ_x
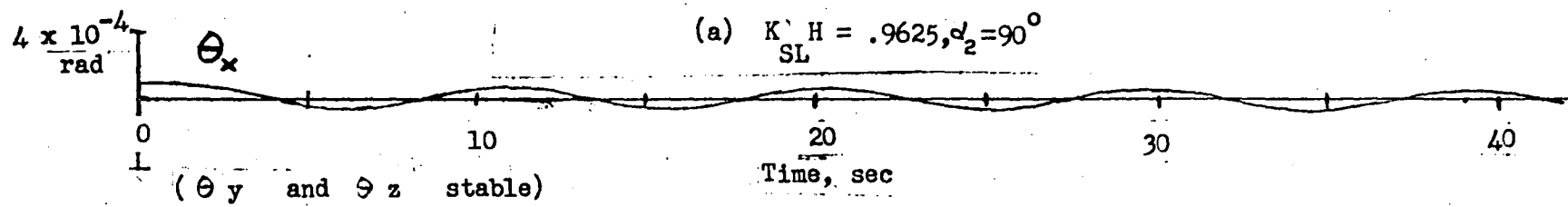
(a) $K_{SL}H = .9625, \alpha_2 = 90°$

0   10   20   30   40

(θ_y and θ_z stable)   Time, sec

(b) $K_{SL}H = .8, \alpha_3 = 90°$

4×10^{-4} / rad θ_y

0   10   20   30   40

(θ_x and θ_z stable)   Time, sec

(c) $K_{SL}H = 1.1, \alpha_1 = 90°$

4×10^{-4} / rad θ_z

0   10   20   30   40

(θ_x and θ_y stable)   Time, sec

Figure 35.- Simulated acquisition maneuvers
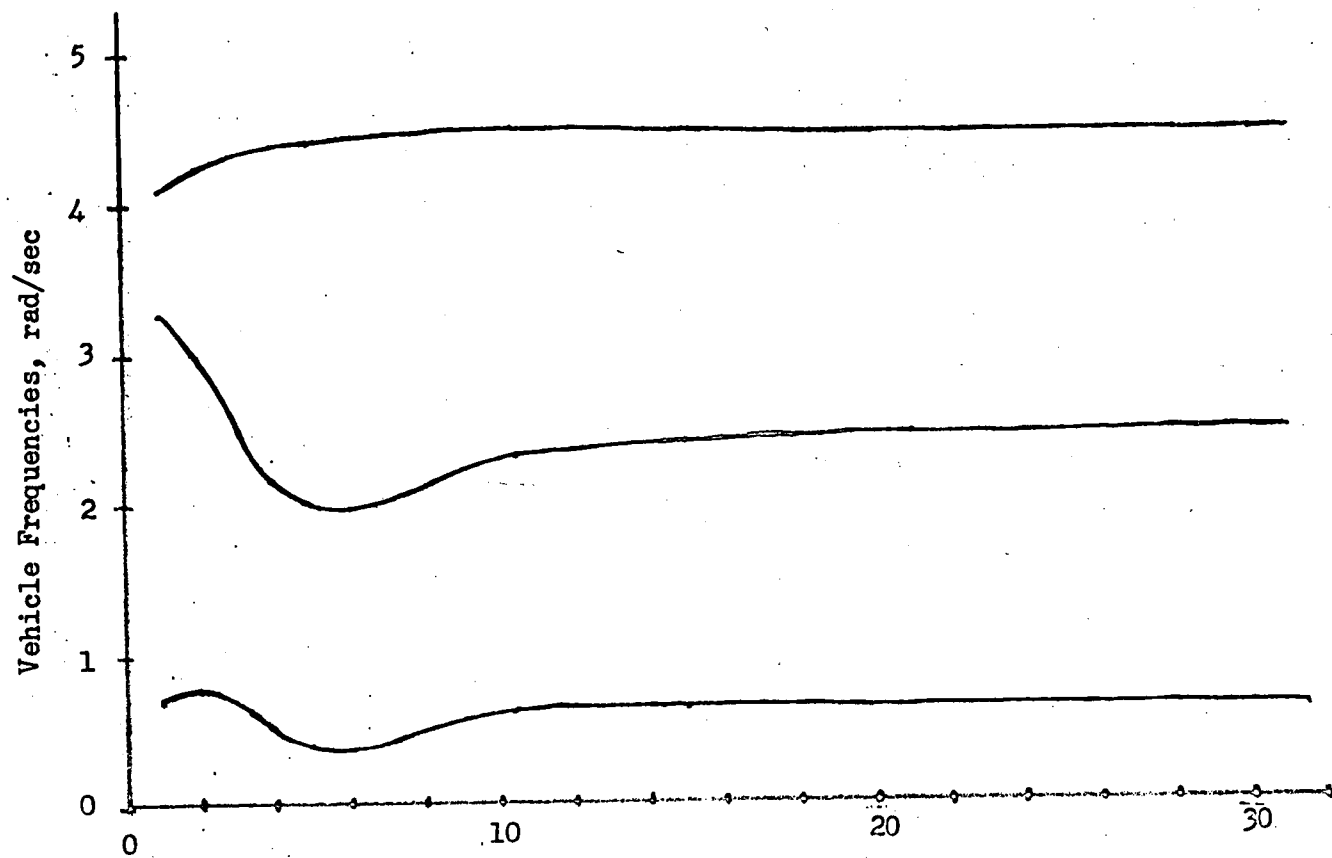
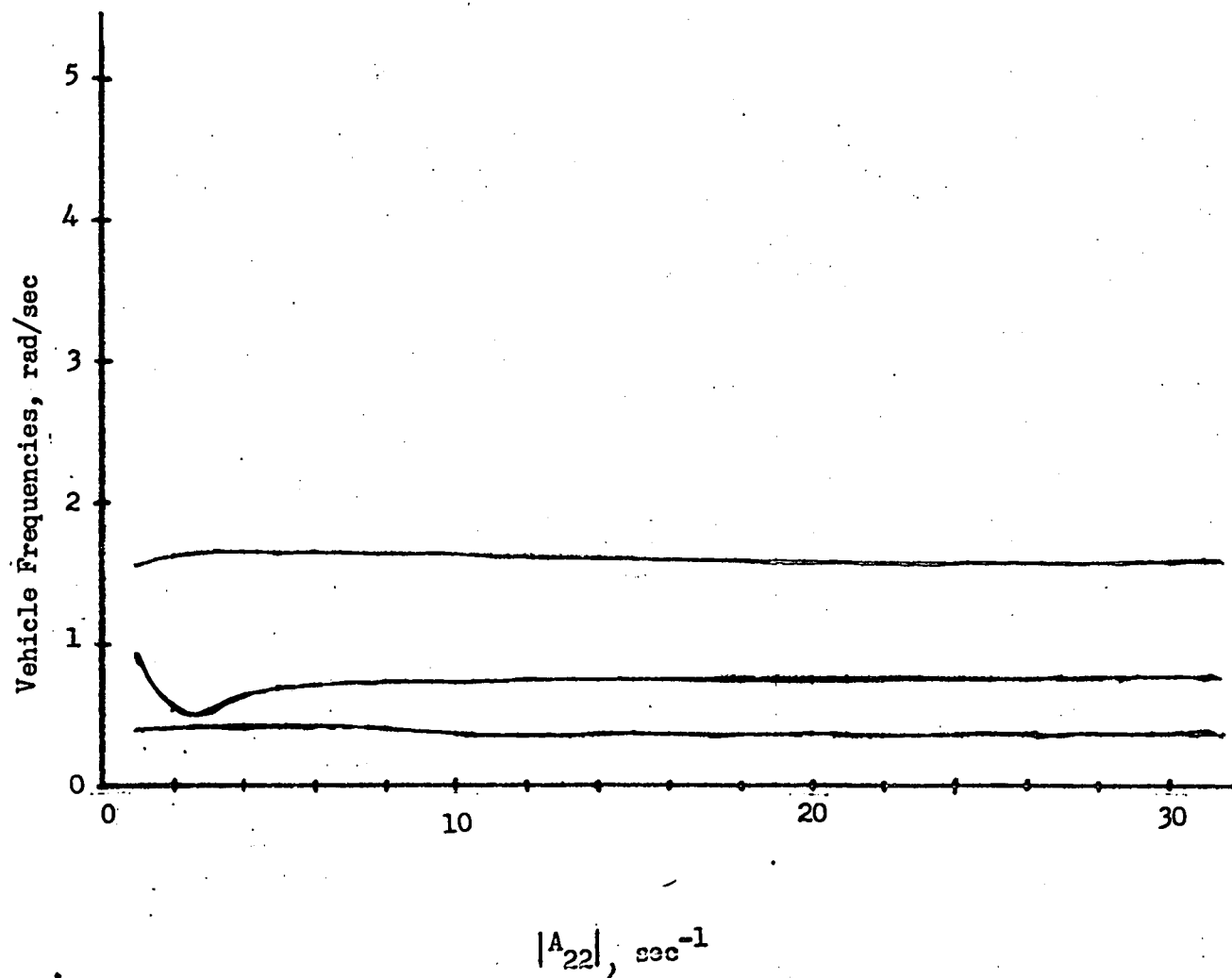Figure 36.- Theoretical θ_x vehicle frequencies.

Figure 37.- Theoretical θ_y vehicle frequencies.
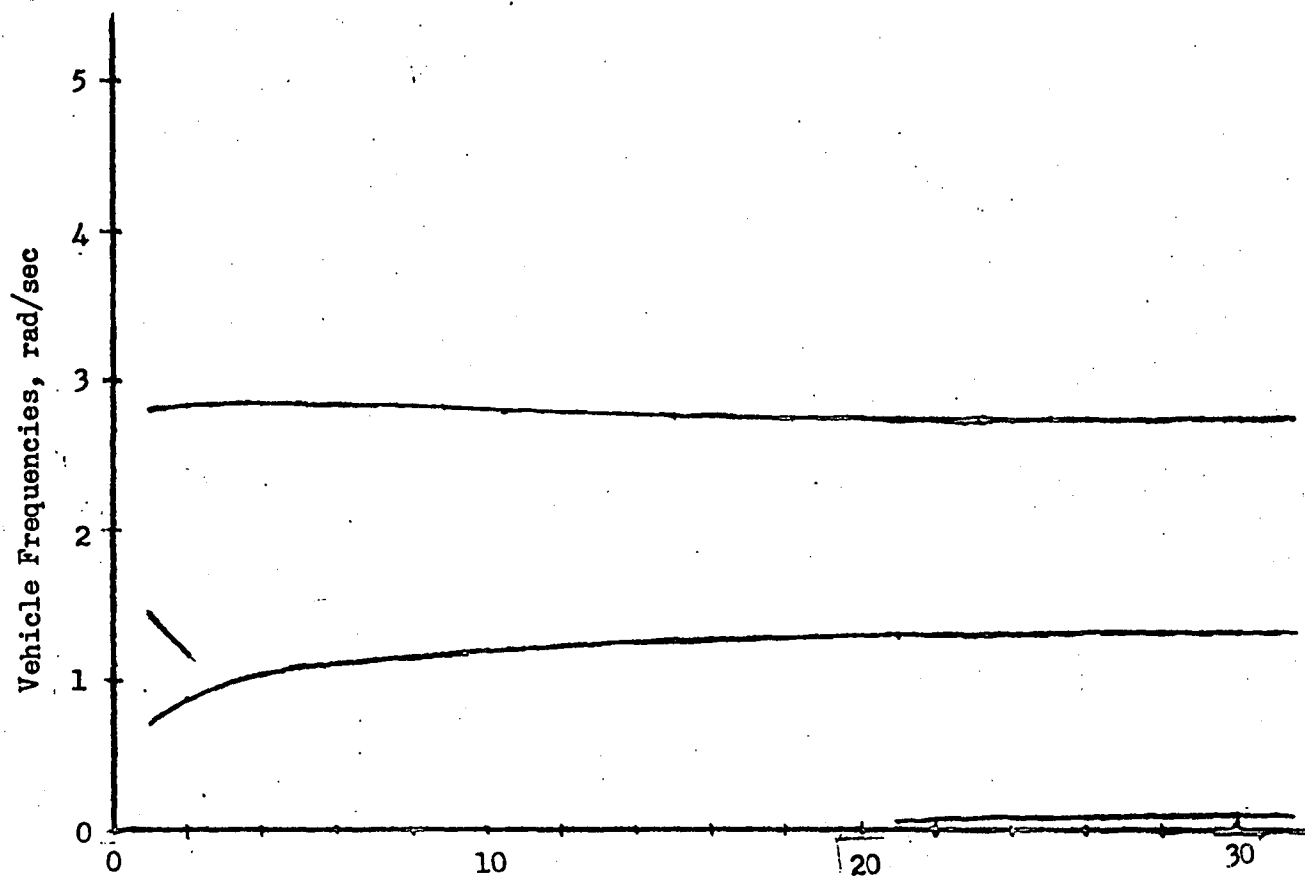
Figure 38.- Theoretical θ_3 vehicle frequencies.
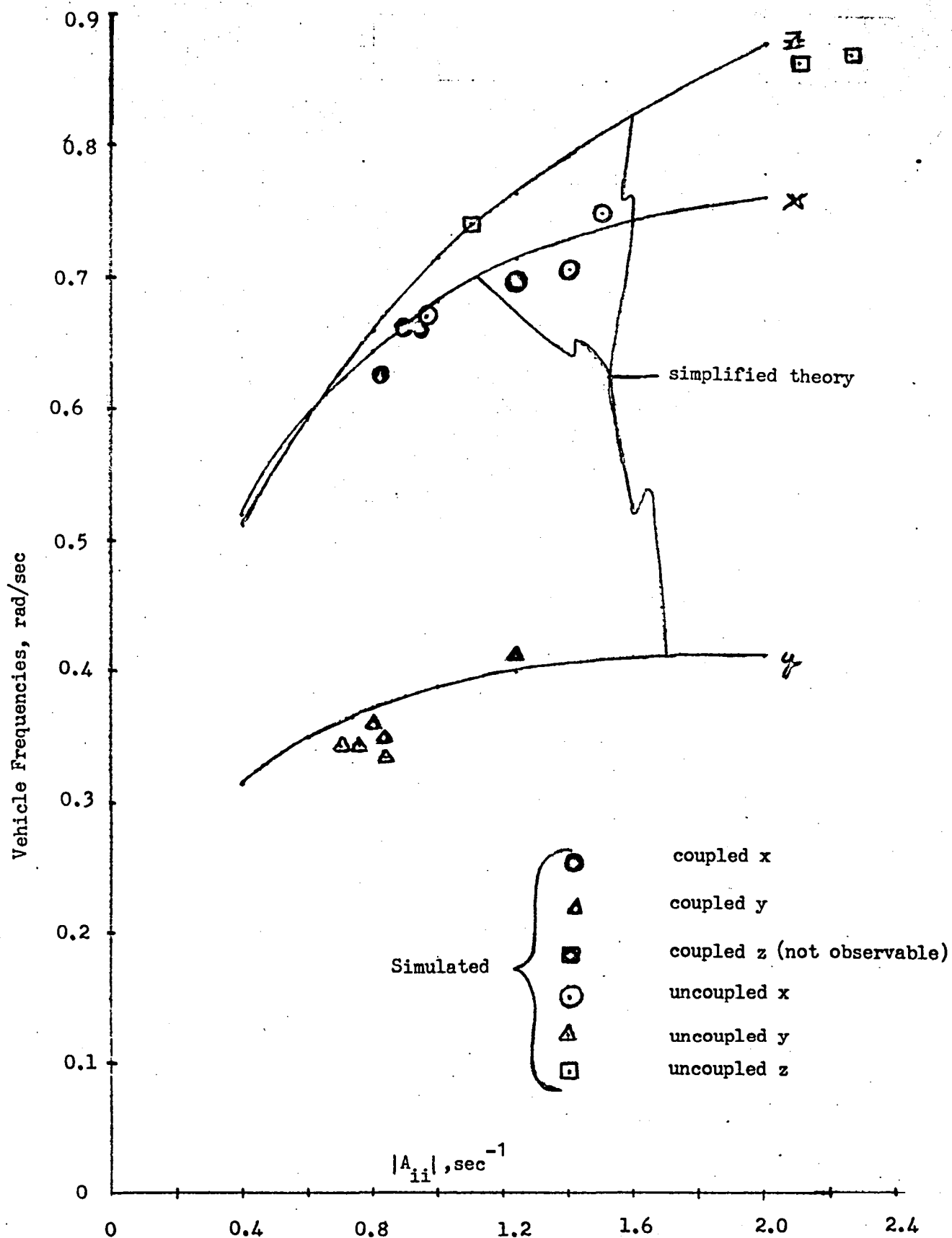
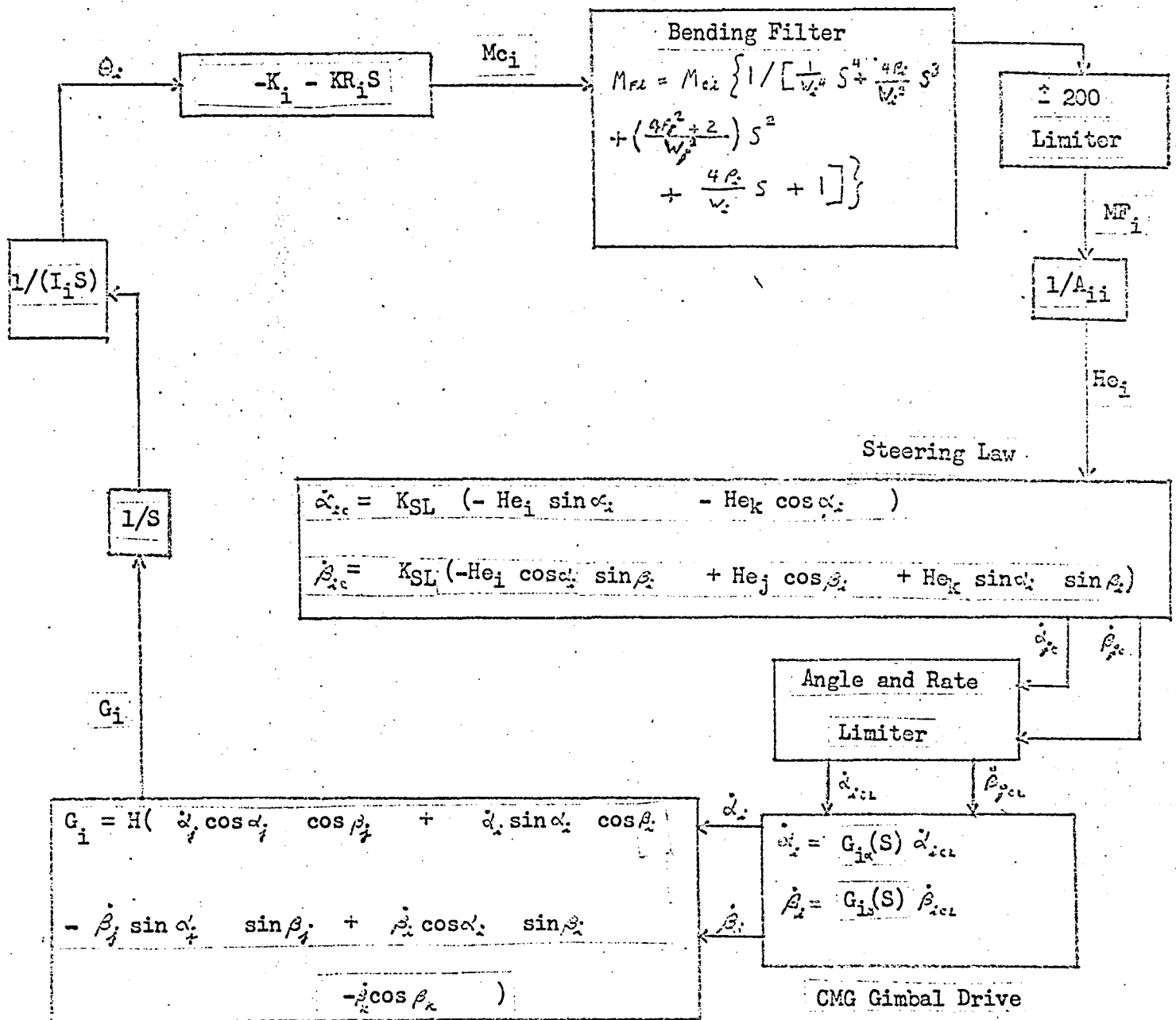Figure 39.- Theoretical and simulated frequencies near neutral stability.

Figure 40.- Equivalent circuit for H-vector feedback system with Z operator.

1. Report No. NASA TM-81827	2. Government Accession No.	3. Recipient's Catalog No.
4. Title and Subtitle ATM-CMG CONTROL SYSTEM STABILITY		5. Report Date May 1980
		6. Performing Organization Code
7. Author(s) W. W. Anderson, L. M. Avis and K. L. Jacobs		8. Performing Organization Report No.
		10. Work Unit No. 506-54-23-01
9. Performing Organization Name and Address NASA Langley Research Center Hampton, VA 23665		11. Contract or Grant No.
		13. Type of Report and Period Covered Technical Memorandum
12. Sponsoring Agency Name and Address National Aeronautics and Space Administration Washington, DC 20546		14. Army Project No.

16. Abstract

Stability analyses and simulation data and results are presented for an initial
Control Moment Gyroscope (CMG) system proposed for the Apollo Telescope Mount
(ATM) cluster (later named Skylab) using momentum vector feedback. A compensa-
tion filtering technique is presented which significantly improved analytical and
simulation performance of the system. This technique is quite similar to the
complementary filtering technique and represents an early NASA application.

17. Key Words (Suggested by Author(s)) Skylab, Control Moment Gyro Complementary filter	18. Distribution Statement Unclassified - Unlimited Subject Category 18		
19. Security Classif. (of this report) Unclassified	20. Security Classif. (of this page) Unclassified	21. No. of Pages 73	22. Price* $5.25